Interstellar Scintillation of the Radio Source Associated with the Gamma-Ray Burst of May 8, 1997

T. V. Smirnova and V. I. Shishov

Astro Space Center, Lebedev Physical Institute, 53 Leninskiĭ pr., Moscow, 117924 Russia
Received July 27, 1999

Abstract—The variability of the radio source associated with the gamma-ray burst of May 8, 1997, detected using the VLA, is analyzed. This variability can be explained as weak scintillations at 4.86 and 8.46 GHz and the refractive component of saturated scintillations at 1.43 GHz. Possible distances for the source are discussed. The scintillation parameters are in best agreement with the observations if the source is at a cosmological distance and has an angular size ~2 microarcseconds (μas) at 4.86 GHz and an expansion speed of the order of 25 μas/year. © 2000 MAIK "Nauka/Interperiodica".

1. INTRODUCTION

A large amount of data on gamma-ray bursts has now been accumulated, but their origin remains a mystery. Since the distances to gamma-ray bursts are not known, there exist a whole range of hypotheses suggesting both Galactic [1, 2] and extragalactic [3, 4] origins. It was only in 1997 that it became possible to localize the coordinates of these objects rather accurately using the BeppoSAX observatory [5], making it possible to conduct quasi-synchronous observations of gamma-ray bursts at other wavelengths, which provides very important clues about their nature. Recently, important arguments have appeared in favor of a cosmological origin: optical afterglows have been detected for five gamma-ray bursts, enabling measurement of their redshifts. However, physically unrelated optical objects could also fall in the coordinate error boxes for the gamma-ray bursts. In addition, it is possible that different gamma-ray bursts could have different physical natures.

The gamma-ray burst of May 8, 1997, is a unique event, since emission was observed at the same location over a wide range of wavelengths: X-ray [5]; optical [6, 7]; and, for the first time, radio [8]. Spectroscopic observations of the optical afterglow yielded the redshift of an object less than 0.37 arcsec from the galaxy where the gamma-ray burst was detected ($z \geq 0.835$ [6]). This testifies to an extragalactic origin for the gamma-ray burst if the optical object is physically related to the burst.

Frail *et al.* [8] discuss the detection of the variable radio source VLA J065349.4 + 791619, whose coordinates coincide within the errors with the gamma-ray burst GRB 970508. The VLA observations were begun at frequency $f_1 = 1.43$ GHz 3.7 hours after the onset of the burst and then at frequencies $f_2 = 4.86$ GHz and $f_3 = 8.46$ GHz five days later. The radio flux detected at $f_2 = 4.86$ and $f_3 = 8.46$ GHz displayed a high degree of variability, while the radio flux at $f_1 = 1.43$ GHz had substantially lower intensity. Frail *et al.* [8] concluded that the radio source was physically related to the

gamma-ray burst and interpreted the radio variability as diffractive scintillations (in a strong scattering regime) of an extragalactic source on plasma inhomogeneities in the interstellar medium. Possible effects of scintillation of radio sources associated with gamma-ray bursts are discussed in [9].

Our work is aimed at interpreting the observed variability of the detected radio source using the most current data on interstellar scintillations. This is important, since analysis of the radio variability can be used to derive the source's angular size and distance. Although the interpretation of Frail *et al.* [8] is based on an angular size for the source that is of the correct order of magnitude, their picture of the flux variations as diffractive scintillations in inhomogeneities in the interstellar plasma is incorrect. In contrast to Frail *et al.* [8], we have analyzed various possible scintillation regimes based on the most current theoretical concepts and on observational data obtained for interstellar scintillations of pulsars.

In addition, we have investigated the frequency dependence of the modulation index and characteristic time scale for the fluctuations of the radio flux of VLA J065349.4 + 791619 as well as correlations between the variations. We show that the observed variability can be well described as the effect of weak scintillations at the high frequencies and the refractive component of saturated scintillations at the lower frequency. We also discuss the question of whether the source is Galactic or extragalactic; the nature of gamma-ray bursts in general and an analysis in terms of current "fireball" models lie beyond the framework of our study.

2. ANALYSIS OF THE OBSERVATIONAL DATA

We used the data of Frail *et al.* [8] in our analysis of the radio flux variations for VLA J065349.4 + 791619 at 8.46 and 4.86 GHz. Although there are no data at 4.86 GHz on some days, there is a rather good correlation between the variations at the two frequencies, for

both short-period (~1 d) and slower (~30 d) variations. The correlation coefficient is $R = 0.63$. The time intervals between observations were irregular, but most of the observations were separated by one to two days. During the first 30 days, there was rather strong variability of the radio flux, even between neighboring days; that is, the time scale for the variations was $\tau \leq 1$ d. On subsequent days, the amplitude of the variations substantially decreased, as noted in [8].

We divided the entire time interval for the observations into two parts. The first interval covered the time up until June 9.74, 1997 (~32 d after the burst), when rapid variability with a large modulation depth was observed; the second interval ended on August 4, 1997, when the variation amplitude had appreciably decreased. We obtained for the mean fluxes and modulation indices $S_{4.86} = 620$ μJy, $m_{4.86} = 0.44$, $S_{8.46} = 680$ μJy, and $m_{8.46} = 0.32$ for the first interval, and $S_{4.86} = 530$ μJy, $m_{4.86} = 0.22$, $S_{8.46} = 600$ μJy, and $m_{8.46} = 0.2$ for the second interval.

Assuming that $S \propto f^{\alpha}$, we find that $\alpha \cong 0.2$ at 4.86–8.46 GHz for both intervals. The characteristic time scale for the fluctuations is less certain. On the one hand, it is clear that this time is less than a day, but, on the other hand, it is longer than the time for a single observing session, which is probably no less than one hour. In cases when there are measurements separated by several tenths of a day, the differences between the fluxes for neighboring measurements are appreciably less than the differences between flux measurements separated by a day or more.

We adopt as an estimate of the characteristic time scale for the fluctuations in the first interval $t_{8.46} \approx 1/3$ d. An estimate derived from a temporal structure-function analysis yields approximately the same result. The observations in the second interval are less dense, and it is possible that the time scale for the fluctuations is longer. We adopt as an estimate of the time scale $t_{4.86}$ roughly the same value.

At 1.43 GHz, we used the data of Galama *et al.* [10]. No emission at 1.43 GHz was detected over the first 30 days: $S_{1.43} < 80$ μJy [10]. We determined the mean flux at times $t > 30$ d to be $S_{1.43} = 220$ μJy (in agreement with the estimate of [10]) and the modulation index to be $m = 0.66$. This flux is close to that expected based on an extrapolation from the higher frequency measurements with $\alpha = 0.2$. Although the measurements at 1.43 GHz were not made frequently enough to derive a trustworthy estimate of the fluctuation time scale, the variations are characterized by time scales of the order of ten days or less (but longer than two days). The variations at 1.43 GHz were not correlated with the variations observed at higher frequencies.

3. INTERSTELLAR SCINTILLATION IN THE DIRECTION OF THE γ SOURCE

The coordinates of the radio source VLA J065349.4 + 791619 are very close to those of the pulsar PSR J0653 + 8051, which has a dispersion measure DM = 32.5 pc/cm³

and lies at a distance $R = 3$ kpc. Although the scintillation parameters of this pulsar are not known, we can estimate them using data for other pulsars with roughly the same dispersion measures. A key parameter in the determination of the characteristics of interstellar scintillations is the critical frequency f_{cr}, which divides the weak and saturated scintillation regimes. A dependence of f_{cr} on the distance to the pulsar R was obtained in [11]. According to this dependence, we have for a distance $R_0 = 2$–3 kpc $f_{cr} \cong 3$ GHz. The distance R_0 corresponds to the path length through a layer of turbulent plasma at Galactic latitude $b = 30°$, where the source under study is located.

In the weak-scintillation regime, the scintillation index m for a source of small angular size grows as the frequency f decreases. In the case of a Kolmogorov spectrum, with a spectral index for the three-dimensional turbulence spectrum $n = 11/3$, we have

$$m = (f_{cr}/f)^{\alpha}, \quad \alpha = (n+2)/4 \cong 1.4. \qquad (1)$$

On the whole, the observational dependences presented in [11] are close to the theoretically dependences. The characteristic spatial scale for scintillations is equal to the size of the first Fresnel zone,

$$b_{\mathrm{Fr}} = \sqrt{R/k}, \qquad (2)$$

where $k = 2\pi/\lambda$ is the wave number. Accordingly, the time scale for the scintillations is

$$t_0 = b_{\mathrm{Fr}}/V \propto 1/\sqrt{f}, \qquad (3)$$

where V is the velocity of the line of sight relative to the medium. We will consider two velocities: $V = 150$ km/s, which corresponds to the typical velocity for a pulsar, and $V = 30$ km/s, which corresponds to the velocity of the line of sight relative to the interstellar medium for an extragalactic source. Adopting $R = 3$ kpc, we obtain

$$t_0 = 2.2(3 \text{ GHz}/f)^{1/2} \text{ h}, \quad V = 150 \text{ km/s},$$
$$t_0 = 11(3 \text{ GHz}/f)^{1/2} \text{ h}, \quad V = 30 \text{ km/s}. \qquad (4)$$

The characteristic time scale corresponding to $V = 150$ km/s is in agreement with the observational data for pulsars presented in [11].

In a strong-scintillation regime, where $f < f_{cr}$, scintillations will include two components: diffractive and refractive. The scintillation index of the diffractive component is close to unity: $m_{dif} \cong 1$. The time scale for diffractive scintillations decreases with decreasing frequency. Based on a theoretical model with a Kolmogorov spectrum and the observational data presented in [11], we adopt for the pulsar case ($V = 150$ km/s)

$$t_{dif} = 8(f/f_{cr})^{\beta} \text{ h}, \quad \beta = 2/(n-2) \cong 1.2. \qquad (5)$$

The scintillation index of the refractive component decreases with decreasing frequency, but the characteristic time scale increases with decreasing frequency. Experimental dependences for the modulation index m_{ref} and the time scale T_{ref} for refractive scintillations as

functions of the dispersion measure DM were obtained in [12] based on observed flux variations at 610 MHz. For example, for DM = 32 pc/cm^3 at 610 MHz, we have $m_{ref} = 0.4$ and $T_{ref} = 5$ d. Adopting a Kolmogorov turbulence spectrum for the interstellar plasma, in agreement with the observational data of [12], we find for the refractive-scintillation index

$$m_{ref} \cong 0.4(f/600 \text{ MHz})^\gamma \cong (f/3 \text{ GHz})^\gamma,$$
$$\gamma = (4-n)(n+2)/[2(n-2)] \cong 0.56. \qquad (6)$$

We obtain for the time scales for refractive scintillations for the two velocities of the line of sight relative to the interstellar medium indicated above

$$T_{ref} \cong 0.2(f/3 \text{ GHz})^{-\delta} \text{ days}, \quad V = 150 \text{ km/s},$$
$$T_{ref} \cong (f/3 \text{ GHz})^{-\delta} \text{ days}, \quad V = 30 \text{ km/s}, \qquad (7)$$
$$\delta = n/(n-2) \cong 2.2.$$

Using the frequency dependences presented above, we expect $m = 0.5$ at 4.86 GHz and $m = 0.23$ at 8.46 GHz, in fairly good agreement with the values derived from the observations. We will have for the time scale of the scintillations $t = 2$ h at 4.86 GHz and $t = 1.3$ h at 8.46 GHz for $V = 150$ km/s, and $t = 10$ h and $t = 6.5$ h at 4.86 and 8.46 GHz, respectively, for $V = 30$ km/s. The expected time scale for refractive scintillations at 1.43 GHz is $t = 5$ d for $V = 30$ km/s, and the corresponding time scale for diffractive scintillations is $t_{dif} = 16$ h.

4. COMPARISON OF THE RADIO FLUX VARIATIONS OF VLA J065349.4 + 791619 WITH SCINTILLATIONS

On the whole, the observed flux variations resemble variations in pulsars associated with interstellar scintillations. However, the observed flux variations of VLA J065349.4 + 791619 cannot be refractive scintillations at all three frequencies for two reasons. First, we cannot shift our estimate of the critical frequency f_{cr} presented above very much toward higher frequencies, since the high-frequency modulation index should then be substantially higher than observed. Second, the high degree of correlation between the fluctuations at the widely spaced frequencies of 4.86 and 8.46 GHz, as well as the frequency dependence of the modulation index, is in contradiction with the hypothesis that the observed flux variations are the result of refractive scintillations.

We can see that a refractive-scintillation regime is realized at 1.43 GHz, since the time scale for diffractive scintillations (~16 h) is substantially longer than the time scale for the observed variations. Measurements on neighboring days yield appreciably smaller flux variations than measurements separated by ≥10 d, which provides a lower limit $t > 2$ d. As noted above, the expected time scale for refractive scintillations is about five days, in good agreement with the observations. We conclude that the flux variations correspond to weak scintillations
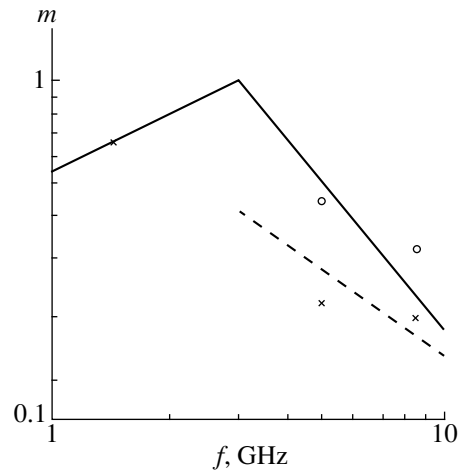
Fig. 1. Dependence of the modulation index m on frequency f. The solid curve shows a model for a point source, and the dashed curve a model for a source with size determined by (10). The circles present the data for the first time interval studied, and the crosses the data for the second interval.

at frequencies $f_2 = 4.86$ GHz and $f_3 = 8.46$ GHz and to refractive scintillations at $f_1 = 1.43$ GHz.

Figure 1 shows a theoretical curve for the frequency dependence of the modulation index for a point source (solid curve). The circles show the observational data for VLA J065349.4 + 791619 for the first time interval. On the whole, the theoretical curve and observations are in good agreement. In the second interval, the observational data (crosses) lie below the theoretical curve for a point source. We suggest that, in the second interval, the radio source had a finite angular size φ_0 exceeding the angular size of the first Fresnel zone

$$\varphi_{Fr} = (1/kR)^{1/2}. \qquad (8)$$

At frequency f_2, we have $\varphi_{Fr} \cong 2.1$ microarcsecond (μas). For a source of finite angular size with $\varphi_0 > \varphi_{Fr}$ in a weak-scintillation regime, repeating the calculations of [13], we can write the scintillation index in the form

$$m \cong m_0(\varphi_{Fr}/\varphi_0)^\gamma, \quad \gamma = (6-n)/2 = 7/6, \qquad (9)$$

where m_0 is the scintillation index for a point source. Here, we take φ_0 to correspond to the diameter of the source. The best agreement with the observed flux variations as interstellar scintillations is obtained if the angular size of the source grows with increasing wavelength.

In Fig. 1, the dashed curve shows the theoretical dependence

$$\varphi_0 = 5.8(3 \text{ GHz}/f) \text{ μas}. \qquad (10)$$

In this case, the angular size of the source will have a fairly weak influence at frequency f_3. On the whole, the theory and observations are in good agreement.

Figure 2 shows theoretical curves for the frequency dependence of the scintillation time scale for the two
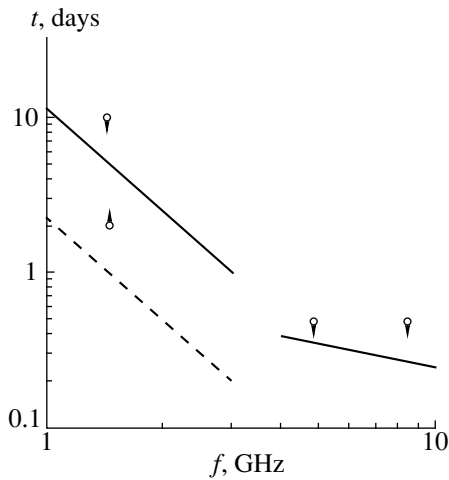
t, days

Fig. 2. Dependence of the characteristic time scale for scintillations t_0 on frequency f. The solid curve shows a model for velocity $V = 30$ km/s, and the dashed curve a model for $V = 150$ km/s. The circles show estimates derived from the observational data.

velocities V indicated above for a point source, in accordance with (4) and (7). The circles show estimates of the observed time scales for the flux variations of the radio source VLA J065349.4 + 791619. The observations are in fairly good agreement with the theoretical prediction for a velocity of the line of sight relative to the medium $V = 30$ km/s.

Further, we consider in more detail possible restrictions on the source parameters if the source is located at various distances from the observer. Although an optical absorption line has been detected in the direction of GRB 970508, yielding a redshift $z \geq 0.84$ [6], the distance of the gamma-ray burst source is not conclusively determined, since there is some significant probability that the optical emission is not physically associated with the burst. Therefore, we cannot exclude the possibility that the source is at a noncosmological distance.

(1) *Cosmological distance.* For the sake of definiteness, we adopt a distance for the source $L = 10^{28}$ cm. The source flux varied over a time of the order of a month ($T = 30$ d); there is no doubt that this is the time scale for intrinsic variability of the source itself, since such variability cannot be explained as the effect of scintillation. Taking the velocity in the source equal to the speed of light c, we obtain an upper limit for the source angular size

$$\varphi < \varphi_{max} = cT/L \cong 2 \ \mu as. \tag{11}$$

There is not doubt that a source with this size should scintillate on inhomogeneities of the interstellar plasma; in this case, interstellar scintillation is the only mechanism that can explain flux variations with a characteristic time scale of a day or less. Our conclusion that the source was unresolved in the first time interval is consistent with the size estimate (11).

The growth of the angular size of the source to $4 \ \mu as$ in the transition from the first to the second time interval over about 30 days suggests the presence of relativistic motions in the source. The characteristic linear size of the source in the second interval is

$$l \cong \varphi R \cong 10^{17} \ cm. \tag{12}$$

This size is too large for the radio and gamma-ray emission to originate in the same volume. If the gamma-ray emission arises in a compact volume, then induces radio emission in a substantially larger volume, the time for propagation of the perturbation should be no more than five days, and the apparent speed of propagation should be superluminal, of the order of $7c$. This is fully consistent with modern fireball models.

(2) *Distance $L \cong 30$ Mpc.* In this case, the linear size of the source in the first time interval is $l \cong 10^{15}$ cm. This size doubles over about 30 days, corresponding to a perturbation propagation speed $V \cong 3800$ km/s. Overall, these parameters correspond to those of supernova outbursts.

(3) *Distance $L \cong 3$ kpc.* If interstellar scintillations give rise to the observed fluctuations, this implies that the size of the source is $l \cong 10^{11}$ cm, and the perturbation propagation velocity is $V \cong 0.3$ km/s. This value is unrealistically small, since material should be torn off an object with a mass of the order of a solar mass with a velocity of hundreds of km/s. In addition, in this case, the flux variations must be intrinsic to the source if the source size is an order of magnitude larger than the estimate presented above.

(4) *Distance $L \cong 100$ pc.* In this case, the gamma-ray burst source could be an old pulsar, as proposed by Komberg and Kompaneets [14]. For such sources, it is difficult to explain the flux variations as the effect of scintillations, since the critical frequency should be substantially lower than 3 GHz; in addition, a velocity of $V \cong 30$ km/s is unrealistically small for pulsars. However, there remains the possibility that the observed fluctuations are intrinsic to the source.

5. CONCLUSION

We have analyzed the frequency dependences of the modulation index and time scale for radio flux variations of VLA J065349.4+791619. Our results, as well as the good correlation between the variations at the two higher frequencies studied, indicate that the fluctuations can be described well as the effect of interstellar scintillations. At frequencies $f_2 = 4.86$ GHz and $f_3 = 8.46$ GHz, the scintillations are weak, while the fluctuations at $f_1 = 1.43$ GHz correspond to the refractive component of saturated scintillations. The source must have an angular size (diameter) of about 2 μas at 4.86 GHz and expand with a speed of about 25 $\mu as/yr$. We have also demonstrated that, in order to explain the observed flux variations, the angular size of the source must grow linearly with frequency.

The observed flux variations at the three frequencies studied are most consistent with the source being extragalactic. It is unlikely that the source is Galactic, since it should then be some kind of known object. If the detected optical object is physically associated with the gamma-ray burst, then, of the two possible models for an extragalactic source—a supernova explosion at a distance $R \cong 30$ Mpc and a source at a cosmological distance—the cosmological-distance scenario is preferred. The observed radio flux variations are in good agreement with this latter scenario.

ACKNOWLEDGMENTS

REFERENCES

1. B. M. Belli, Astrophys. Space Sci. **231**, 43 (1995).
2. V. G. Kurt and B. V. Komberg, Astron. Astrophys. Trans. **8**, 89 (1995).
3. D. Q. Lamb and J. M. Quashock, Mon. Not. R. Astron. Soc. **265**, L45 (1993).
4. V. V. Usov and G. I. Chibisov, Astron. Zh. **52**, 192 (1975) [Sov. Astron. **19**, 115 (1975)].
5. E. Costa *et al.*, Nature **387**, 783 (1997).
6. J. S. Bloom, S. G. Djorgovski, S. R. Kulkarni, and D. A. Frail, Astrophys. J. Lett. **507**, L25 (1998).
7. H. Bond, IAU Circ. 6654 (1997).
8. D. A. Frail, S. R. Kulkarni, L. Nicasto, *et al.*, Nature **389**, 261 (1997).
9. J. Goodmen, New Astron. **2**, 449 (1997).
10. T. J. Galama, M. J. Wijers, M. Bremer, *et al.*, Astrophys. J. Lett. **500**, L101 (1998).
11. V. M. Malofeev, V. I. Shishov, W. Sieber, *et al.*, Astron. Astrophys. **308**, 180 (1994).
12. T. V. Smirnova, V. I. Shishov, and D. R. Stinebring, Astron. Zh. **75**, 866 (1998) [Astron. Rep. **42**, 766 (1998)].
13. V. I. Shishov, Pis'ma Astron. Zh. **15**, 975 (1989) [Sov. Astron. Lett. **15**, 425 (1989)].
14. B. V. Komberg and D. A. Kompaneets, Astron. Zh. **74**, 690 (1997).

Translated by D. Gabuzda

Physical Conditions in Photodissociation Regions from Observations of Carbon Radio Recombination Lines and IR Fine-Structure Lines of CII and OI

R. L. Sorochenko and A. P. Tsivilev

Lebedev Institute of Physics, Russian Academy of Sciences, Leninskiĭ pr. 53, Moscow, 117924 Russia
Received June 16, 1999

Abstract—Observations of the C56α line—the first carbon radio recombination line in the millimeter waveband—in the directions of the Orion Bar, NGC 2024, and W3 are reported. The results are analyzed together with data for the IR fine-structure lines of CII and OI, enabling unambiguous determination of the temperature and density in the photodissociation regions separating the HII regions and parent molecular clouds. © *2000 MAIK "Nauka/Interperiodica".*

1. INTRODUCTION

Photodissociation regions (PDRs) are formed at the surfaces of molecular clouds irradiated by UV emission with $\lambda > 912$ Å. The UV emission can be either background, from distant OB stars, or local, from an HII region that has formed in the molecular cloud and is part of the same complex. The radiation is stronger in the latter case, and PDRs at the boundaries between molecular clouds and HII regions are found much more frequently than PDRs due to background radiation. Under the action of UV radiation, the molecules in a PDR are dissociated, and atoms with ionization potentials lower than that of hydrogen are ionized. The most abundant of these are atoms of carbon, for which $V_{ion} = 11.3$ eV.

The first information about PDRs was obtained from radio recombination lines (RRLs) of carbon detected toward some HII regions [1, 2]. They testified to the existence of CII regions and, at the same time, stimulated searches for the $^2P_{3/2}$–$^2P_{1/2}$ C$^+$ line at 158 μm, which theories predicted should play a major role in the cooling of gas clouds. This line was detected by Russell *et al.* [3] after the construction of a high-resolution IR spectrometer.

Investigations of PDRs are important for studies of star formation processes, since they yield valuable information about the action of the UV radiation from young, newly formed stars on the parent molecular cloud. Numerous observations in the above lines have been carried out; however, the PDR physical conditions derived from them have been determined with only poor accuracy. In particular, the derived PDR temperatures toward Orion A vary from 50 K [4] to ~300 K [5], and even 500–1000 K [6].

The aim of the present study is to obtain new, more accurate data about the physical conditions in PDRs. For this purpose, we have made two important steps.

(1) We extended observations of carbon RRLs, which had previously been limited to centimeter and longer wavelengths, to the millimeter range, which provides a number of advantages. First, the ratio of the brightness temperature in the carbon RRL to the HII-region continuum radiation within the radio telescope beam grows in proportion to the frequency, increasing the reliability of the line measurements. Second, the RRL intensity is determined only by spontaneous transitions (stimulated emission is minor and can be neglected), and the line optical depth is ≪1. These circumstances considerably simplify interpretation of the observations and enable us to draw more specific conclusions.

(2) Our analyses were based on comparisons of observations of the carbon RRL and of the IR fine-structure lines of carbon CII (158 μm) and oxygen OI (63 μm and 146 μm). As targets for the observations, we chose PDRs for which these IR lines have been detected: the Orion Bar, NGC 2024, and W3.

2. OBSERVATIONS AND RESULTS

The observations were carried out in the 8-mm band on the 22-meter radio telescope of the Lebedev Institute of Physics. The beamwidth was 1.9′. The front-end cooled transistor amplifier yielded a system noise temperature of 220 K. A 128-channel filter-bank spectrum analyzer with a resolution of 125 kHz (1 km/s) was used. We observed hydrogen H56α (36466.27 MHz), helium He56α (36481.11 MHz), and carbon C56α (36484.47 MHz) RRLs. The observations were carried out using a symmetric beam-switching method: the radio telescope was alternately directed toward the region studied using each of the two beams, separated by 23 arcmin. Individual spectrograms were recorded over 6 min (3 min for each beam) and then averaged. To obtain an acceptable signal-to-noise ratio, the signal integration time for each source was tens of hours.

Table 1. Observed RRL parameters

Source	$\alpha_{1950}\ \delta_{1950}$	Line	t_{int}, h	T_L, K	ΔV_L, km/s	$\Delta\nu$, 10^3 Hz	V_{lsr}, km/s
Orion Bar	$5^h32^m55^s$	H56α	4.4	0.800(0.030)	27.5(1.0)	3340(117)	−0.65(0.4)
	−5°26′30″	He56α	31.5	0.137(0.011)	20.9(2.0)	2534(200)	−0.47(0.6)
		C56α	31.5	0.081(0.014)	3.41(0.9)	415(100)	10.54(0.3)
NGC 2024	$5^h39^m13^s$	H56α	15.3	0.240(0.009)	28.8(1.3)	3500(150)	7.0(0.5)
	−1°57′00″	He56α	54.4	0.051(0.006)	11.4(1.7)	1390(200)	5.7(0.6)
		C56α	54.4	0.069(0.007)	6.1(1.1)	740(100)	11.2(0.4)
W3	$2^h21^m52^s$	H56α	22.1	0.331(0.017)	27.6(1.3)	3350(150)	−42.3(0.4)
	61°52′39″	He56α	94.7	0.058(0.006)	14.6(1.9)	1775(230)	−43.4(0.7)
		C56α	94.7	0.038(0.007)	6.7(1.6)	814(200)	−41.9(0.6)

Figure 1 shows the resulting spectra. Due to the limited analysis bandwidth, the hydrogen line was observed separately from the lines of helium and carbon. We estimated the line parameters by fitting Gaussian profiles, listed in Table 1. This table presents the source name, positions observed, RRL notation, integration time, brightness temperature, line FWHM on velocity and frequency scales, and the line radial velocity with respect to the Local Standard of Rest.

3. COMPARISON OF THE RRL AND IR LINE INTENSITIES

It is very difficult to determine the physical conditions in PDRs using RRL observations alone, since this requires data on many lines obtained over a wide frequency band. The problem can essentially be avoided by combining observations of carbon RRLs and the IR

158-μm line [6, 7]. Both types of lines are due to the same carbon ions, which radiate the RRLs during recombination to excited levels and subsequent cascade transitions, and emit the 158-μm IR line during transitions between the $^2P_{3/2}$–$^2P_{1/2}$ fine-structure levels. For this reason, the RRLs and 158-μm line form in the same spatial regions, but their intensities have different dependences on the physical conditions.

In the optically thin case, the intensity of the 158-μm line is proportional to the *first power* of the density, while the RRL intensity is proportional to the density *squared*. As a result, the ratio of the RRL and 158-μm intensities enables us to estimate the electron density as a function of temperature: $N_H = f(T)$. In the general case, without assuming small optical depth, the functional relation between the electron temperature and density is [7]

$$N_H = \frac{2.33 \times 10^5 \Delta\nu_L T_L \alpha_{1/2} \beta_{158} T^{1.5} \exp(-1.58 \times 10^5/n^2 T)}{b_n \Delta\nu_{158}\left(1 - \frac{\beta_n T_{bg}}{T}\right)\ln\left[\frac{\exp(91.2/T_{158}) - 1}{\exp(91.2/T_{158}) - \exp(91.2/T_{ex,\,158})}\right]}, \tag{1}$$

where $\Delta\nu_L$ and T_L are the measured total width and brightness temperature of the carbon RRL in Hz and K, respectively; $\Delta\nu_{158}$ and T_{158} are the total width and brightness temperature for the carbon 158-μm line; and $T_{bg} = 3.55 + T_c$ is the background brightness temperature, where T_c includes the emission of the HII region if it lies behind the PDR. The term $\beta_n T_{bg}/T$ describing stimulated emission can be neglected at millimeter wavelengths. The factor b_n accounting for deviation of the populations of the excited carbon levels from thermodynamic equilibrium was calculated for various temperatures and densities in [8]; these calculations were later extended to higher values of T and N_H. The

factors $\alpha_{1/2}$ and β_{158} and the excitation temperature $T_{ex,\,158}$ are obtained in the Appendix. When deriving (1), we took the cosmic abundance of carbon to be $N_C = 3 \times 10^{-4} N_H$ and assumed that the carbon in PDRs is completely ionized and all the electrons have formed from this ionization; i.e., $N_C = N_{C^+} = N_e$.

We used data on the CII 158-μm line obtained by the Kuiper Airborne Observatory in the comparison with the carbon RRL observations. These data are listed in Table 2. Maps of the 158-μm-line intensity with angular resolution 55″ were smoothed to 2′ for comparison with the C56α observations. The 158-μm line was not
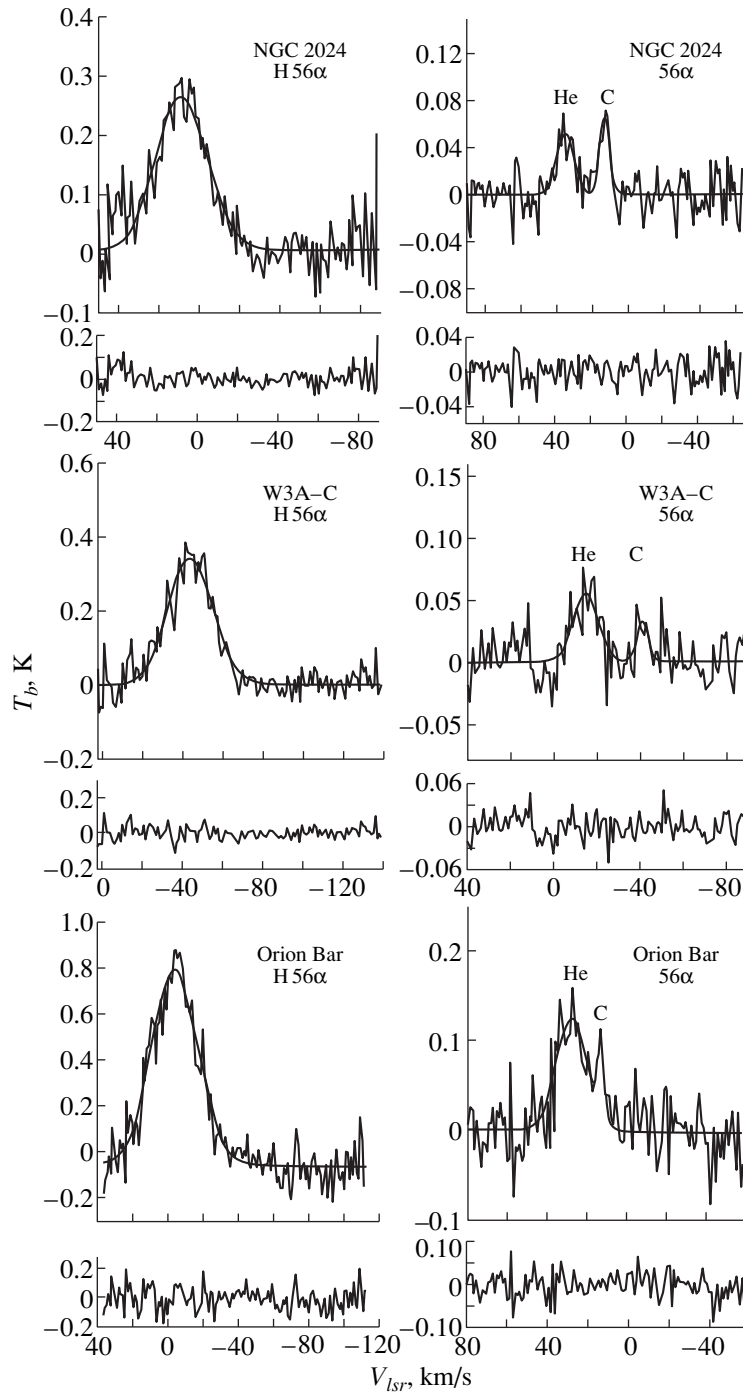
Fig. 1. Spectrograms of the C56α RRLs of H, He, and C with the fitted Gaussian profiles. The residual baselines remaining after fitting are drawn under each spectrum. The horizontal axis plots velocity with respect to the Local Standard of Rest for hydrogen (spectra at the left) and carbon (spectra at the right); the vertical axis plots brightness temperature. The lines of hydrogen and helium are emitted by HII regions, and the carbon lines, by photodissociation regions.

spectrally resolved, and its width was not measured. We took it to be equal to the width of the C56α line multiplied by a broadening factor due to the optical depth when $\tau_{158} \geq 1$ (see below). For the source NGC 2024,

taking into account data for other carbon RRLs [9], in which most observations have yielded a smaller line width, we adopted the value obtained by us minus the error.

Table 2. Observational data used in the comparison of the C56α and the CII and OI IR line intensities

Source	C56α		CII 158 μm			OI I, erg/(cm^2 s ster)	References
	ΔV_L, km/s	$\Delta \nu_L T_L$, Hz K	I_{158}, erg/(cm^2 s ster)	$\Delta \nu_{158}$, 10^6 Hz	T_{158}, K		
Orion Bar	3.41	33.6	3.5 s	24.7	161	2.25×10^{-3} (146) s	[13]
NGC 2024	5	41.9	2.7			6.7×10^{-3} (63)	[14, 15]
			2.2 s	36.3	90		
W3	6.7	30.9	3.1 s	42.5	100	1.5×10^{-3} (146) s	[16]

Note: The numbers in parentheses in column OI, (63) and (146), indicate that the observations were carried out at wavelengths 63 μm and 146 μm, respectively. A superscript "s" indicates that the intensity data were smoothed to 2′.

We determined the brightness temperature in the 158-μm line from its integrated intensity and width [see (A7)]:

$$T_{158} = \frac{91.2}{\ln\left(1 + 1.08 \times 10^{-10}\dfrac{\Delta\nu_{158}}{I_{158}}\right)}. \qquad (2)$$

Table 2 lists the brightness temperatures obtained for the 158-μm line from its intensity and width.

The ambiguity between N_H and T that follows from (1) for the C56α and CII 158-μm lines can be resolved by also considering data for oxygen IR lines. The oxygen in PDRs is mainly atomic. The widespread CO molecules, with a dissociation energy of 11.09 eV, and other oxygen-bearing molecules in molecular clouds are destroyed in PDRs by dissociation. At the same time, there is no ionization of oxygen: its ionization potential somewhat exceeds that of hydrogen. The ground state of atomic oxygen is split into three fine-structure levels: $^3P_2$ (lower), $^3P_1$, and $^3P_0$ (upper). During their $^3P_1$–$^3P_2$ and $^3P_0$–$^3P_1$ transitions, oxygen atoms radiate spectral lines at 63 and 146 μm, respectively.

The cross sections for collisional excitation of the C$^+$ fine-structure levels due to collisions with hydrogen atoms [10] exceed those for OI by one to two orders of magnitude [11]. Therefore, when $N_H \geq 3 \times 10^4$ cm^{-3}, the fine-structure levels of carbon are already thermalized and the intensity of the CII 158-μm line is independent of the density; in contrast, there is no thermalization of the oxygen fine-structure levels for $N_H = 10^4$–10^6 cm^{-3}, and the intensities of the oxygen IR lines depend on the density [12]. Hence, the line intensity ratios I(CII 158 μm)/I(OI 63 μm) and I(CII 158 μm)/I(OI 146 μm) depend on the density, and these dependences can be used to resolve the ambiguity in the physical conditions in the PDR.

The data for the OI lines we used in the analysis are also listed in Table 2, which presents the source name; line width obtained from the C56α observations; product of the width and brightness temperature of the C56α line; intensity, width, and brightness temperature of the CII 158-μm line; intensities of the OI 63- and 146-μm lines; and references for the IR-line data.

For the Orion Bar and W3, for which we had maps, the data were smoothed to 2′. In W3, only one oxygen line, OI 146 μm, was observed [16]. We used this same line for the analysis of the Orion Bar, for which both oxygen lines (63 μm and 146 μm) were observed [13]. In NGC 2024, for which only the 158-μm line was mapped, we used data with resolution 55″ [14, 15] for the comparison of the CII and OI line intensities.

Figure 2 presents the results of our comparison of the line intensities, which yields the functional relationships between the density and temperature. Figure 2a also shows the comparison for the PDR in NGC 2024. We obtained the $N = f(T)$ curve for C56α/CII(158) using (1). To derive the second curve for CII(158)/OI(63), we calculated the line intensity ratio as a function of temperature for various hydrogen densities (see Appendix) and compared the calculation results with the measured value of I(CII 158 μm)/I(OI 63 μm) = 0.4. The resulting $N = F(T)$ dependence is shown in Fig. 2a.

The key factor in this analysis is using spectral lines having different physical natures. The formation of RRLs is based on the recombination process, for which the line intensities are proportional to the square of the density, as noted above. Furthermore, since recombination determines the populations of excited levels, the RRL intensity decreases rapidly with increasing temperature ($\sim T^{-1.5}$). At the same time, the intensity of the fine-structure lines increases with temperature. Therefore, the C56α/CII (158) curve has a positive gradient: higher densities correspond to higher temperatures.

The ratio of the intensities of the IR lines of carbon and oxygen has a different dependence. Both lines have the same nature and are characterized by the same mechanism for population of the upper levels—collisions with hydrogen. For this reason, the intensities of both lines grow with temperature and density, but at different rates: slower in carbon and faster in oxygen. Therefore, for a constant intensity ratio, the gradient of the $N_H = F(T)$ curve is negative: lower densities correspond to higher temperatures. By virtue of these behaviors, the two curves in Fig. 2a intersect, enabling us to determine the PDR's temperature and density from the intersection point.
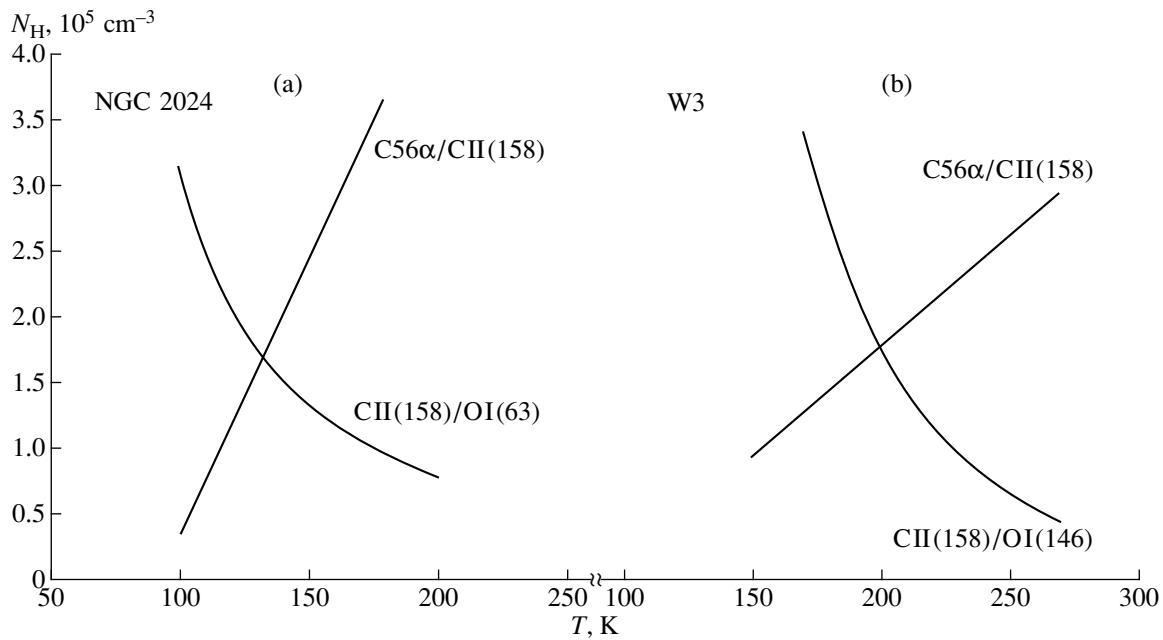
Fig. 2. Comparison of observations of the carbon C56α RRL and the IR lines of CII 158 μm, OI 146 μm, and OI 63 μm. The point of intersection of the two curves determines the PDR temperature and density.

Figure 2b shows the results for the PDR toward W3. Here, as in the previous case, we determined the $N_H = f(T)$ curve from the C56α and CII 158-μm lines using (1), using the OI 146-μm line instead of the OI 63-μm line in the calculation of the second curve. The 146-μm line is weaker than the 63-μm line, and its intensity can be calculated for the optically thin case using the relation [see (A17)]

$$I_{146} = \frac{A_{01}h\nu\alpha_0 \times 5 \times 10^{-4} N_H L}{4\pi} \ \text{erg/(cm}^2 \ \text{s ster)}, \quad (3)$$

where A_{01} is the probability of spontaneous transitions between the $^3P_0$ and $^3P_1$ levels, ν is the transition frequency, α_0 is the relative population of the $^3P_0$ level, and L is the PDR's line-of-sight depth.

Using the OI 146-μm line instead of the OI 63-μm line does not change the overall procedure for the analysis. As in the previous case, Fig. 2b shows two intersecting curves whose gradients have opposite signs. Thus, combining the observations of the RRLs and the CII and OI IR lines enables us to unambiguously determine the basic physical conditions in the PDRs.

In our analysis, we took into consideration and, wherever possible, allowed for a number of factors affecting the intensities of the IR lines. We took into account the fact the hydrogen is not atomic throughout the PDR but only in a layer adjacent to the HII region with visual extinction $A_v = 2–3$; at greater distances from the boundary with the HII region, the hydrogen becomes molecular [12]. The rates of excitation of the C^+ and O fine-structure levels by collisions with atoms [10, 11] and molecules [17, 18] of hydrogen are differ-

ent, which affects the level populations. These circumstances can be neglected for the CII 158-μm line: as a rule, the PDR density thermalizes the levels. In addition, at densities to $N_H > 10^6$ cm^{-3}, the intensities of oxygen fine-structure lines formed in media where hydrogen is atomic or molecular are somewhat different. The transition from atomic to molecular hydrogen takes place approximately at the half-thickness of the PDR layer [12]. Based on these considerations, we adopted a mean $N_H = F(T)$ curve between the curves for fully atomic and fully molecular hydrogen.

In our calculations for the OI 63-μm and CII 158-μm lines, we did not assume small τ for lines having appreciable optical depths. In NGC 2024, $\tau_{63} \sim 3$ and $\tau_{158} \sim 1$. In the Orion Bar, too, τ_{158} is ~1. At such optical depths, the lines are broadened by factors of 1.14 (τ = 1) and 1.47 (τ = 3). We took this into account when determining the width and brightness temperature of the CII 158-μm line from the intensity (2) and in calculations of the line intensity ratio I_{158}/I_{63} using relationships (A7) and (A16). In the OI 146-μm lines in the Orion Bar and W3, $\tau_{146} \ll 1$, substantially simplifying the analysis. For this reason, we used this oxygen line instead of the more intense OI 63 μm line in our analysis for the Orion Bar. Due to the mutual dependence between the temperature, density, and optical depth, we determined self-consistent physical conditions for the PDRs that were also consistent with the observations in an iterative fashion.

We neglected the fact that the depth of the OI region could somewhat exceed that of the CII region. The reason for this is that the carbon at the boundary of the CII region (at $A_v = 4–5$), which is mainly in the form of CO

Table 3. Physical conditions in the PDRs

| Source | HII region | | PDR | | | References | | |
| | exciting star | N_e, cm^{-3} | T, K | N_e, cm^{-3} | N_H, cm^{-3} | HII region | | PDR |
						exciting star	N_e	
Orion Bar	O6	10^4	215	39	1.3×10^5	[21]	[22]	This work
W3	O5–O6	1.7×10^4	200	54	1.8×10^5	[23]	[23]	"
NGC 2024	O9.5	1.9×10^3	132	51	1.7×10^5	[21]	[24]	"
S140/L1204	BOV	10	67–85	3	$\sim 10^4$	[25]	[7]	"
Cas A	–		50	0.15	5×10^2			[20]

molecules, does not bind all the oxygen, which is more abundant. There are no quantitative calculations available for this case. A qualitative estimate suggests that this effect could slightly lower the values of T and N_H obtained for the PDRs, but by no more than 10–15% in temperature and 20–30% in density.

4. THE PHYSICAL CONDITIONS IN THE PHOTODISSOCIATION REGIONS

Table 3 lists the physical conditions in the PDRs derived by comparing the carbon RRL observations with the data for the IR lines of CII and OI. The two columns after the source name describe the HII region adjacent to the PDR: the spectral type of the exciting star and the electron density. Further, the PDR parameters are listed: temperature, electron density, and density of hydrogen atoms. The last three columns give references and sources of information.

In addition to the objects observed in the C56α line, we have included two more sources for which we have determined PDR physical conditions. We obtained the $N_H = f(T)$ dependence for S140/L1204 earlier using the ratio of the C165α–C166α RRLs and the CII 158-μm-line intensities. This dependence yielded $T = 75$–200 K and $N_e = 0.5$–9 cm^{-3} ($N_H = 1600$–3×10^4 cm^{-3}) [7]. New data on the OI 63-μm line for this source [19] enabled us to find unambiguous values of T and N_H using the method described above.

The other additional source is a molecular cloud (or clouds) toward Cas A. The nature of the PDR here is different from that of the remaining PDRs in Table 3. There are no HII regions in the direction of Cas A, and the PDR is formed by background UV emission. There are no observations of the CII and OI IR lines for this PDR, but the available data on the carbon RRLs are unique. The molecular cloud is seen against the background of a powerful source, and carbon lines have been observed over a very broad range of radio wavelengths from 21 cm to 15 m, both in emission at λ < 3 m and in absorption at λ > 3 m. This enabled us to determine the physical conditions in the PDR using the carbon RRL data alone [20].

Let us now consider some features of the individual sources in more detail.

The Orion Bar. The Orion Bar photodissociation region formed in the Orion A molecular cloud, among the best-studied astronomical objects. It represents an intermediate layer between the cloud and an HII region that formed at the nearest surface of the cloud under the action of the star θ^{1}Ori. The HII region and PDR both have a cuplike shape, with the cup axis slightly inclined to the direction toward the observer. In the Orion Bar region ~2′ southeast from θ^{1}Ori, the plane of the PDR layer is almost parallel to the line of sight, and the boundary between the HII region and molecular cloud is seen almost edge-on. The depth of penetration of the HII region into the molecular cloud is ~0.6 pc [26], and the thickness of the PDR layer in the C91α line is ~20″ (0.05 pc) [27].

The electron density of the HII region (the well-known Orion Nebula) has been measured directly from the Stark broadening of the hydrogen RRL: $N_e = (1 \pm 0.3) \times 10^4$ cm^{-3} [22], and the temperature was derived from the ratio of the intensities of this line and the continuum: $T = 8000 \pm 100$ K [28]. The ^{12}CO and ^{13}CO data indicate that the molecular gas adjacent to the PDR is primarily in the form of a uniform medium with hydrogen density $N_H \sim 5 \times 10^4$ cm^{-3}. Embedded in this medium are several, slightly denser clumps ($N_H > 10^6$ cm^{-3}), which do not play a major role in determining the physical conditions in the PDR. According to the same measurements, the temperature of the molecular cloud, which is ~30 K in its interior, grows to ~90–120 K toward the boundary with the PDR [29].

The temperature $T = 215$ K we have obtained for the PDR corresponds to the expected value as we approach the ionization front. However, we should bear in mind that this temperature is the mean over the entire depth of the PDR. The density of the PDR, which is higher than the densities of both the hotter HII region (as is natural) and the cooler molecular layer, probably testifies to pressure from the HII region on the molecular cloud.

The PDR temperature and density from Table 3 are close to $T = 220$ K and $N_H = 3 \times 10^5$ cm^{-3}, obtained for the Orion Bar from IR lines and the CO line in [13]. At the

N_H, cm^{-3}
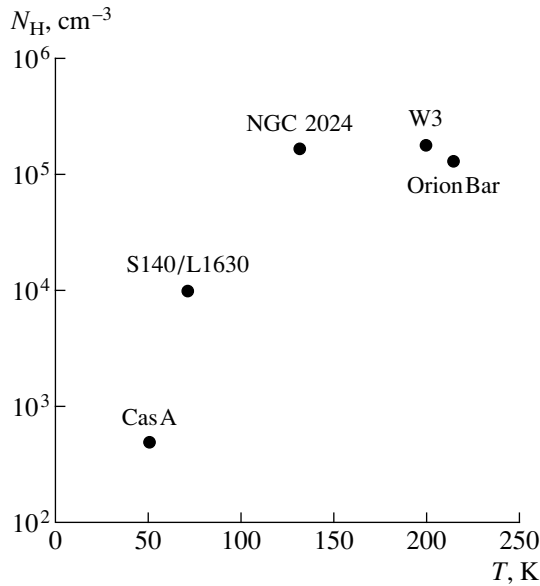
Fig. 3. PDR temperature and density.

same time, the appreciably higher values $N_H = 10^6$ cm^{-3} and $T > 400$ K were obtained by Natta *et al.* [6] by combining observations in the C91α and CII 158-μm lines. This discrepancy can be explained by the fact that, when interpreting their results on the RRL, Natta *et al.* [6] took carbon to be hydrogen-like without considering dielectronic recombination. As a result, the calculated b_n factor was underestimated and N_H [see (1)] was overestimated. It is interesting that early but sensitive and high-resolution (1'.3) observations in the C75α line suggested that the temperature of the CII region in the Orion Bar could not exceed 50 K [4]. This conclusion, which is at variance with our work and observations of the brightness temperatures of the CII 158-μm and OI 63-μm lines [30] ($T_B > 100$ K), reflects the difficulties in determining the physical conditions in PDRs from observations of a single carbon RRL.

NGC 2024. In contrast to the Orion Bar, the PDR layer in NGC 2024, which is on the near side of the molecular cloud L1630/Orion B, lies in the plane of the sky, not along the line of sight. For this reason, the PDR is rather large. It is 2' (~0.3 pc) in the C76α line [31], and even larger—6' × 7'(~0.8 pc) [32]—in the CII 158-μm line.

The mean density of the molecular cloud derived from the CO line, N_{H_2}, is ~10^3 cm^{-3} [32]. In NGC 2024, as in the Orion Bar, the density in the PDR is appreciably higher than in the parent molecular cloud. Earlier, only estimates of the temperature and density in the PDR were available. Observations in the CII 158-μm, C109α, and C137β lines yielded $T \sim 100$ K [3, 33] and $N_H \sim 10^5$ cm^{-3} [33], which are close to the values obtained in the present work.

W3. The W3 complex is a molecular cloud with an H$_2$ density of ~10^5 cm^{-3}; inside, closer to its far boundary, are the HII regions W3A–W3D [34]. The size of the region of CII 158-μm-line emission is ~3.5' (2.4 pc), with its center near W3B [35]. High-angular-resolution mapping in the C92α line revealed a thin (about 0.06 pc) CII envelope around this source [36]. The impossibility of explaining the large overall size of the CII region with a homogeneous distribution of material led Howe *et al.* [35] to propose a PDR model; which is consistent with observations with clumps having a density of ~10^5 cm^{-3} embedded in a dilute (≤300 cm^{-3}) medium with T is ≥100 K. In early measurements, based on the ratio of the C109α and C137β line intensities, Pankonin [33] obtained $T \sim 100$ K and $N_H \sim 10^5$ cm^{-3}.

S140/L1204. Recent mapping of the S140/L1204 region in the 158-μm line [19] showed that the line emission has two components. One, with angular size ~20', is associated with the PDR, which was observed in the C165α and C166α lines [7], while the other, smaller component is associated with the foreground IR source S140 IRS 1. Toward the 158-μm-line peak, where $I_{158} = 3.5 \times 10^{-4}$ erg s^{-1} cm^{-2} ster^{-1} [19], the PDR contributes only about one-third of the intensity. We were not aware of this when we compared the results for the RRL and the 158-μm line in [7], and the intensity of the CII 158-μm line adopted in our analysis was overestimated by a factor of three. As a result, the $N_H = f(T)$ curve obtained from (1) underestimated the PDR density.

Only an estimate of the ratio $I_{158}/I_{63} = 3$–10 in the direction of the PDR is available [19]. For this reason, the PDR temperature and density are determined to lower accuracy.

Figure 3 illustrates the results for the main PDR parameters—gas temperature and density. We can see that higher densities are observed in hotter PDRs. This is in good agreement with theory, which proposes that, in PDRs with higher density, the increase in heating due to photoemission leads the increase of cooling via line emission [12]. We can also see the relation between the physical conditions in the PDRs and the parameters of the ionization source. Higher temperatures and densities are typical of PDRs that have formed at the boundaries of HII regions excited by O stars. In S140/L1204, where the source of ionization is a B star, T and N_H are appreciably lower. The PDR in Cas A is an exception: its temperature and, especially, density are much lower than in the remaining sources. The reason is clear: this PDR has no nearby source of ionization, and the photodissociation region has probably formed under the action of background UV radiation.

5. CONCLUSION

Simultaneous analyses of a carbon radio recombination line and the CII 158-μm, OI 146-μm, and 63-μm IR fine-structure lines provide a means for effective study

of the physical conditions in photodissociation regions formed at the surfaces of molecular clouds, at boundaries with HII regions. The different natures of the two types of lines lead to different dependences of their intensities on the physical conditions in the PDR, including opposite temperature dependences; this makes it possible to unambiguously determine the PDR temperature and density. The resulting density (based on collisions and level populations) is the true density, not a volume-averaged value, as are densities derived from surface-brightness measurements.

For joint analyses with IR lines, it is best to use the millimeter carbon RRL, which has a number of advantages in comparison with longer wavelength lines (higher ratio of the line brightness to the continuum emission, small optical depth, etc.). The values of T and N_H obtained for several sources based on a joint analysis of observed RRL and IR lines are consistent with current theories of PDRs [12].

ACKNOWLEDGMENTS

APPENDIX

INTENSITIES OF THE CII 158-μm, OI 63-μm, AND OI 146-μm LINES

CII 158-μm line. To find the intensity of the $^2P_{3/2}-^2P_{1/2}$ CII line, it is necessary to calculate its optical depth and brightness temperature. According to [7],

$$\tau_{158} = \frac{A_{3/2-1/2}\lambda^2 g_{3/2}\alpha_{1/2}N_C + L\beta_{158}}{8\pi 1.06\Delta\nu_{158}g_{1/2}}$$
$$= \frac{1.34\times10^{-14}\alpha_{1/2}\beta_{158}N_H L}{\Delta\nu_{158}},$$
(A1)

where

$$\beta_{158} = 1 - \frac{\exp(-91.2/T)}{(1+R_{158})}$$
(A2)

is the contribution of stimulated emission and the factor $\alpha_{1/2}$ determines the fraction of carbon ions in the lower state (relative to their total density N_{C^+}):

$$\alpha_{1/2} = \frac{1+R_{158}}{(1+R_{158}) + 2\exp(-91.2/T)}.$$
(A3)

It is assumed that $N_{C^+} = N_C = 3\times10^{-4}N_H$. In formulas (A1)–(A3), $A_{3/2-1/2} = 2.4\times10^{-5}$ s^{-1} is the probability of spontaneous transitions between the $^2P_{3/2}$ and $^2P_{1/2}$ levels; $\lambda = 157.7\times10^{-6}$ cm is the wavelength; $\Delta\nu_{158}$ is the Gaussian line FWHM (Hz) for this transition; L is the

PDR line-of-sight depth; and $g_{3/2} = 4$ and $g_{1/2} = 2$ are the statistical weights of the upper and lower levels, respectively. The factor $1 + R_{158}$ describes the deviation of the fine-structure level population from thermodynamic equilibrium. Its value, which was investigated in [8], depends on the ratio of the probability of spontaneous transition $A_{3/2-1/2}$ and the rate of level $^2P_{3/2}$ deactivation by collisions with electrons and hydrogen atoms. Taking into account only collisions with hydrogen atoms, which play the main role, the value of R_{158} is [12]

$$R_{158} = \frac{A_{3/2-1/2}}{N_H\gamma_H} = \frac{2.4\times10^{-6}}{N_H\times5.8\times10^{-10}T^{0.02}}$$
$$= \frac{4.1\times10^3}{N_H T^{0.02}},$$
(A4)

where $\gamma_H = 5.8\times10^{-10}T^{0.02}$ is the rate of deactivation of the $^2P_{3/2}$ level by collisions with hydrogen atoms. For collisions with hydrogen molecules ($C^+ - H_2$), we have $\gamma_{H_2} = 3.1\times10^{-10} T^{0.1}$ cm^{-3} s^{-1} [12, 17]. The transition of hydrogen to molecular form must be taken into account when $N_H < 3\times10^4$ cm^{-3}.

The brightness temperature in the 158-μm line (T_{158}) is related to its optical depth as

$$T_{158} = \frac{91.2}{\ln\left[\dfrac{\exp(\tau_{158})\exp(91.2/T_{ex,158}) - 1}{\exp(\tau_{158}) - 1}\right]}, \quad \text{(A5)}$$

where

$$T_{ex,158} = \frac{91.2T}{91.2 + T\ln(1+R_{158})}$$
(A6)

is the temperature of excitation of the fine-structure levels. In accordance with the Planck law, the integrated intensity in a 158-μm line with width $\Delta\nu_{158}$ is

$$I_{158} = \frac{2h\nu_{158}\times1.06\Delta\nu_{158}}{[\exp(h\nu/kT_{158}) - 1]\lambda^2}$$
$$= \frac{1.08\times10^{-10}\Delta\nu_{158}}{\exp(91.2/T_{158}) - 1} \quad \text{erg/(cm}^2 \text{ s ster)}.$$
(A7)

OI 63-μm line. The intensity of the OI 63-μm line, whose optical depth, as a rule, exceeds unity, can be calculated in the same way as for the CII 158-μm line. Substituting the numerical values for the $^3P_1-^3P_2$ transition into (A1), namely, $A_{12} = 8.95\times10^{-5}$ s^{-1}, $\lambda = 63.2\times10^{-6}$ cm, statistical weights of the upper and lower levels $g_1 = 3$ and $g_2 = 5$, and an oxygen abundance $N_O = 5\times10^{-4}N_H$, we have

$$\tau_{63} = \frac{4\times10^{-14}N_H L\alpha_2\beta_{63}}{\Delta\nu_{63}},$$
(A8)

where

$$\beta_{63} = 1 - \frac{\exp(-228/T)}{(1 + R_{63})}, \qquad (A9)$$

α_2 is the fraction of oxygen atoms in the $^3P_2$ level, and $1 + R_{63}$ is a factor describing the deviation of the population of this level from its equilibrium value.

The values of α_2 and $1 + R_{63}$ can be found from the equations of balance of the three-level OI fine-structure system. Solving these equations, we find

$$\frac{n_1}{n_2} = \frac{N_H(\gamma_{20} + \gamma_{21})}{A_{12} + N_H\gamma_{12}}, \qquad (A10)$$

$$\frac{n_0}{n_2} = \frac{[\gamma_{10}N_H^2(\gamma_{20} + \gamma_{21}) + N_H\gamma_{20}(A_{12} + N_H\gamma_{12})]}{(A_{12} + N_H\gamma_{12})[A_{01} + N_H(\gamma_{01} + \gamma_{02})]}, (A11)$$

where n_0, n_1, and n_2 are the populations of the $^3P_0$, $^3P_1$, and $^3P_2$ levels, respectively; $A_{01} = 1.7 \times 10^{-5}$ s^{-1} is the probability of spontaneous transitions between the $^3P_0$ and $^3P_1$ levels (we did not include spontaneous transitions from the $^3P_0$ to the $^3P_2$ level in the equations of balance due to the small value of A_{02}); and γ is the rate of collisional excitation and deexcitation. For O–H collisions, we used the approximate formulas of [12] for the deexcitation rates of various transitions at gas temperature T: $\gamma_{01} = 1.5 \times 10^{-11}T^{0.44}$, $\gamma_{12} = 4.2 \times 10^{-12}T^{0.67}$, and $\gamma_{02} = 1.1 \times 10^{-12}T^{0.8}$ cm^3 s^{-1}. The collisional-excitation rates are related to the deexcitation rates as $\gamma_{lu} = \frac{g_u}{g_l} e^{\frac{-h\nu_{lu}}{kT}} \gamma_{ul}$, where the subscripts l and u denote the lower and upper levels, and g_l and g_u are their statistical weights. For O–H$_2$ collisions, we used the rates of collisional excitation and deexcitation tabulated in [18].

It follows from equations (A10) and (A11) that

$$\alpha_2 = \frac{1}{n_0/n_2 + n_1/n_2 + 1}. \qquad (A12)$$

The factor $1 + R_{63}$ is determined by the ratio of the equilibrium population of the triplet lower levels

$$\left(\frac{n_1}{n_2}\right)^* = \frac{g_1}{g_2}\exp(-228/T) \qquad (A13)$$

to the population calculated from the equation of balance (A10):

$$1 + R_{63} = \frac{g_1\exp(-228/T)}{g_2(n_1/n_2)}. \qquad (A14)$$

The subsequent procedure for calculating the line intensity I_{63} is similar to that used for the CII 158-μm line.

Using relationships (A6) and (A5) with the data for the 63-μm line

$$T_{ex, 63} = \frac{228T}{228 + T\ln(1 + R_{63})},$$

$$T_{63} = \frac{228}{\ln\left[\dfrac{\exp(\tau_{63})\exp(228/T_{ex, 63}) - 1}{\exp(\tau_{63}) - 1}\right]}, \qquad (A15)$$

we can determine the excitation temperature and line brightness temperature and, from formula (A7), the intensity:

$$I_{63\,\mu m} = \frac{1.67 \times 10^{-9}\Delta\nu_{63}}{[\exp(228/\tau_{63}) - 1]} \text{ erg/(cm}^2 \text{ s ster).} \quad (A16)$$

OI 146-μm line. Below densities $N_H < 10^6$ cm^{-3}, typical for PDRs, the upper level of the atomic-oxygen ground-state triplet $^3P_0$ is poorly populated. As a rule, the optical depth in the $^3P_0$–$^3P_1$ line is $\ll 1$, and its intensity can be determined from the formula

$$I_{146} = \frac{A_{01}h\nu\alpha_0 \times 5 \times 10^{-4}N_O L}{4\pi}, \qquad (A17)$$

where $\nu = 2.06 \times 10^{12}$ Hz is the transition frequency, N_O is the density of atomic oxygen, and $\alpha_0 = n_0/N_O$ is the fraction of oxygen atoms at the $^3P_0$ level. According to (A10) and (A11), this quantity is

$$\alpha_0 = \frac{n_0/n_2}{n_0/n_2 + n_1/n_2 + 1}. \qquad (A18)$$

After substituting the numerical values and adopted oxygen abundance $N_O = 5 \times 10^{-4} N_H$ into (A17), the formula for the intensity of the OI 146-μm line becomes

$$I_{146} = 9.23 \times 10^{-24}\alpha_0 N_H L \text{ erg/(cm}^2 \text{ s ster).} \quad (A19)$$

REFERENCES

1. P. Palmer, B. Zuckerman, M. Penfield, *et al.*, Nature **215**, 40 (1967).
2. B. Zuckerman and P. Palmer, Astrophys. J. **153**, L145 (1968).
3. R. W. Russel, G. Melnick, G. F. Gull, and M. Harwit, Astrophys. J. Lett. **240**, L99 (1980).
4. T. B. Kuiper and N. J. Evans, II, Astrophys. J. **219**, 141 (1978).
5. G. T. Stacey, D. T. Jaffe, N. Geis, *et al.*, Astrophys. J. **404**, 219 (1993).
6. A. Natta, C. M. Walmsley, and A. G. G. M. Tielens, Astrophys. J. **428**, 209 (1994).
7. G. T. Smirnov, R. L. Sorochenko, and C. N. Walmsley, Astron. Astrophys. **300**, 923 (1995).
8. V. O. Ponomarev and R. L. Sorochenko, Pis'ma Astron. Zh. **18**, 541 (1992) [Sov. Astron. Lett. **18**, 215 (1992)].
9. S. A. Gulyaev and R. L. Sorochenko, *The Catalogue of the Radio Recombination Lines*, Preprints Nos. 145, 146,

and 168 FIAN (Lebedev Institute of Physics, Academy of Sciences of USSR, 1983).

10. J. M. Launay and E. Roueff, J. Phys. B **10**, 879 (1977).

11. J. M. Launay and E. Roueff, Astron. Astrophys. **56**, 289 (1977).

12. A. G. G. M. Tielens and D. J. Hollenbach, Astrophys. J. **291**, 722 (1985).

13. F. Herrmann, S. C. Madden, T. Nikola, *et al.*, Astrophys. J. **481**, 343 (1997).

14. D. T. Jaffe, S. Zhou, J. E. Howe, and G. J. Stacey, Astrophys. J. **436**, 203 (1994).

15. M. J. Luhman, D. T. Jaffe, A. Sternberg, *et al.*, Astrophys. J. **482**, 298 (1997).

16. J. E. Howe, private communication (1999).

17. D. R. Flower and J. M. Launay, J. Phys. B **10**, 3673 (1977).

18. R. Jaquet, V. Staemmlert, M. D. Smith, and D. R. Flower, J. Phys. B **25**, 285 (1992).

19. R. Emery, P. Aannestad, N. Minchin, *et al.*, Astron. Astrophys. **315**, L285 (1996).

20. R. L. Sorochenko, Astron. Astrophys. Trans. **11**, 199 (1996).

21. N. Panagia, Astrophys. J. **192**, 221 (1974).

22. G. T. Smirnov, R. L. Sorochenko, and V. Pankonin, Astron. Astrophys. **135**, 116 (1984).

23. D. Colley, Mon. Not. R. Astron. Soc. **193**, 495 (1980).

24. I. I. Berulis and R. L. Sorochenko, Astron. Zh. **50**, 270 (1973) [Sov. Astron. **17**, 179 (1973)].

25. D. Crampton and W. A. Fisher, Publ. Dom. Astrophys. Obs. **14** (12) (1973).

26. M. R. Hogerheijde, D. J. Jansen, and E. F. van Dishoeck, Astron. Astrophys. **294**, 792 (1995).

27. F. Wyrowski, P. Schilke, P. Hofner, and C. M. Walmsley, Astrophys. J. Lett. **487**, Ll71 (1997).

28. R. L. Sorochenko, G. Rydbeck, and G. T. Smirnov, Astron. Astrophys. **198**, 233 (1988).

29. J. A. Tauber, A. G. G. M. Tielens, M. Meixner, and P. F. Goldsmith, Astrophys. J. **422**, 136 (1994).

30. R. T. Boreiko and A. L. Betz, Astrophys. J. Lett. **464**, L83 (1996).

31. E. Krügel, C. Thum, J. Martín-Pintado, and V. Pankonin, Astron. Astrophys., Suppl. Ser. **48**, 345 (1982).

32. D. T. Jaffe, S. Zhou, J. E. Howe, *et al.*, Astrophys. J. **436**, 203 (1994).

33. V. Pankonin, *Radio Recombination Lines*, Ed. by P. A. Shaver (Reidel, Dordrecht, 1980) p. 111.

34. H. R. Dickel, W. M. Goss, and G. R. Condon, Astrophys. J. **460**, 716 (1996).

35. J. E. Howe, D. T. Jaffe, R. Genzel, and G. J. Stacey, Astrophys. J. **373**, 158 (1991).

36. D. S. Adler, D. O. S. Wood, and W. M. Goss, Astrophys. J. **471**, 871 (1996).

Translated by G. Rudnitskiĭ

Flux Densities of 235 Pulsars at 102.5 MHz

V. M. Malofeev[1], O. I. Malov[1], and N. V. Shchegoleva[2]

[1]*Pushchino Radio Astronomy Observatory, Astrospace Center of the Lebedev Institute of Physics, Russian Academy of Sciences, Pushchino, Moscow oblast, 142292 Russia*
[2]*Sternberg Astronomical Institute, Moscow State University, Universitetskiĭ pr. 13, Moscow, 119899 Russia*
Received July 21, 1999

Abstract—The flux densities of 235 mostly faint pulsars at 102.5 MHz are presented. The observations were carried out on the very sensitive Large Phased Array of the Lebedev Institute of Physics in 1994–1998. The procedure used for the observations and data processing is described in detail, and estimates of probable errors, including the effect of interstellar scintillations, are given. The mean spectral indices at 102–408 MHz for normal and millisecond pulsars are calculated and compared with information from higher frequency data. There is a deficit of pulsars at distances of less than 3 kpc. © 2000 MAIK "Nauka/Interperiodica".

1. INTRODUCTION

At the present time, more than 1000 radio pulsars have been discovered, including more than 50 millisecond pulsars. Until recently, most detections were made at 400 MHz; however, fairly numerous data at 610 and 1400 MHz have now appeared (mainly for distant objects). Energy or flux density measurements have been carried out primarily at these frequencies (see references in [1]). For example, over the last few years, many flux-density measurements have become available at decimeter and centimeter wavelengths (for 280 pulsars at 408, 606, 925, 1408, and 1606 MHz [2]; 183 pulsars at 1400 MHz, 46 at 4.7 GHz, and 24 at 10.6 GHz [3]; and 87 pulsars at 4.85 GHz [4]).

Using previous surveys and results for several dozen pulsars from 327 MHz to 24 GHz [5–10] (see also references in [11]), these new data enable the construction of spectra for almost 300 objects from 400 to 1400 MHz, for 150 stronger objects up to 5 GHz, and, finally, for several dozen of the strongest pulsars up to 10 GHz [12]. At the same time, there is an evident deficiency of flux measurements at low frequencies. There exist data at 102.5 MHz for only 90 pulsars [13, 14], and data at frequencies near 40, 60, 80–86, and 150–160 MHz for only a few dozen pulsars [13, 15, 16]. There are even fewer data at lower frequencies. In all, about ten pulsars have flux measurements at 17, 20, 25, and 34 MHz [17, 18] (see also references in [11, 15]). To be fair, we should also note that, at very high frequencies as well (30, 47, 87 GHz [19–21]), fluxes have been measured for only a few pulsars.

It is absolutely clear that detailed studies of spectra and their connections with other pulsar parameters require large numbers of flux measurements throughout the radio range. Compiled spectra [12] of the strongest 45 pulsars, for which the most flux measurements are available, have shown that nearly all the spectra can be roughly divided into two classes, with one or two power-law sections; however, there is at least one object (PSR B1822-09 [22]) with a more complex spectrum. In the spectra of most of the 45 strongest pulsars, a low-frequency (50–400 MHz) cutoff is observed [12]. The peak frequency correlates with the rotation period of the pulsar, and there are also correlations of the spectral shape with other basic pulsar parameters [11, 12]. In addition, precise calculation of such important parameters as the luminosity requires knowledge of the emission spectrum [23, 24]. In this connection, the need for extensive flux-density measurements of pulsars at low frequencies is quite evident. There is a similar deficiency of observational data for mean pulsar profiles at frequencies below 400 MHz; precisely these frequencies are now of considerable interest, since many pulsars show sharp changes of the profile width with frequency (see, for example, [13]).

Motivated by the obvious shortage of data on pulsar fluxes and profiles near the peak emission frequencies, we carried out a survey of pulsars at 102.5 MHz. The survey covered faint and not very distant northern-hemisphere objects that had not been observed previously at frequencies below 400 and 600 MHz, including nearby millisecond pulsars. Unfortunately, there are no radio telescopes in the world sufficiently sensitive to carry out similar surveys at frequencies below 102 MHz.

Here, we present the procedure used for the observations and processing of the weak signals, together with flux-density measurements (or estimates) for 235 pulsars. In addition, we analyze the effect of scintillations in the interstellar medium on the scatter of the flux values. We present spectral indices from 102 to 400 MHz and a comparative analysis of these with spectral indices determined at higher frequencies. In forthcoming publications, we will discuss the mean profiles and properties of the radio emission of faint pulsars.

2. OBSERVATIONS

The observations were carried out on the Large Phased Array (LPA) meridian radio telescope of the Lebedev Institute of Physics [25]. It is a highly sensitive instrument with an effective area of

$$3 \times 10^4 \cos|\delta - 55°| \text{ m}^2,$$

where δ is the source declination. Until recently, the fortuitous design of the radio telescope allowed us to observe nearly 24 hours a day, even under conditions of increasing interference (though not over the entire frequency band, only in several 200–300 kHz windows of the entire 3 MHz).

Our observations were carried out from April 1994 to March 1998 in 25 four- to seven-day sessions. The LPA is a phased array with dimensions 384×187 m operating at 102.5 ± 2 MHz. The observation time at the beam half-maximum is $3.5^m/\cos\delta$. To obtain reliable information on the flux and profile of a pulsar, we observed it over several days during several different sessions.

As the receiver backend, we used AS-128 [26] and AS-32 filter-bank spectrum analyzers, which have worked successfully at the Pushchino Radio Astronomy Observatory (PRAO) for many years. As a rule, we used (1) 32, 128, 64, 16, 8 channels with bandwidth 20 kHz (AS-128) or (2) 32, 16, 8 5-kHz channels (AS-32). A narrow-band (channel bandwidth 1.25 kHz), multi-channel (128 channels) UAS-128 spectrum analyzer [27] was designed and created to study pulsars with large dispersion measures, to ensure accurate measurement of their energies and mean profiles. Thus, we could choose an appropriate channel bandwidth and number of channels for the dispersion measure of a particular pulsar. The choice of channel bandwidth is dictated by the fact that, during its propagation through the interstellar medium, the pulsar signal experiences a dispersion in frequency with a time delay

$$\Delta t_\partial(c) = \frac{\Delta\nu \text{DM}}{1.205\nu^3}, \tag{1}$$

where $\Delta\nu$ and ν are the channel bandwidth and frequency in hundreds of MHz and DM is the dispersion measure in pc/cm^3. Using the narrow-band 1.25-kHz channels, we can observe objects with dispersion measures as high as 300 pc/cm^3 with only minor pulse broadening within a channel (up to 3 ms). However, when studying faint pulsars, we used bandwidths of 20 kHz to increase the sensitivity, which restricted the dispersion measure to 60–100 pc/cm^3 if we wished to derive an undistorted mean profile. In addition to the pulse broadening due to dispersion, the pulse shape is strongly distorted at low frequencies by an exponential tail resulting from scattering on inhomogeneities in the interstellar medium. Scattering measurements at 102.5 MHz for

17 pulsars [28] showed that the scattering τ_s depends on the dispersion measure as

$$\tau_s(\text{ms}) = 66\frac{\text{DM}^2}{100}. \tag{2}$$

Therefore, we have carefully searched the shapes of the mean profiles for evidence of scattering for dispersion measures in excess of 50 pc/cm^3. The resulting restriction on the number of channels will be clear from our description of the data-reduction procedure.

The limiting sensitivity of the LPA for observations of pulsars can be estimated:

$$\delta S = \frac{2kT_{\text{sys}}}{A_{\text{eff}}(\Delta\nu_R\Delta tN)^{1/2}}, \tag{3}$$

where k is the Boltzmann constant, T_{sys} is the system temperature, A_{eff} is the antenna's effective area, $\Delta\nu_R$ and Δt are the receiver bandwidth and sampling time interval, and N is the number of periods accumulated. If we substitute mean values of these parameters for the pulsar observations—$T_{\text{sys}} = 1000$ K, $A_{\text{eff}} = 2 \times 10^4$ m^2, $\Delta\nu_R = 5 \times 10^5$ Hz (25 of the 32 20-kHz channels that remained after cleaning), $\Delta t = 0.00256 \times 5 = 0.0128$ s (taking into account running smoothing of every five points with a sampling interval of 2.56 ms) and a mean $N = 400$ for a pulsar with a period of 0.55 s—we find $\delta S = 86$ mJy (1 mJy $= 10^{-29}$ W m^{-2} Hz^{-1}). This high sensitivity enables us to measure a period-averaged flux density as low as 19 mJy for PSR 0353 + 52 with an accumulation of 5412 periods over six days of observation. The problem is that the definition of δS refers to the so-called peak flux density (S_p), which is related to the usual flux density as $S_p = S\dfrac{P}{W_{0.5}}$, where P is the pulsar period and $W_{0.5}$ is the duration of the integrated profile at the half-maximum level in seconds. Thus, if we substitute $N = 5412$ into (3) instead of $N = 400$ and take into account the fact that $P/W_{0.5}$ for PSR 0353 + 52 is 16, we find that we achieve $S_p = 4\ \delta S$ for a mean $S = 6$ mJy. This is close to the limiting sensitivity for the LPA for very narrow pulsar pulses and long integration times.

The measurement complex, which is based on an AT-486 PC [29], enables us to record and accumulate pulses synchronously with the calculated period and starting time. The complex includes a frequency oscillator, commutator, and additional buffer memory. An analog/code converter makes it possible to take readings at intervals down to 0.7 microsecond per channel. Most of our observations were carried out with a time constant of 3 ms and a sampling interval of 2.56 ms. Millisecond pulsars were an exception: for them, as a rule, we chose a time constant of 0.3 ms and a sampling interval of 0.3072 ms.

We performed all the observations using a calibration signal. For this purpose, a step of the noise generator was fed in synchronously with the pulsar period

during the first 15 readings. The generator signal was fed to the front end of the phasing matrix of the LPA, so that the output channel and gain of each of the 128 antenna lines were calibrated. The magnitude of the step was calibrated using pointlike discrete sources with known flux densities. A table with the basic calibration sources is presented below. In this way, we applied a relative method for measuring the pulsar fluxes, which has been successfully used for a long time (see, for example, [11]).

3. DATA PROCESSING

In addition to the standard procedures, the data processing included some additional operations aimed at detecting weak signals appearing at an unknown phase in the pulsar period. The observations yielded a data file containing service information, as well as the signal accumulated with the pulsar period for all the channels used. The standard processing procedure consisted of the following several steps.

(1) Searching for the "zero" level. The zero level was determined outside the pulse, provided the pulse was visible by eye in at least several channels. If the pulsar signal was weak, the zero level was determined over the entire period excluding the first 15 readings, when the calibration step from the noise generator was always present. We used a ~40-ms or 4-ms step during the recordings for millisecond pulsars.

(2) Gain equalization. After subtracting the zero level, we determined the gain factor K in each channel and normalized the signal using the ratio of the calibration signals in the reference and current channels. As a rule, we chose 2–3 channels that were free of interference as reference channels throughout a session.

(3) Elimination of channels with interference. Here, we used two criteria. The first was based on the gain factor K, which should be $3 \geq K > 0$ in channels free of interference. The second criterion used the ratio of the noise dispersions in the current (σ) and reference (σ_0) channels. If this ratio σ/σ_0 exceeded three, such channels were rejected. As a rule, both criteria were suitable simultaneously in the presence of interference, but there were cases where only one criterion operated. The gain factor K proved to be more sensitive, especially, in cases where the interference did not strongly increase the σ of the noise, but appreciably increased the average signal level.

(4) Summation of the signal over channels. After excluding the part with the calibration step, we added the signals in all remaining channels taking into account the dispersion delay between the first (highest frequency) and current channels using relation (1). As a rule, we did not know the phase of the pulse's appearance, and, in order for a large fraction of the channels to participate in the summation, even when the pulse fell in the second half of the period, it was necessary to specify a condition restricting the time delay. As a rule, the delay should not exceed 0.3 of the period. This results in a clear restriction on the number of channels used in the observations. Using (1), we find that the optimum number of channels is

$$n \leq \frac{0.36 P \nu^3}{\mathrm{DM} \Delta \nu} + 1, \qquad (4)$$

where P is the period of the pulsar rotation in seconds.

Figure 1 presents an example demonstrating the effectiveness of the signal processing procedure in the presence of interference. The upper graph shows the sum of 32 channels and the lower graph the sum of 23 of these channels, taking into account the gain factor and with nine channels excluded.

(5) We smoothed the new zero line over two intervals of the noise signal outside the pulse, which, as a rule, were located at opposite ends of the period. We then found the boundaries of the accumulated pulse and calculated the energy. In the general case, this is

$$E = \frac{D K_\mathrm{a} \Delta t}{K_\mathrm{e} N I_0} \sum_{t_1}^{t_2} I(t), \qquad (5)$$

where D is a calibration factor, equal to the step amplitude in Janskys; K_e and K_a are correction factors taking into account the complex shape of the LPA beam in elevation and azimuth (see the detailed calculation in [30]); Δt is the sampling interval in milliseconds; I_0 and $I(t)$ are the amplitudes of the calibration step and pulse signal in units of the analog/code converter; and t_1 and t_2 are the boundaries of the summed pulse. The period-averaged flux density, which is becoming increasingly popular in catalogs (see, for example, [1]), is $S = E/P$. The factor D was calculated as the mean for each observing session, using several calibration sources with small angular sizes and, whenever possible, uniformly distributed in right ascension in order to trace changes of D during the session. The main reference radio sources from the 3C catalog and their flux densities are listed in Table 1. We calculated the flux densities based on the survey [31] carried out at the PRAO at the nearby frequency of 86 MHz. In addition to the sources listed in Table 1, we used about ten secondary sources to monitor the stability of D.

In single observations of faint pulsars, the signal did not always exceed the 4σ level. In this case, for reliable detection of the integrated pulse, we used several types of summation: (a) over several days within one session, (b) over several sessions, (c) over groups of channels, and (d) with a period multiple of several pulsar periods. The first two procedures proved to be feasible, since the daily time for the start of pulse accumulation was calculated using the program of Shabanova [32] with conservation of the pulse arrival phase with respect to a particular date and the PRAO time service [33]. We also summed over two groups of channels (for example, 1–16 and 17–32), which enabled us to see the shift of the pulse arrival phase in the two sums and, thereby, distinguish a faint pulsar signal from pulsed interfer-
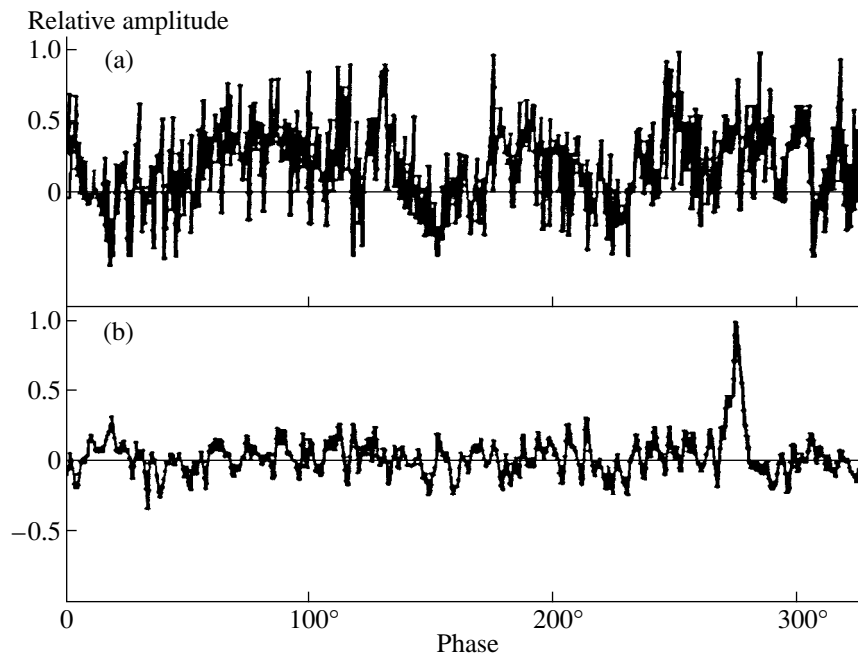
Relative amplitude

Fig. 1. An example of the mean profile of PSR 1112 + 50, obtained on May 19, 1997, averaged over 205 periods: (a) sum of 32 channels with 20-kHz bandwidth, (b) sum of the 23 channels that remained after cleaning.

ence, which does not change the arrival phase. In addition to the different summations, we also made use of additional information on the mean-pulse shape at 400 MHz or higher frequencies to ensure reliable pulse detection [3–5]. Another criterion was the presence of two pulses in signals accumulated with the double period. We frequently used this mode, especially for short-period pulsars; in observations of millisecond pulsars, the signal was integrated with a period equal to 4–20 pulsar periods. It was necessary not only to check for the presence of a pulse, but also to insert a 4-ms calibration step into the recording.

4. FLUX-MEASUREMENT ERRORS

In our case, the error in our measurement of the energy has the following origins.

(1) Errors in the data processing: fitting the zero line, evaluation of the mean-pulse area, and calibration. These errors strongly depend on the signal-to-noise ratio. According to our estimates [30], they do not exceed 20–30%.

(2) The error in measuring the total energy using a linearly polarized antenna such as the LPA. This error is discussed in detail in [30], where it is shown that it strongly depends on the rotation measure and degree of linear polarization at 102.5 MHz. For the most frequently used bandwidth of 640 kHz (32 20-kHz channels) and a mean linear polarization of 30% [32], this error varies from 1 to 30%. It grows slowly with decreasing receiver bandwidth.

(3) The error due to refractive (long-period) scintillations and, especially, to diffractive (short-period) scintillations of the pulsar signal on irregularities in the interstellar medium. At 102 MHz, diffractive scintillations are saturated [35] and reach 100% of the mean flux. The effect of these scintillations can be reduced by averaging the signal in time and frequency using the broad bandwidth of the receiver. To estimate the effect of scintillations quantitatively, we used empirical dependences of the decorrelation bandwidth (Δv_m), time correlation radius (t_m), and scintillation index (m) on frequency and dispersion measure. We employed the relations obtained in [36, 37], our own data, and also numerous published data on the scintillation parameters of some several dozen pulsars. To estimate the critical frequency, which

Table 1. Flux densities of calibration sources at 102.5 MHz

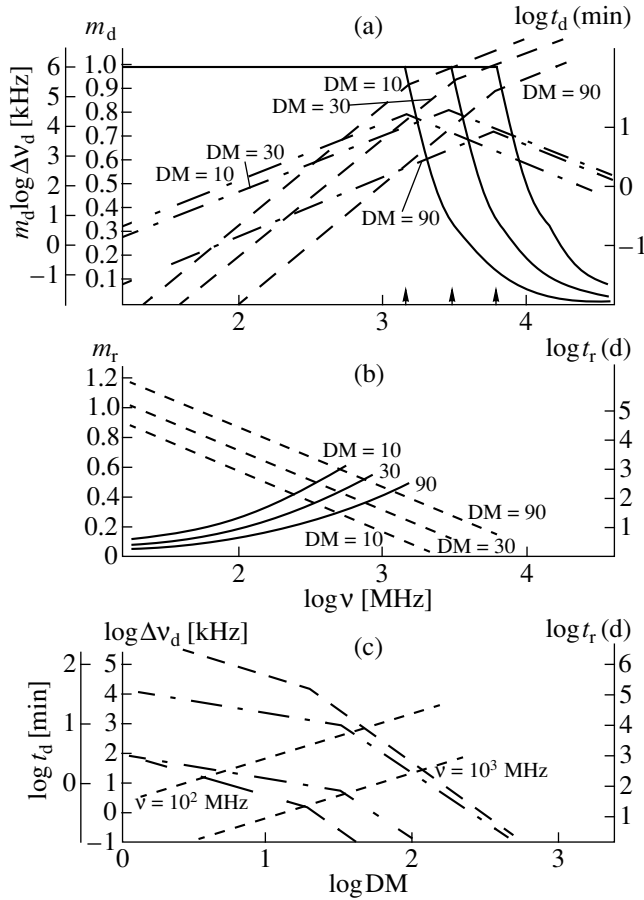| Calibration source	Flux density at 102.5 MHz, Jy
3C75	41
3C119	20
3C137	19
3C142.1	37
3C186	40
3C244.1	34
3C267	24
3C270	74
3C289	19
3C441	22

Fig. 2. Empirical dependences of the parameters of (a) diffractive scintillations and (b) refractive scintillations on frequency and (c) on dispersion measure. The solid line corresponds to m, the long dashed curve to $\Delta\nu_d$, the dot-dash curve to t_d, and the short dashed curve to t_r.

marks the transition from weak to strong scintillation, we used the relation $\nu_{cr} = DM \times 0.1$ GHz [37]. Figure 2 shows the frequency dependences for diffractive (subscript d, Fig. 2a) and refractive (subscript r, Fig. 2b) scintillations as well as the dependence of scintillation parameters on dispersion measure or distance (Fig. 2c). The total relative error in the flux measurement can be written

$$\Delta S = \left(\Delta S_p^2 + (\Delta S_{t_r} m_r)^2 + (\Delta S_{t_d} m_d m(J))^2\right)^{1/2}. \quad (6)$$

Here, ΔS_p is the relative error due to the linearly polarized antenna; $\Delta S_t \approx 1/(t/3\, t_m)^{1/2}$ is the error due to temporal fluctuations with time correlation radius t_m and duration of the observations t [30]; $m = (\langle (S - \bar{S})^2 \rangle / \bar{S}^2)^{1/2}$, $m(J) = m/m_0 = ((2/J) \arctan J - (1/J^2)\ln(1 + J^2))^{1/2}$; and $J = \Delta\nu_R/\Delta\nu_d$ is the ratio of the scintillation indices for signal reception over a rectangular bandwidth (m) and an infinitely narrow bandwidth (m_0), as derived by Sutton and given in [30]. The value $m(J) = 0.2$ requires that $J = 70$; this is achieved with a total receiver bandwidth

$\Delta\nu_R = 640$ kHz for pulsars with DM ≥ 10 (Fig. 2c). Thus, the signal fluctuations due to diffractive scintillations are very efficiently suppressed by the use of broad receiver bandwidths. At meter wavelengths, the largest contribution to ΔS comes from m_d and ΔS_{t_d} (Fig. 2a), and from ΔS_{t_r} for distant pulsars (Fig. 2c); however, due to the smallness of the other factors, ΔS does not exceed 40% for most pulsars. To decrease ΔS_{t_d} and ΔS_{t_r}, we average all observations obtained over five years.

(4) An error that strongly increases for distant pulsars is that due to scattering of the signal on inhomogeneities in the interstellar medium, which leads to the appearance of an exponential tail in the pulse; for some dispersion measures, this tail can occupy the entire period of the pulsar. It is shown in [30] that, beginning from $\tau_r/P = 0.2$, the added energy is 17% [the parameter τ_r can be estimated from (2)]. For a pulsar with a period of 0.5 s, the value $\tau_r/P = 0.2$ is already reached for pulsars with DM = 123 pc/cm³. This error is especially important for millisecond pulsars: it restricts possibilities for observing such pulsars with dispersion measures greater than 20 pc/cm³ at our frequency.

Thus, to decrease the effect of scintillations, it is desirable to use broader receiver bands. However, this opposes the desire to obtain an undistorted mean pulse shape, since it increases the value of Δt_∂ (1). Therefore, we often used broad bands to measure the energy but narrower bands to study the profiles of distant pulsars, already knowing the phase of arrival of the mean pulse. Without calculating the error for any individual pulsar, we can estimate the total error, including the effect of scintillations, from the scatter of the daily flux-density measurements. However, all of this is true only if the pulsars have no intrinsic flux variations and if there is no interference. We plan to carry out a dedicated detailed analysis to separate fluctuations associated with scintillations and with the radiation mechanism, especially for strong and distant objects.

5. RESULTS OF THE MEASUREMENTS

Table 2 lists our results for 235 pulsars at 102.5 MHz. The columns give the pulsar name from the catalog of Taylor *et al.* [1], the mean flux density in mJy S, the rms scatter of the flux density in mJy δS, the number of summed pulsar periods in thousands N, the number of observation days M, and the spectral index from 102 to 408 MHz α. The data at 408 MHz were taken mainly from the long-term measurements of [2].

These fluxes can be used to construct the spectra and estimate spectral indices, luminosities, etc. They have already been used to extend our catalog of pulsar spectra [38] and for various statistical studies [39]. Figure 3 presents the spectra of several pulsars, to show the mea-
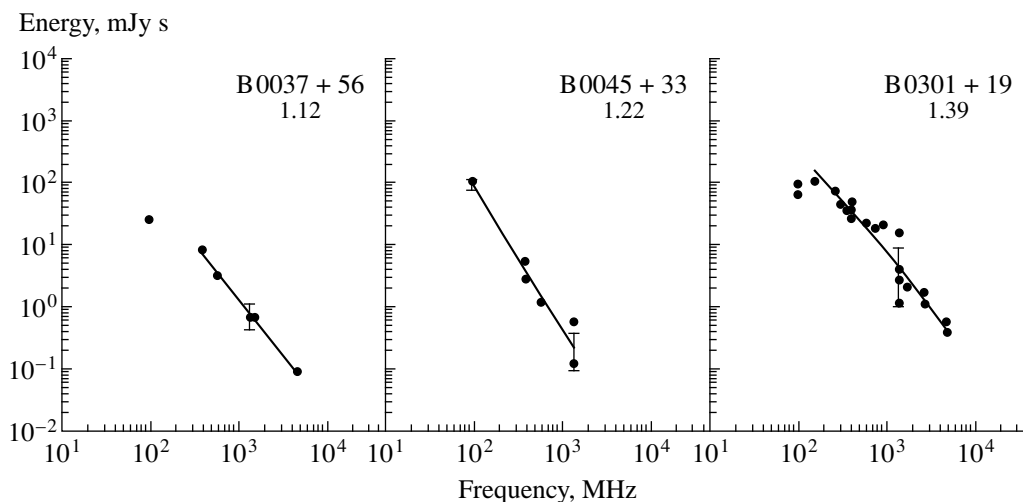
Fig. 3. Examples of pulsar spectra with fitted power-law functions. The errors at 100 and 1400 MHz show estimates of the effect of scintillations on the accuracy of the energy measurements. The pulsar name and period of rotation (in seconds) are given in the upper right corner.

sured flux density (energy) at the extreme frequency of 102.5 MHz.

We constructed a histogram of the 102.5-MHz flux densities of the pulsars (Fig. 4). The measured flux densities cover a wide range from 16 mJy (PSR 0643 + 80) to 10^4 mJy (PSR 0531 + 21, the Crab pulsar), with most between 30 and 300 mJy. While the right-hand part of the distribution reflects the decrease of the flux with growing distance to the pulsars, the reason for the small number of pulsars with weak fluxes is not clear. In this histogram and our subsequent analysis, we have added 53 pulsars from earlier measurements [13, 14], not overlapping with the list of pulsars for the present study. It is interesting that the flux distribution for the 21 millisecond pulsars (dashed distribution in Fig. 4) is shifted somewhat toward greater fluxes.

To understand the deficit of faint pulsars, we have constructed a distribution of the number of pulsars as a function of distance R (Fig. 5). The deficit corresponds to the small number of pulsars within 3 kpc; if we use the number of pulsars at distances of 3–5 kpc with a mean of 4 kpc as a reference (N_4), the number of survey pulsars at greater distances is fairly well approximated by the dependence $N_4 R^{-2}$ (kpc), shown in Fig. 5 by the dashed line. The absence of the 160 nearby pulsars predicted by this dependence could be connected either with undetected low-luminosity pulsars or with a "cutoff" in the integrated luminosity function at luminosities below 10^{28} erg/s [24], and a lack of pulsars with luminosities lower than 10^{26} erg/s. The undetected pulsars must mostly have steep spectra to explain their absence after numerous searches at 400, 600, and 1400 MHz; i.e., these objects would be similar to the Geminga radio pulsar [40].

The distribution of 102–400-MHz spectral indices is close to normal (Fig. 6) and yields a mean value over 175 pulsars $\bar{\alpha} = 1.47$ with $\sigma = 0.76$ (without millisec-

ond pulsars, including PSR 0531 + 21 and 1310 + 18). For the remaining pulsars, there is either only an estimate of the 102-MHz flux or no flux measurement at 408 MHz. This spectral index is considerably greater that we obtained earlier for 88 stronger objects ($\bar{\alpha} = 0.91$ with $\sigma = 0.76$) [14]. About half these pulsars were included in the new survey, and the increase in the mean spectral index is primarily due to the steep spectra of new, mostly faint pulsars. A comparison with other studies of the spectra of 343 objects at 400–1600-MHz ($\bar{\alpha} = 1.6$) [2] and of 141 pulsars at 1400–4850 MHz ($\bar{\alpha} = 1.9$) [4] shows that the mean spectral index decreases at meter wavelengths and increases at centimeter wavelengths. We noted this tendency as early as 1979 [40], and, after studies of the spectra of dozens of pulsars over a broad wavelength
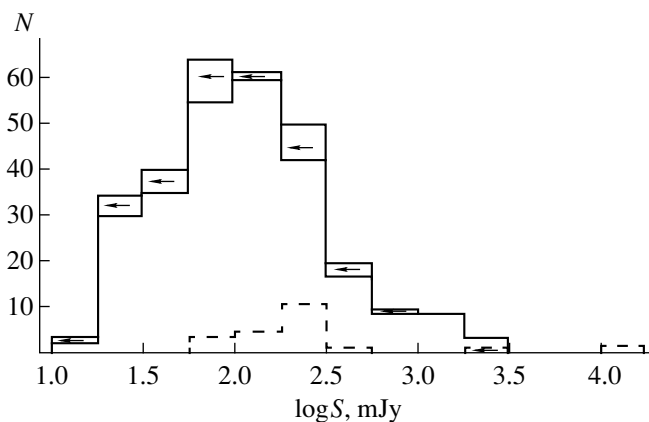

Fig. 4. Flux density distributions for the survey normal pulsars (solid) and millisecond pulsars with periods shorter than 35 ms (dashed). The arrows show pulsars with upper limits for their flux densities.

Table 2. Flux densities of pulsars at 102.5 MHz

PSR	S, Jy	δ_S, Jy	N, 10^3	M	α	PSR	S, Jy	δ_S, Jy	N, 10^3	M	α
J 0006 + 18	<40		18.0	9	<3.9	J 0927 + 23	30	13	5.2	17	
0031–07	560	310	1.6	8	1.7	0942–13	100	30	2.0	8	1.0
0037 + 56	24	15	3.8	12	0.9	0943 + 10	200	200	1.1	7	2.9
0045 + 33	88	21	1.5	8	2.7	J 0943 + 22	77	60	7.9	18	1.9
0052 + 51	23	12	3.1	19	1.4	0950 + 08	2030	2650	59.4	69	1.2
0053 + 47	80	26	6.1	9	2.4	J 1012 + 5307	MP 100	40	620.1	19	0.9
0059 + 65	77	42	0.4	4	1.6		IP 85	45	360.2	11	
0105 + 65	84	23	0.8	2	1.6	1016–16	220	120	0.6	5	2.8
0105 + 68	23	12	12.4	22	1.3	J 1022 + 10	100	40	165.0	19	1.1
0114 + 58	70	20	29.2	11	1.6	J 1025-0709	300	120	126.5	8	2.5
0136 + 57	181	85	19.5	13	1.4	1039–19	<50		0.8	5	<2.1
0144 + 59	MP 25	15	39.5	23		1112 + 50	60	14	9.8	48	1.2
	IP 13	8	26.0	13		1133 + 16	1280	550	4.7	25	1.2
0148–06	109	55	1.2	8	0.8	1237 + 25	260	130	1.7	10	0.6
0153 + 39	<39		0.6	4	<1. 7	J 1238 + 21	60	22	3.3	16	
0154 + 61	52	20	2.0	10	1.5	J 1246 + 22	30	20	10.9	22	0.0
0226 + 70	17	8	10.0	25	1.4	1254–10	110	60	6.7	19	1.6
0301 + 19	48	26	2.3	14	0.4	1257 + 12	220	100	390.0	27	1.8
0320 + 39	230	70	1.2	16	1.4	1309–12	60	35	2.0	8	2.0
0329 + 54	517	223	1.8	6	−0.8	1310 + 18	80	30	68.5	20	3.2
0331 + 45	34	11	18.1	17	1.3	1322 + 83	36	12	30.6	11	0.9
0339 + 53	50	26	2.8	15	1.9	1508 + 55	1280	500	3.6	7	1.8
0353 + 52	19	8	21.1	16	0.3	1516 + 02a	(180)	(50)	136	7	3.9
0402 + 61	55	18	11.5	15	0.9	1540–06	130	30	4.4	15	0.9
0410 + 69	28	23	24.0	15	1.1	J 1518 + 4904	68	20	76	19	
J 0417 + 35	46	15	6.0	15	2.6	1530 + 27	94	44	2.6	12	1.4
J 0421–03	58	43	2.8	14	2.0	1534 + 12	MP 90	35	102.0	18	0.7
J 0435 + 27	67	28	15.7	21			IP80	30	70.0	12	
0447–12	64	23	6.1	12	1.3	1541 + 09	400		2.0	7	1.2
0450 + 55	150	60	26.9	24	0.7	J 1549 + 2110	66	46	2.4	13	
0458 + 46	40	20	12.8	26	1.0	1604–00	220	100	4.0	8	1.0
J 0459–02	130	50	2.5	13	1.8	1607–13	160	80	3.2	20	1.7
0523 + 11	119	25	3.7	6	1.3	1612 + 07	100	40	0.5	3	1.7
0525 + 21	100	50	0.3	5	0.4	1620–09	40	25	3.4	20	1.4
0531 + 21	10^4	6×10^3	24.0	5	2.0	J 1627 + 1419	50	26	9.0	20	
J 0533 + 04	42	21	4.9	22		1633 + 24	50	15	5.4	15	1.3
J 0538 + 2817	320	150	14.5	10	1.7	J 1640 + 2224	250	130	258.5	7	
0540 + 23	44	16	13.1	16	0.3	1639 + 36a	180	100	116.9	9	3.0
0559–05	100	38	10.4	19	1.1	1642–03	300	170	3.2	6	− 0.2
0609 + 37	60	20	17.7	24	1.0	J 1645 + 1012	90	60	2.4	9	
J 0613-0200	(210)	160	26.5	1	1.7	1648–17	<260		1.4	12	−2.5
0611 + 22	280	100	8.8	14	1.7	J 1649 + 2533	60	30	1.6	7	
J 0621 + 1002	(420)	240	76.0	2		J 1652 + 2651	40	20	2.9	11	
0621–04	100	60	6.7	32	2.2	1657–13	90	50	2.9	11	1.9
0626 + 24	130	80	6.9	16	1.0	1700–18	190	100	0.6	7	2.1
J 0631 + 1036	180	20	2.3	3	3.5	1702–19	150	50	3.8	5	1.2
0643 + 80	16	7	26.9	24	0.7	1709–15	200	120	1.1	6	2.6
0656 + 14	55	29	10.5	19	1.6	J 1713 + 0747	280	75	360.1	14	1.5
0727–18	<250		2.2	5	<1.3	1717–16	<190		2.1	15	<2.0
J 0751 + 1807	290	90	612.0	15	2.5	1718–02	80	40	3.6	8	0.9
0751 + 32	49	20	1.7	11	1.3	J 1720 + 2150	<60		1.9	8	
0756–15	60	44	5.5	17	1.5	1726–00	80	40	5.6	10	1.5
0809 + 74	1080	900	1.8	3	1.9	1730–22	<290		0.8	3	<1.8
0820 + 02	100	46	4.7	19	0.9	1732–07	100	36	4.9	13	1.3
0823 + 26	620	130	14.6	32	1.6	1732–02	80	60	2.8	11	1.9
0834 + 06	1040	320	1.8	11	1.8	J 1736 + 05	70	24	2.0	9	
0841 + 80	28	17	18.8	21	2.1	1737 + 13	80	12	1.1	4	0.9
0906–17	320	150	6.2	11	2.2	1738–08	140	83	0.9	8	1.2
0917 + 63	30	11	4.7	15	1.3	1740–13	370	200	3.3	12	3.0
0919 + 06	128	63	4.5	9	0.6	1740–03	90	40	6.8	18	2.5

Table 2. (Contd.)

| PSR	S, Jy	δ_S, Jy	N, 10³	M	α	PSR	S, Jy	δ_S, Jy	N, 10³	M	α
J 1741 + 2758	30	10	0.7	5		1935 + 25	<100		3.5	6	
1745–12	230	180	5.1	9	1.7	1937 + 21	>2200	1100	37.0	4	>1.6
J 1752 + 2359	40	20	5.8	10		1942–00	90	50	2.0	10	2.0
1753 + 52	30	12	1.5	21	1.3	1943 + 18	<60		2.4	11	
1758–03	100	55	2.4	11	1.3	J 1946 + 2611	115	60	3.9	8	3.2
J 1758 + 30	60	40	4.0	15	2.5	1946 + 35	60	40	3.7	10	–0.6
1802 + 03	110	30	8.9	9	2.3	1951 + 32	220	170	117.0	18	2.5
1804–08	550	340	12	14	1.6	1953 + 50	170	50	5.5	17	1.4
J 1808 + 00	<190		1.3	5	<3.3	2000 + 32	80	30	2.2	6	2.0
J 1808–0813	120	50	2.5	10	1.1	2000 + 40	170	80	0.5	3	0.9
1810 + 02	35	18	2.4	11	1.6	2002 + 31	<35		1.1	9	
J 1811 + 0702	160	50	6.6	14	1.9	2003–08	190	50	2.6	7	1.6
1822 + 00	60	30	4.5	15	1.5	J 2008 + 2513	60	30	6.5	16	2.3
J 1822 + 0705	60	20	1.9	12		2011 + 38	95	40	6.0	20	0.9
1823–11	<150		1.2	11	<2.5	2016 + 28	260	100	4.3	11	–0.1
J 1823–0154	300	170	2.6	9	2.3	J 2019 + 2425	170	80	332.6	11	1.8
1829–08	<80		2.4	7	<1.6	2020 + 28	340	140	3.2	8	1.1
1831–03	770	400	2.2	7	1.6	2021 + 51	60	25	5.0	11	–0.2
1831–00	<540		0.8	2	<3.4	2022 + 50	30	20	3.5	8	1.1
1834–06	90	60	1.5	13	1.3	2025 + 21	30	10	3.5	6	1.7
J 1834 + 10	80	50	1.3	7		2028 + 22	22	10	1.8	5	1.1
1839–04	610	340	0.9	8	2.6	J 2033 + 17	200	60	196.0	8	
1839 + 56	50	20	0.5	2	0.6	2035 + 36	34	10	3.5	8	1.3
1841–04	<190		0.3	5	<2.3	2036 + 53	30	17	3.0	12	1.7
1844–04	100	60	3.6	10	0.2	2043–04	45	20	0.5	6	0.6
1845–01	950	550	2.0	6	1.8	J 2043 + 2740	190	80	8.4	10	
1846–06	90	60	0.3	6	0.9	2044 + 46	<110		3.1	14	
1848 + 04	280	180	9.1	12	2.3	2045 + 56	34	11	4.2	5	1.5
1848 + 12	70	30	1.9	11	1.6	2053 + 36	80	20	9.7	16	0.8
1848 + 13	65	10	1.6	5	1.7	2110 + 27	130	30	4.4	31	1.4
1853 + 01	<220		4.8	6	<3.0	2111 + 46	430	110	3.1	10	0.5
1854 + 00	170	90	6.8	16	2.6	2122 + 13	55	25	5.8	18	1.9
1855 + 02	340	140	1.6	6	2.2	2127 + 11a	40	23	21.0	17	3.6
1855 + 09	370	120	45.0	3	1.8	J 2139 + 2242	30	10	1.7	8	
1859 + 03	1460	920	1.0	3	1.6	J 2145–0750	90	50	29.0	3	0.4
1900–06	140	90	3.5	7	1.3	2148 + 52	40	24	7.5	14	0.7
1900 + 05	100	30	2.3	8	1.4	2148 + 63	20	8	5.1	11	=0.3
1902–01	280	170	3.3	10	2.5	2154 + 40	200	70	0.9	5	0.5
1903 + 07	<180		1.7	5		J 2156 + 2618	<40		1.4	3	
J 1904 + 0004	<60		12.4	8		J 2205 + 1444	60	20	2.1	9	2.7
1907–03	220	160	3.8	9	1.5	2210 + 29	50	20	3.0	12	1.5
1907 + 02	110	50	1.3	6	1.2	J 2215 + 1538	30	16	4.5	15	1.5
1907 + 10	250	120	7.9	12	1.2	2217 + 47	1200	400	0.6	2	1.7
1907 + 12	100	50	0.9	6	2.2	2227 + 61	60	10	9.1	9	0.9
1911 + 13	55	25	1.7	4	1.7	J 2229 + 2643	270	200	40.1	1	2.2
1913 + 10	220	50	1.4	4	1.7	J 2234 + 2114	35	13	1.2	7	1.9
1914 + 09	230	85	1.6	4	1.8	J 2235 + 1506	90	40	38.1	6	2.5
1914 + 13	530	390	3.9	5	2.7	2241 + 69	30	20	2.8	9	1.8
1915 + 13	140	100	2.2	2	0.9	J 2248–0101	120	50	5.0	11	1.7
1918 + 26	30	11	3.1	10	1.2	J 2253 + 1516	45	20	2.5	9	2.1
1919 + 14	210	110	2.5	7	3.1	2303 + 46	20	10	3.6	12	–0.1
1919 + 21	1900	600	0.7	4	2.7	J 2307 + 2225	30	13	4.4	10	2.0
1920 + 20	<130		1.8	9		2310 + 42	110	90	7.3	9	0.2
1923 + 04	50	30	0.8	4	0.6	2315 + 21	100	30	0.3	2	1.4
1924 + 14	160	80	1.0	7	2.1	J 2317 + 1439	120	50	160.0	4	1.3
1924 + 16	140	90	3.9	10	2.1	2324 + 60	120	40	7.2	5	1.4
1929 + 10	950	660	5.4	9	0.6	2334 + 61	75	30	14.0	16	1.5
1929 + 20	550	300	6.0	7	2.2	J 2347–0612	70	40	2.9	16	1.4
1930 + 22	90	20	9.6	6	1.8	2351 + 61	30	10	2.9	8	0.4
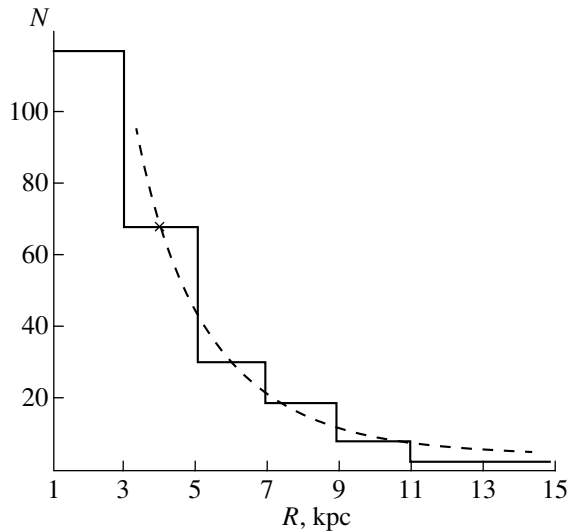
Fig. 5. Distribution of number of pulsars with distance. The dashed line shows the dependence $N_4 R^{-2}$.
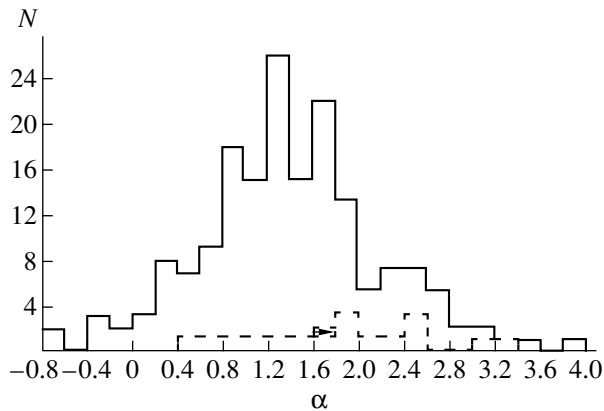

Fig. 6. Distribution of 102–408-MHz spectral indices for normal pulsars (solid) and millisecond pulsars (dashed).

range [11, 12], it became clear that it reflects two properties of the pulsar spectra: a low-frequency cutoff and a high-frequency turnover in class B pulsars. It follows that very few of the faint pulsars observed at 102 MHz for the first time have cutoffs above this frequency.

A comparison of the spectral indices of "normal" and millisecond pulsars (Fig. 6) shows that a very broad distribution of spectral indices is observed for the millisecond pulsars, in spite of their small number (19), with a somewhat higher value $\bar{\alpha} = 1.9$ and with $\sigma = 0.9$. The same mean spectral index was measured at higher frequencies, from 0.4 to 1.7 (4.7) GHz for 32 northern-hemisphere objects ($\bar{\alpha} = 1.8 \pm 0.1$ [42]) and for 19 southern pulsars at the same frequencies ($\bar{\alpha} = 1.9 \pm 0.1$ [43]). Thus, we conclude that, while the "normal" pulsars of our sample include many objects with low-frequency

cutoffs, the relative number of such objects among the millisecond pulsars is much smaller.

REFERENCES

1. J. H. Taylor, R. N. Manchester, and A. G. Lyne, Astron. J., Suppl. Ser. **88**, 529 (1993).
2. D. R. Lorimer, J. A. Yates, A. G. Lyne, and D. M. Gould, Mon. Not. R. Astron. Soc. **273**, 411 (1995).
3. J. H. Seiradakis, J. A. Gil, D. A. Graham, *et al.*, Astron. Astrophys., Suppl. Ser. **111**, 205 (1995).
4. J. Kijak, M. Kramer, R. Wielebinski, and A. Jassner, Astron. Astrophys., Suppl. Ser. **127**, 153 (1998).
5. D. Morris, D. A. Graham, W. Sieber, *et al.*, Astron. Astrophys., Suppl. Ser. **46**, 421 (1981).
6. M. Vivekanand, D. K. Mohanty, and C. F. Salter, Mon. Not. R. Astron. Soc. **204**, 81 (1983).
7. A. D. Kuz'min, V. M. Malofeev, V. A. Izvekova, *et al.*, Astron. Astrophys. **161**, 183 (1986).
8. W. Sieber and R. Wielebinski, Astron. Astrophys. **177**, 342 (1987).
9. D. R. Stinebring and J. J. Condon, Astrophys. J. **352**, 207 (1990).
10. S. Johnston, A. G. Lyne, R. N. Manchester, *et al.*, Mon. Not. R. Astron. Soc. **255**, 401 (1992).
11. V. M. Malofeev and I. F. Malov, Astron. Zh. **57**, 90 (1980) [Sov. Astron. **24**, 54 (1980)].
12. V. M. Malofeev, J. A. Gil, A. Jessner, *et al.*, Astron. Astrophys. **285**, 201 (1994).
13. V. A. Izvekova, A. D. Kuz'min, V. M. Malofeev, and Yu. P. Shitov, Astrophys. Space Sci. **78**, 45 (1981).
14. V. M. Malofeev, Pis'ma Astron. Zh. **19**, 366 (1993) [Astron. Lett. **19**, 138 (1993)].
15. W. Sieber, Astron. Astrophys. **28**, 237 (1973).
16. O. B. Slee, S. K. Alurkar, and A. D. Bobra, Aust. J. Phys. **39**, 103 (1986).
17. Yu. M. Bruk, D. G. Devis, A. D. Kuz'min, *et al.*, Astron. Zh. **55**, 1031 (1978) [Sov. Astron. **22**, 588 (1978)].
18. A. A. Deshpande and V. Radhakrishnan, J. Astrophys. Astron. **13**, 151 (1992).

19. R. Wielebinski, A. Jessner, M. Kramer, *et al.*, Astron. Astrophys. **272**, L13 (1993).

20. M. Kramer, K. M. Xilouris, A. Jessner, *et al.*, Astron. Astrophys. **306**, 867 (1996).

21. D. Morris, K. Kramer, C. Thum, *et al.*, Astron. Astrophys. **322**, L17 (1997).

22. J. A. Gil, A. Jessner, J. Kijak, *et al.*, Astron. Astrophys. **282**, 45 (1994).

23. I. F. Malov, V. M. Malofeev, and D. S. Sen'e, Astron. Zh. **71**, 762 (1994) [Astron. Rep. **38**, 677 (1994)].

24. I. F. Malov, O. I. Malov, and V. M. Malofeev, Astron. Astrophys. Trans. **10**, 205 (1996).

25. V. V. Vitkevich, A. A. Glushaev, Yu. P. Ilyasov, *et al.*, Izv. Vyssh. Uchebn. Zaved. Radiofiz. **19**, 1594 (1976).

26. M. V. Bobkov, G. I. Dobysh, and V. V. Kokarev, in *Abstracts of the All-Union Conference on Apparatus, Antennas, and Methods* [in Russian] (Akad. Nauk Arm. SSR, Yerevan, 1978), p. 57.

27. V. M. Malofeev, A. G. Soin, and I. G. Mazurin, Preprint FIAN (Lebedev Institute of Physics Russian Academy of Scince, 1996), p. 45.

28. A. D. Kuz'min, V. A. Izvekova, V. M. Malofeev, and Yu. P. Shitov, Pis'ma Astron. Zh. **14**, 140 (1988) [Sov. Astron. Lett. **14**, 58 (1988)].

29. I. M. Dagkesamanskaya, K. A. Lapaev, and S. V. Logvinenko, in *Abstracts of the XXV Radio Astronomy Conference* [in Russian] (Pushchino, 1993), p. 234.

30. V. M. Malofeev, Tr. Fiz. Inst. Akad. Nauk SSSR **199**, 125 (1989).

31. V. S. Artyukh, V. V. Vitkevich, R. D. Dagkesamanskiĭ, *et al.*, Astron. Zh. **45**, 712 (1968) [Sov. Astron. **12**, 567 (1968)].

32. T. V. Shabanova, Astron. Astrophys. **453**, 779 (1995).

33. A. S. Vdovin, Yu. P. Ilyasov, and Yu. A. Fedorov, *Studies in the Measurement of Time and Frequency. Collection of Scientific Works* [in Russian] (Gosstandart, Moscow, 1989), p. 46.

34. S. A. Suleĭmanova, D. V. Volodin, and Yu. P. Shitov, Astron. Zh. **65**, 349 (1988) [Sov. Astron. **32**, 177 (1988)].

35. V. I. Shishov, Izv. Vyssh. Uchebn. Zaved. Radiofiz. **33**, 443 (1990).

36. V. I. Shishov, V. M. Malofeev, A. V. Pynzar', and T. V. Smirnova, Astron. Zh. **72**, 485 (1995) [Astron. Rep. **39**, 428 (1995)].

37. V. M. Malofeev, V. I. Shishov, W. Sieber, *et al.*, Astron. Astrophys. **308**, 180 (1996).

38. V. M. Malofeev, Astron. Astrophys. (1999) (in press).

39. V. M. Malofeev, *Pulsars: Problems and Progress*, ASP Conf. Ser. **105**, 271 (1996).

40. V. M. Malofeev and O. I. Malov, Nature **389**, 697 (1997).

41. V. A. Izvekova, A. D. Kuz'min, V. M. Malofeev, and Yu. P. Shitov, Astron. Zh. **56**, 322 (1979) [Sov. Astron. **23**, 179 (1979)].

42. M. Kramer, K. Xilouris, D. Lorimer, *et al.*, Astrophys. J. **501**, 270 (1998).

43. M. Toskano, M. Bailes, R. Manchester, *et al.*, Astrophys. J. **506**, 863 (1998).

Translated by G. Rudnitskiĭ

Light-Curve Synthesis for Close Binaries: Elliptical Disk around a White Dwarf

T. S. Khruzina

Sternberg Astronomical Institute, Universitetskiĭ pr. 13, Moscow, 119899 Russia
Received June 15, 1999

Abstract—We present an algorithm for the synthesis of the light curve of a close binary system consisting of a red dwarf that fills its Roche lobe and a spherical white dwarf. The spherical component is surrounded by an elliptical accretion disk with a complex shape, geometrically thin near the spherical star and geometrically thick at the edge of the disk. The model is able to describe the shape of the secondary minimum in the light curve of the eclipsing variable KU Cyg, which has not been possible using other models.

1. INTRODUCTION

There has recently been a plethora of studies investigating matter flows and accretion disks in close binary systems (see, for example, [1–4]). Some interesting results have been obtained for SU UMa stars, which form a subclass of dwarf novae. They are characterized by the "superhump" phenomenon; i.e., in addition to frequent but short outbursts lasting two to three days, similar to the normal outbursts in ordinary dwarf novae, these stars display less frequent but more regular very intense, prolonged (10–14 day) outbursts called "superoutbursts." No outbursts of intermediate duration have been observed. During superoutbursts, periodic enhancements of the emission level by up to $0\overset{m}{.}2$–$0\overset{m}{.}3$ ("superhumps") are observed in the light curve. The period of these superhumps is very close to the orbital period, but always exceeds it by several (usually 3–7) percent. No such superhumps have been detected in other subclasses of dwarf novae.

Numerous models have been suggested to explain the superhump phenomenon. Currently, the model initially proposed by Vogt [5] and later developed in [1, 6, 7] is generally accepted. As shown by computer simulations of mass transfer in binary systems [1, 7], in systems with a low-mass donor star (secondary), the accretion disk around the white dwarf (primary) is tidally unstable and its shape is close to oval. The reason for the tidal instability in the accretion disks in close binary systems with small mass ratios ($Q = M_2/M_1 < 0.25$) is a parametrical resonance of the orbital rotation period for a test particle in the disk and the rotation period of the secondary when the period ratio is 3 : 1. A general scenario for the tidal instability was suggested in [8], including both thermal and tidal instability mechanisms.

For systems with $Q \sim 1$, calculations made by Hirose and Osaki [7] indicate that, in the course of mass transfer through the inner Lagrange point, the disk size increases

until it reaches the tidal radius, where the angular momentum brought by inflowing matter is balanced by that carried away by outflowing matter. The shape of such a disk is a symmetric oval, with the major axis perpendicular to the binary-system axis within several degrees. Unlike close binary systems with a low-mass secondary, in such binaries, the disk remains in a stationary state, and does not precess. Three-dimensional computer simulations of ideal-gas flows in semidetached binaries made by Bisikalo *et al.* [9–11] confirm the formation of a quasi-elliptical disk around the primary.

Here, we present a procedure for synthesizing the light curve of a close binary system in which the white dwarf is surrounded by an elliptical accretion disk. We used the light curve of KU Cyg to test the algorithm. Spectral studies have established the presence of an elliptical accretion disk around the hot primary star in this system.

2. CONSTRUCTING THE DISK SHAPE

We will take the disk to have a complex geometry, corresponding to the intersection of an ellipsoid with semiaxes a, b, and c and two paraboloids specified by the parameter A_p. The value for A_p depends on the angle of rotation of the radius vector about an axis perpendicular to the orbital plane. The ellipsoid specifies the shape of the disk at its outer (lateral) surface, while the paraboloids specify the shape of the inner (upper and lower) surfaces of the accretion disk. We take all lengths to be given in units of the distance between the components a_0, with $a_0 = 1$.

To describe the shape of the elliptical disk, we will use the two coordinate frames $\overline{O}\,\overline{X}\,\overline{Y}\,\overline{Z}$ and $\tilde{O}\,\tilde{X}\,\tilde{Y}\,\tilde{Z}$, in which the $\overline{O}\,\overline{X}$, $\overline{O}\,\overline{Y}$, $\tilde{O}\,\tilde{X}$, and $\tilde{O}\,\tilde{Y}$ axes lie in the orbital plane of the system and the $\overline{O}\,\overline{Z}$ and $\tilde{O}\,\tilde{Z}$ axes are perpendicular to this plane (Fig. 1). A small, spherical star with radius R_w is situated at the focus of the
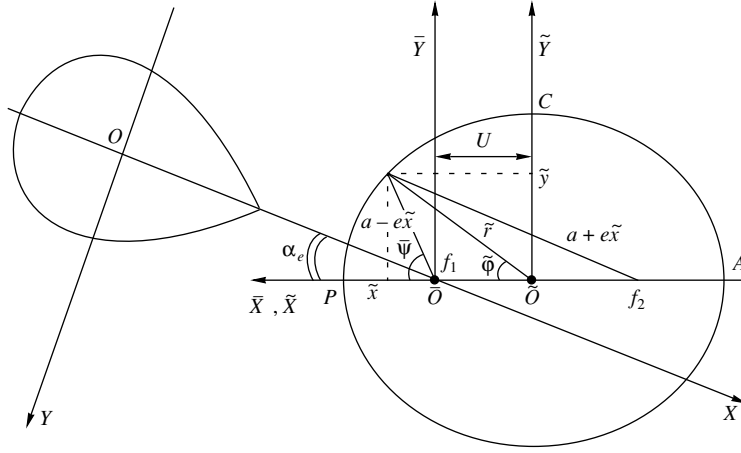
Fig. 1. Coordinate frames used to construct the shape of the elliptical accretion disk: $\overline{O}\overline{X}\overline{Y}\overline{Z}$ (for inner parts of the disk) and $\tilde{O}\tilde{X}\tilde{Y}\tilde{Z}$ (for the ellipsoidal lateral surface of the disk). The $OXYZ$ frame is fixed to the center of mass of the red dwarf. α_e is the azimuth of the disk periastron, and f_1, f_2 are the foci of the disk ellipsoid. The spherical star is located at the focus f_1.

ellipsoid; the origin of the $\overline{O}\overline{X}\overline{Y}\overline{Z}$ frame is fixed to this focus. The $\overline{O}\overline{X}$ axis makes an angle α_e with the line connecting the components of the system, and is directed from the apoastron (A) to the periastron (P) of the disk ellipse; the $\overline{O}\overline{Y}$ axis is perpendicular to the $\overline{O}\overline{X}$ axis and separated from it in the clockwise direction. The center of the $\tilde{O}\tilde{X}\tilde{Y}\tilde{Z}$ frame is at the center of the ellipsoid, and the directions of the $\tilde{O}\tilde{X}$ and $\tilde{O}\tilde{Y}$ axes coincide with those for the $\overline{O}\overline{X}\overline{Y}\overline{Z}$ axes.

The transformation from the $\overline{O}\overline{X}\overline{Y}\overline{Z}$ frame to the $OXYZ$ frame (Fig. 1) fixed to the center of mass of the red dwarf is given by the formulas

$$x = 1 - \bar{x}\cos\alpha_e - \bar{y}\sin\alpha_e,$$
$$y = \bar{x}\sin\alpha_e - \bar{y}\cos\alpha_e, \qquad (1)$$
$$z = \bar{z};$$

the inverse transformation is

$$\bar{x} = (1-x)\cos\alpha_e + y\sin\alpha_e,$$
$$\bar{y} = (1-x)\sin\alpha_e - y\cos\alpha_e, \qquad (2)$$
$$\bar{z} = z.$$

We have for the transformation from the $\overline{O}\overline{X}\overline{Y}\overline{Z}$ frame to the $\tilde{O}\tilde{X}\tilde{Y}\tilde{Z}$ frame

$$\tilde{x} = \bar{x} + U,$$
$$\tilde{y} = \bar{y}, \qquad (3)$$
$$\tilde{z} = \bar{z},$$

where

$$U = \sqrt{a^2 - b^2} = ea = \frac{eb}{\sqrt{1-e^2}} \qquad (4)$$

and e is the eccentricity of the disk ellipse in the orbital plane.

The equation of the ellipsoid describing the lateral surface of the accretion disk in the $\tilde{O}\tilde{X}\tilde{Y}\tilde{Z}$ frame is

$$\frac{\tilde{x}^2}{a^2} + \frac{\tilde{y}^2}{b^2} + \frac{\tilde{z}^2}{c^2} - 1 = 0, \qquad (5)$$

where a, b, and c are the semiaxes of the ellipse: a is in the direction from the ellipsoid periastron to apoastron (section $\tilde{O}A$), b is perpendicular to this direction (section $\tilde{O}C$), and c is perpendicular to the orbital plane.

The paraboloid equation used to define the shape of the inner surface of the disk in the $\overline{O}\overline{X}\overline{Y}\overline{Z}$ frame can be written as

$$\bar{x}^2 + \bar{y}^2 = A_p^2(\overline{\psi})(\bar{z} + \bar{z}_0). \qquad (6)$$

Here, $\overline{\psi}$ is the angle by which the radius vector is rotated from $\overline{O}P$ in the clockwise direction (Fig. 1). The coefficient $A_p(\overline{\psi})$ has the form

$$A_p(\overline{\psi}) = \frac{Ab^2}{a^2(1+e\cos\overline{\psi})} = \frac{A(1-e^2)}{1+e\cos\overline{\psi}}, \qquad (7)$$

where $A = $ const. When $e = 0$, this coincides with the paraboloid constant A_{par} [12] describing the shape of the inner surfaces of a circular disk, $A_p = A = $ const; in the case of an elliptical disk, we obtain at periastron ($\overline{\psi} = 0.0$) $A_p = A(1-e)$, and at apoastron ($\overline{\psi} = \pi$) $A_p = A(1+e)$.

The vertices of the paraboloids are shifted by z_0 relative to the binary's orbital plane. We will determine z_0 from (6), much as we did in our previous study [13]. We assume that the vertex of the paraboloid is displaced toward negative z by z_0, such that, for $\overline{\psi} = 0.0$ (at disk periastron), the paraboloid intersects the orbital plane at a distance R_w from the center of the white dwarf. In this case,

$$z_0 = \frac{R_w^2}{A^2(1-e)^2}. \tag{8}$$

Taking into account the relations for $A_p(\overline{\psi})$ and z_0, we use the following equation to describe the shape of the inner disk surface:

$$\overline{\rho}^2 = \overline{x}^2 + \overline{y}^2 = \frac{A^2(1-e^2)^2}{(1+e\cos\overline{\psi})^2}\left(\overline{z} + \frac{R_w^2}{A^2(1-e)^2}\right). \tag{9}$$

The $\tilde{O}\tilde{X}\tilde{Y}\tilde{Z}$ frame is more convenient for separating the ellipsoidal (lateral) surface of the disk into area elements. Let $\tilde{\phi}$ be the clockwise angle between the positive $\tilde{O}\tilde{X}$ axis and the radius vector $\tilde{r} = \sqrt{\tilde{x}^2 + \tilde{y}^2 + \tilde{z}^2}$ from the center of the ellipsoid to the center of an area element on the disk, with $\tilde{\eta}$ being the angle between the $\tilde{O}\tilde{Z}$ axis and $\tilde{r}$. In the spherical coordinates $(\tilde{r}, \tilde{\eta}, \tilde{\phi})$, the ellipsoid surface is given by the formulas

$$\tilde{x} = \tilde{r}\cos\tilde{\phi}\sin\tilde{\eta},$$

$$\tilde{y} = \tilde{r}\sin\tilde{\phi}\sin\tilde{\eta}, \tag{10}$$

$$\tilde{z} = \tilde{r}\cos\tilde{\eta},$$

where

$$\tilde{r} = \frac{1}{\sqrt{\dfrac{\sin^2\tilde{\eta}\cos^2\tilde{\phi}}{a^2} + \dfrac{\sin^2\tilde{\eta}\cos^2\tilde{\phi}}{b^2} + \dfrac{\cos^2\tilde{\eta}}{c^2}}}. \tag{11}$$

The area element with coordinates $(\tilde{r}, \tilde{\eta}, \tilde{\phi})$ is defined by the standard formula [12, 13]

$$dS_{ell} = \frac{\tilde{r}^2\sin\tilde{\eta}\,d\tilde{\eta}\,d\tilde{\phi}}{\cos\tilde{\delta}}. \tag{12}$$

Here, $\cos\tilde{\delta} = \tilde{\mathbf{r}}\tilde{\mathbf{n}}/|\tilde{\mathbf{r}}|$,

$$\tilde{\mathbf{n}} = \left\{\frac{\tilde{x}}{a^2 N_*}, \frac{\tilde{y}}{b^2 N_*}, \frac{\tilde{z}}{c^2 N_*}\right\} \tag{13}$$

and is the normal vector to the ellipsoid surface at the center of the area element, where

$$N_* = \sqrt{\frac{\tilde{x}^2}{a^4} + \frac{\tilde{y}^2}{b^4} + \frac{\tilde{z}^2}{c^4}}. \tag{14}$$

Substituting the expressions for $\tilde{r}$ and $\cos\tilde{\delta}$ in (12), we obtain for an area element on the lateral surface of the disk

$$dS_{ell} = N_*\tilde{r}^3\sin\tilde{\eta}\,d\tilde{\eta}\,d\tilde{\phi}. \tag{15}$$

We will divide the inner (parabolic) surface of the disk into area elements in the $\overline{O}\overline{X}\overline{Y}\overline{Z}$ frame. Let $\overline{R}(\overline{\eta}, \overline{\psi})$ be the radius vector from the vertex of the paraboloid to the center of an area element, $\overline{\eta}$ be the angle between the $\overline{O}\overline{Z}$ axis and $\overline{R}(\overline{\eta}, \overline{\psi})$, and $\overline{\psi}$ be the angle in the orbital plane between the positive $\overline{O}\overline{X}$ axis and $\overline{\rho}(\overline{\eta}, \overline{\psi})$, which is the projection of $\overline{R}(\overline{\eta}, \overline{\psi})$ onto the orbital plane:

$$\overline{\rho}(\overline{\eta}, \overline{\psi}) = \overline{R}(\overline{\eta}, \overline{\psi})\sin\overline{\eta}. \tag{16}$$

The coordinates of the center of the area element in the $\overline{O}\overline{X}\overline{Y}\overline{Z}$ frame are

$$\overline{x} = \overline{\rho}\cos\overline{\psi} = \overline{R}\sin\overline{\eta}\cos\overline{\psi},$$

$$\overline{y} = \overline{\rho}\sin\overline{\psi} = \overline{R}\sin\overline{\eta}\sin\overline{\psi}, \tag{17}$$

$$\overline{z} = \overline{R}\cos\overline{\eta} - z_0.$$

We will specify divisions in z with step $\Delta z = (z_{cr} + z_0)/N_z$, where N_z is the number of steps. Then, having specified divisions in the angle $\overline{\psi}$ with step $\Delta\overline{\psi}$, we will determine the value $\overline{\rho}_{ij}$ for each z_i and $\overline{\psi}_j$ in accordance with (9). From (17), we calculate the coordinates x_{ij} and y_{ij} for the center of the area element and the corresponding angle $\overline{\eta}_{ij}$ from the relation $\tan\overline{\eta}_{ij} = \overline{\rho}_{ij}/(z_i + z_0)$.

The components of the vector normal to the inner disk surface are

$$\overline{n}_x = -\frac{\Omega_x'}{|\Omega'|}, \quad \overline{n}_y = -\frac{\Omega_y'}{|\Omega'|}, \quad \overline{n}_z = -\frac{\Omega_z'}{|\Omega'|}, \tag{18}$$

where the potential specified by the equation

$$\Omega = (\overline{x}^2 + \overline{y}^2)\frac{(1 + e\cos\overline{\psi}(\overline{x}, \overline{y}))^2}{A^2(1-e^2)^2} \\ - \overline{z} - \frac{R_w^2}{A^2(1-e)^2}, \tag{19}$$

describes the paraboloid surface of the disk. Here, $|\Omega'| = \sqrt{\Omega_x'^2 + \Omega_y'^2 + \Omega_z'^2}$; to calculate the derivatives of the

potential, we use the fact that $\cos\overline{\psi}\,(\bar{x},\bar{y}) = \bar{x}/\sqrt{\bar{x}^2 + \bar{y}^2}$. Then,

$$\Omega'_x = \bar{\rho}G_0(\cos\overline{\psi} + e),$$

$$\Omega'_y = G_0\bar{y} = G_0\bar{\rho}\sin\overline{\psi},$$

$$\Omega'_z = -1, \tag{20}$$

$$|\Omega'| = G_0\sqrt{\bar{\rho}^2(1 + e^2 + 2e\cos\overline{\psi}) + G_0^{-2}},$$

where

$$G_0 = \frac{2(1 + e\cos\overline{\psi})}{A^2(1 - e^2)^2}. \tag{21}$$

When $e = 0$, we obtain the relations previously derived in [12]: $\Omega'_x = 2\bar{x}/A^2$, $\Omega'_y = 2\bar{y}/A^2$, $\Omega'_z = -1$, $|\Omega'| = \frac{2}{A^2}\sqrt{\bar{x}^2 + \bar{y}^2 + \frac{A^4}{4}}$. Thus, the components of the vector normal to the inner disk paraboloid surface are

$$\bar{n}_x = \frac{-(\cos\overline{\psi} + e)\bar{\rho}}{\sqrt{\bar{\rho}^2(1 + e^2 + 2e\cos\overline{\psi}) + G_0^{-2}}},$$

$$\bar{n}_y = \frac{-\bar{\rho}\sin\overline{\psi}}{\sqrt{\bar{\rho}^2(1 + e^2 + 2e\cos\overline{\psi}) + G_0^{-2}}}, \tag{22}$$

$$\bar{n}_z = \frac{G_0^{-1}}{\sqrt{\bar{\rho}^2(1 + e^2 + 2e\cos\overline{\psi}) + G_0^{-2}}}.$$

For the paraboloidal disk, an area element is defined by a formula similar to that for an elliptical disk:

$$dS_{parab} = \frac{\overline{R}^2\sin\overline{\eta}\,d\overline{\eta}\,d\overline{\psi}}{\cos\overline{\delta}}, \quad \cos\overline{\delta} = \frac{\overline{\mathbf{R}}\overline{\mathbf{n}}}{|\overline{\mathbf{R}}|}.$$

Substituting $\dfrac{\overline{R}}{|\overline{\mathbf{R}}|} = \left\{ \dfrac{\bar{x}}{\overline{R}}, \dfrac{\bar{y}}{\overline{R}}, \dfrac{\bar{z} + \bar{z}_0}{\overline{R}} \right\}$ and $\bar{\mathbf{n}} = \{\bar{n}_x, \bar{n}_y,$

$\bar{n}_z\}$ from relation (22), we obtain

$$dS_{parab} \tag{23}$$
$$= \frac{2\bar{\rho}(\bar{\rho}^2 + A_p^4(\overline{\psi}))\sqrt{\bar{\rho}^2(1 + e^2 + 2e\cos\overline{\psi}) + G_0^{-2}}\,d\overline{\eta}\,d\overline{\psi}}{A_p^4(\overline{\psi})(1 + e\cos\overline{\psi})}.$$

Let us determine the height of the outer edge of the disk, i.e., the z coordinate of the line of intersection of the ellipsoidal and paraboloidal parts of the elliptical disk. We will write equations for these surfaces in the $\overline{O}\overline{X}\overline{Y}\overline{Z}$ frame for points in the plane $z = \text{const}$ for which $\bar{x} = -U$ (in the $\tilde{O}\tilde{X}\tilde{Y}\tilde{Z}$ frame, these are points for which $\tilde{x} = 0$; this is valid, in particular, for the angle

$\tilde{\phi} = 0.5\pi$, where $\cos\overline{\psi} = -e$). At this point, the paraboloid equation (9) has the form

$$U^2 + \bar{y}^2 = \bar{z}A^2 + \frac{R_w^2}{(1 - e)^2}. \tag{24}$$

The ellipsoid equation at a point where $\tilde{\phi} = 0.5\pi$ is

$$\frac{\bar{y}^2}{b^2} + \frac{\bar{z}^2}{c^2} - 1 = 0. \tag{25}$$

Solving (24) and (25) simultaneously for $\bar{z}$ yields for the height of the upper disk edge $\bar{z}_{cr}$

$$\bar{z}_{cr} = cl\left(\sqrt{\frac{c^2A^4}{4b^4} - \frac{1}{b^2}\left[\frac{R_w^2}{(1 - e)^2} - a^2\right]} - \frac{cA^2}{2b^2}\right), \tag{26}$$

where $l = +1$ and -1 for disk edge heights along the positive and negative $\overline{O}\overline{Z}$ axis, respectively, and $b^2 = a^2(1 - e^2)$. For a circular disk with $e = 0$ and $a = b$, formula (26) becomes the formula for $\bar{z}_{cr}$ from [13].

3. HEATING OF THE DISK AND RED STAR

3.1. Heating of the Disk Surface

To calculate the temperature of an area element on the disk surface, we took into account the following factors.

(1) The temperature of an area element depends on the distance between its center and the white-dwarf surface. Near the surface of the white dwarf, we take the temperature of an area element on the disk to be equal to that of the star. The heating of the disk is associated with the transformation of the gravitational energy of matter into heat in the course of its spiral-like motion toward the white-dwarf surface. It is usually assumed that this temperature follows the dependence

$$T_g = T_w\left(\frac{R_w}{r}\right)^{\alpha_g}, \tag{27}$$

where r is the distance from the white-dwarf center to the center of the area element on the disk. To first approximation, the parameter α_g is generally taken to be $\alpha_g = 0.75$ [14], assuming that each point on the disk surface radiates as a blackbody. However, studies of the temperature distribution over the disk surface indicate that α_g deviates appreciably from 0.75 [15, 16]: $\alpha_g \sim 0.3$–0.75.

(2) The paraboloidal parts of the disk are heated by the white dwarf. We will take this heating into account in the $\overline{O}\overline{X}\overline{Y}\overline{Z}$ frame. Let the coordinates for an area element on the disk be $(\bar{x}_d, \bar{y}_d, \bar{z}_d)$, and for an area element on the white dwarf be $(\bar{x}_w, \bar{y}_w, \bar{z}_w)$. The disk area element will be heated by radiation only from areas on

the white dwarf that are located in the same sector as it is, that is, under the following conditions: (1) if $\bar{z}_d > 0$, then $\bar{z}_w > 0$; (2) if the area element on the disk has azimuth $\bar{\psi}_d$, it can be heated only by areas on the white dwarf with azimuths $\bar{\psi}_d - \frac{\pi}{2} < \bar{\psi}_w < \bar{\psi}_d + \frac{\pi}{2}$; (3) $\cos\bar{\beta}_w \geq 0$, where $\bar{\beta}_w$ is the angle between the radius vector $\bar{\rho}_w$ from the point $(\bar{x}_w, \bar{y}_w, \bar{z}_w)$ on the white-dwarf surface to the point $(\bar{x}_d, \bar{y}_d, \bar{z}_d)$ on the disk and the normal $\bar{\mathbf{n}}$ to the area on the white dwarf:

$$\bar{\rho}_w = \sqrt{(\bar{x}_d - \bar{x}_w)^2 + (\bar{y}_d - \bar{y}_w)^2 + (\bar{z}_d - \bar{z}_w)^2}, \quad (28)$$

$$\cos\bar{\beta}_w = \frac{\bar{x}_w(\bar{x}_d - \bar{x}_w) + \bar{y}_w(\bar{y}_d - \bar{y}_w) + \bar{z}_w(\bar{z}_d - \bar{z}_w)}{R_w\sqrt{(\bar{x}_d - \bar{x}_w)^2 + (\bar{y}_d - \bar{y}_w)^2 + (\bar{z}_d - \bar{z}_w)^2}}. \quad (29)$$

Having summed the radiation from those areas on the white dwarf satisfying these conditions, we obtain the flux f_w heating the area element on the disk:

$$f_w = \sigma T_w^4 R_w^2 \Sigma \cos\bar{\alpha}_w \sin\bar{\eta}_w d\bar{\eta}_w d\bar{\phi}_w. \quad (30)$$

Here, σ is the Stefan–Boltzmann constant, $R_w^2 \sin\bar{\eta}_w d\bar{\eta}_w d\bar{\phi}_w$ is an area element on the white dwarf, and $\bar{\alpha}_w$ is the angle between the normal $\bar{\mathbf{n}}_d$ to the area element [see (22)] and the radius vector $\bar{\rho}_d$, such that $\bar{\rho}_d = -\bar{\rho}_w$:

$$\cos\bar{\alpha}_w = \frac{\bar{\mathbf{n}}_d \cdot \bar{\rho}_d}{|\bar{\rho}_d|}. \quad (31)$$

Thus, due to heating by radiation, the temperature of an area element on the parabolical portion of the disk will increase according to the relation

$$T = \sqrt[4]{T_g^4 + \frac{\kappa_{opt} f_w \cos\bar{\alpha}_w}{4\pi\sigma\bar{\rho}_w^2}}. \quad (32)$$

(3) For areas on the paraboloidal disk surface, heating by the red dwarf's radiation must also be taken into account. Since the red dwarf's radiation is small compared to that of the hot star, and the radiation from areas of the red star near the orbital plane is obscured by the disk edge, we will take an area element on the disk to be heated by the radiation form a point source located at the pole of the red star in the corresponding hemisphere with coordinates $(\cos\alpha_e, \sin\alpha_e, z_s)$ in the $\overline{O}\overline{X}\overline{Y}\overline{Z}$ frame and luminosity L_{pol} equal to that of the polar regions of the red star. This heating does not occur if the area element is shielded from the red dwarf's radiation by the edge of the disk or the white dwarf. Let us now consider these conditions in more detail.

Area elements on the paraboloidal disk surface will be heated only if the angle between the radius vector ρ_s from the center of the area element to the red-dwarf

pole and the normal to the area element [see (22)] does not exceed 90°; i.e.,

$$\cos\bar{\alpha}_s$$
$$= \frac{(\cos\alpha_e - \bar{x}_d)\bar{n}_x + (\sin\alpha_e - \bar{y}_d)\bar{n}_y + (\bar{z}_s - \bar{z}_d)\bar{n}_z}{\sqrt{(\cos\alpha_e - \bar{x}_d)^2 + (\sin\alpha_e - \bar{y}_d)^2 + (\bar{z}_s - \bar{z}_d)^2}} \geq 0. \quad (33)$$

To check whether an area element on the inner disk surface can be shielded from the red dwarf's radiation by the edge of the disk, consider the equation for a line along the vector $\bar{\rho}_s$ passing through the center of the area element:

$$\bar{x} = \bar{x}_d + \tau\bar{n}_{\rho x},$$
$$\bar{y} = \bar{y}_d + \tau\bar{n}_{\rho y}, \quad (34)$$
$$\bar{z} = \bar{z}_d + \tau\bar{n}_{\rho z},$$

where

$$\bar{n}_\rho = \left\{ \frac{\cos\alpha_e - \bar{x}_d}{|\bar{\rho}_s|}, \frac{\sin\alpha_e - \bar{y}_d}{|\bar{\rho}_s|}, \frac{\bar{z}_s - \bar{z}_d}{|\bar{\rho}_s|} \right\}, \quad (35)$$

$$|\bar{\rho}_s| = \sqrt{(\cos\alpha_e - \bar{x}_d)^2 + (\sin\alpha_e - \bar{y}_d)^2 + (\bar{z}_s - \bar{z}_d)^2}. \quad (36)$$

Let us substitute (34) into the equation for the disk ellipsoid in the $\overline{O}\overline{X}\overline{Y}\overline{Z}$ frame

$$\frac{(\bar{x} + ea)^2}{a^2} + \frac{\bar{y}^2}{a^2(1 - e^2)} + \frac{\bar{z}^2}{c^2} - 1 = 0 \quad (37)$$

and solve this equation for the parameter τ. The intersection of the line (34) with the ellipsoid in the region between the white dwarf and the red dwarf occurs when

$$\tau = -\frac{B}{A} + \sqrt{\left(\frac{B}{A}\right)^2 - \frac{C}{A}}, \text{ where}$$

$$A = \bar{n}_{\rho x}^2(1 - e^2) + \bar{n}_{\rho y}^2 + \bar{n}_{\rho z}^2\frac{b^2}{c^2},$$

$$B = (1 - e^2)(\bar{x}_d + ea)\bar{n}_{\rho x} + \bar{y}_d\bar{n}_{\rho y} + \frac{b^2}{c^2}\bar{z}_d\bar{n}_{\rho z}, \quad (38)$$

$$C = (1 - e^2)\left[(\bar{x}_d + ea)^2 + \frac{\bar{y}_d^2}{1 - e^2} + \frac{a^2}{c^2}\bar{z}_d^2 - a^2 \right].$$

The Z coordinate of the intersection point is $\bar{z}_{ell} = \bar{z}_d + \tau\bar{n}_{\rho z}$. The edge of the disk shields the area element on the disk from heating by the red dwarf's radiation if $\bar{z}_{ell} \leq \bar{z}_{cr}$, where the z coordinate $\bar{z}_{cr}$ of the upper edge of the disk is calculated using (26).

If the edge of the disk does not shield an area element on the disk from heating by the red star's radiation, we must check if the element could be shielded by

the white dwarf, i.e., if the ray $\bar{\rho}_s$ (34) intersects the body of the white dwarf specified by the equation

$$\bar{x}^2 + \bar{y}^2 + \bar{z}^2 - R_w^2 = 0. \tag{39}$$

The corresponding coefficients A, B, and C specifying the parameter τ are calculated in the same way as they are for the case $e = 0$ [13, formulas (24), (25)], with the only difference being that the components of the directional vector $\bar{n}_\rho$, $\bar{n}_{\rho x}$, $\bar{n}_{\rho y}$, $\bar{n}_{\rho z}$ are given by formulas (35), (36). An area element on the disk is heated either when $D = (B/A)^2 - C/A < 0$ (the ray $\bar{\rho}_s$ does not intersect the white dwarf) or when $D > 0$ (both intersections of the ray $\bar{\rho}_s$ with the white dwarf are in the lower hemisphere of the star; i.e., $\bar{z}_{ell\pm} = \bar{z}_d + (-B/A \pm \sqrt{D})\bar{n}_{\rho z} < 0$).

If an area element on the disk is heated by radiation from the red star, its temperature increases in accordance with the relation

$$T_r = \sqrt[4]{T_g^4 + \frac{\kappa_{opt}f_w\cos\bar{\alpha}_w}{4\pi\sigma\bar{\rho}_w^2} + \frac{\kappa_{opt}L_{pol}\cos\bar{\alpha}_s}{4\pi\sigma\bar{\rho}_s^2}}, \tag{40}$$

where κ_{opt} is the coefficient for reprocessing of the red dwarf's optical radiation by the disk material; L_{pol} is the radiation flux from circumpolar regions of the red star; $\cos\bar{\alpha}_s$ and $\bar{\rho}_s$ are calculated using (33) and (36); and $\bar{\rho}_w$, f_w, and $\cos\bar{\alpha}_w$ are calculated using (28), (30), and (31).

(4) The procedure for calculating the temperature of area elements on the lateral disk surface is presented in [12], with the normal vectors to the lateral disk surface specified by relation (13). In this case, we use the $\tilde{O}\tilde{X}\tilde{Y}\tilde{Z}$ frame. We take the lateral disk surface to be heated by radiation form a point source at the center of mass of the red star. This simplification does not introduce large errors into the results, due to the low temperature of the secondary; however, it appreciably speeds up the calculations. The temperature of an area element on the lateral surface of the disk will be specified by the relation

$$T_r = \sqrt[4]{T_g^4 + \frac{\kappa_{opt}L_s\cos\tilde{\alpha}_L}{4\pi\sigma\tilde{\rho}_L^2}}. \tag{41}$$

Here, $\tilde{\rho}_L$ is the distance between the center of the disk area element with coordinates $(\tilde{x}_d, \tilde{y}_d, \tilde{z}_d)$ and the center of mass of the optical star with coordinates $(\cos\alpha_e, \sin\alpha_e, 0)$,

$$\bar{\rho}_L = \sqrt{(\cos\alpha_e - \tilde{x}_d)^2 + (\sin\alpha_e - \tilde{y}_d)^2 + \tilde{z}_d^2}, \tag{42}$$

L_s is the red-dwarf luminosity in the absence of heating from its companion, $\tilde{\alpha}_L$ is the angle between the radius

vector $\tilde{\rho}_L$ and the normal to the area element on the disk (13),

$$\cos\tilde{\alpha}_L = \frac{(\cos\alpha_e - \tilde{x}_d)\tilde{n}_x + (\sin\alpha_e - \tilde{y}_d)\tilde{n}_y - \tilde{z}_d\tilde{n}_z}{\sqrt{(\cos\alpha_e - \tilde{x}_d)^2 + (\sin\alpha_e - \tilde{y}_d)^2 + \tilde{z}_d^2}}. \tag{43}$$

If $\cos\tilde{\alpha}_L \leq 0$ (or $\tilde{x}_d\cos\alpha_e + \tilde{y}_d\sin\alpha_e \leq 0$), we are dealing with area elements on the side of the lateral surface of the elliptical disk that is opposite to the red star, and is therefore not heated by its radiation.

Figure 2 illustrates a close binary system at orbital phase $\varphi = 0.3$. The crosses mark the centers of area elements on the disk that are heated by the red dwarf's radiation. The dots mark the centers of those areas that are shielded from the red star's radiation by the edge of the disk and the white dwarf.

3.2. Heating of the Red-Dwarf Surface

Our model assumes that the red star is heated only by the radiation of the white dwarf. We will perform the calculations in the $OXYZ$ frame fixed to the secondary (Fig. 1). Let an area element on the surface of the red star have coordinates (x_{rs}, y_{rs}, z_{rs}). We will assume that the star is heated only by radiation from the polar regions of the white dwarf, i.e., from points with coordinates $(1, 0, l_w R_w)$. The values $l_w = +1$ and $l_w = -1$ correspond to the white-dwarf pole being in the positive and negative OZ directions, respectively. An area element on the surface of the red star can be heated only if

$$\cos\gamma_{rs} \geq 0, \tag{44}$$

where γ_s is the angle between the normal vector $\mathbf{n}_{rs}$ to the stellar surface at the center of the area element and the radius vector from the point (x_{rs}, y_{rs}, z_{rs}) to the point with the coordinates of the white dwarf's pole, $\rho_{rs} = \{1 - x_{rs}, -y_{rs}, l_w R_w - z_{rs}\}$. Denoting the components of the normal to the stellar surface n_{rx}, n_{ry}, n_{rz} (formulas for their calculation are presented in [17]), we obtain

$$\cos\gamma_{rs} = \frac{\rho_{rs} \cdot \mathbf{n}_{rs}}{|\rho_{rs}|}$$
$$= \frac{(1 - x_{rs})n_{rx} - y_{rs}n_{ry} + (l_w R_w - z_{rs})n_{rz}}{\sqrt{(1 - x_{rs})^2 + y_{rs}^2 + (l_w R_w - z_{rs})^2}}. \tag{45}$$

If condition (44) is not satisfied, the area (x_{rs}, y_{rs}, z_{rs}) is located on the back hemisphere of the red star and is not heated. There is also no heating if (44) is satisfied, but the area element on the star is shielded by the disk edge.

We can test for shielding using the method described in detail above: in parametrical form, we construct a straight line passing through the area element and the white dwarf's pole, parallel to the unit radius vector $\rho_{rs}/|\rho_{rs}|$ (with components ρ_{rs}, ρ_{ys}, ρ_{zs}),
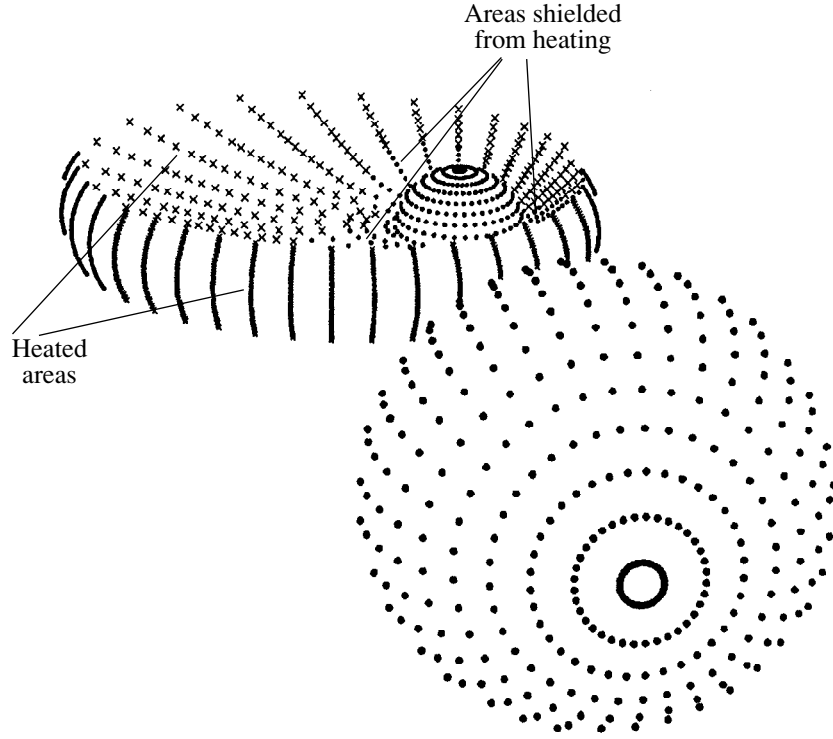
$$x = x_{rs} + t\rho_{xs},$$

Fig. 2. Projection onto the plane of the sky of a close binary system consisting of a red dwarf and spherical star surrounded by an elliptical accretion disk at orbital phase $\varphi = 0.3$ (computer simulation). The system parameters are: $q = M_1/M_2 = 2.0$, $i = 70°$, $e = 0.5$, disk radius at apoastron $R_d = 0.54a_0$, disk semi-major axis $a = 0.362a_0$, $\alpha_e = 60°$, $R_w = 0.0856a_0$, half-height of the disk edge above the orbital plane $h/2 = 0.062a_0$. The crosses mark areas on the disk surface that are not shielded from the red star's radiation, and are therefore heated. The dots mark areas that are shielded from the red star's radiation by the disk edge or the body of the spherical component.

$$y = y_{rs} + t\rho_{ys}, \qquad (46)$$

$$z = z_{rs} + t\rho_{zs},$$

and then check if it crosses the disk surface. The equation for the disk ellipsoid in the $OXYZ$ frame is

$$\frac{[(1-x)\cos\alpha_e + y\sin(\alpha_e + ea)]^2}{a^2}$$
$$+ \frac{[(1-x)\sin\alpha_e - y\cos\alpha_e]^2}{b^2} + \frac{z^2}{c^2} = 1. \qquad (47)$$

Simultaneous solution of (46) and (47) for the parameter t yields the z coordinates for the two points of intersection of the straight line (46) and the lateral disk surface: $z_{t\pm} = z_{rs} + t_{\pm}\rho_{zs}$, where

$$t_{\pm} = \frac{B}{A} \pm \sqrt{\left(\frac{B}{A}\right)^2 - \frac{C}{A}}, \qquad (48)$$

$$A = (\rho_{xs}\cos\alpha_e - \rho_{ys}\sin\alpha_e)^2$$
$$+ \frac{(\rho_{xs}\sin\alpha_e + \rho_{ys}\cos\alpha_e)^2}{1-e^2} + \left(\frac{a}{c}\right)^2\rho_{zs}^2,$$

$$B = (\rho_{xs}\cos\alpha_e - \rho_{ys}\sin\alpha_e)[(1-x_{rs})\cos\alpha_e$$

$$+ y_{rs}\sin\alpha_e + ea]$$
$$+ \frac{(\rho_{xs}\sin\alpha_e + \rho_{ys}\cos\alpha_e)[(1-x_{rs})\sin\alpha_e - y_{rs}\cos\alpha_e]}{1-e^2}$$

$$- \left(\frac{a}{c}\right)^2 z_{rs}\rho_{zs}, \qquad (49)$$

$$C = [(1-x_{rs})\cos\alpha_e + y_{rs}\sin\alpha_e + ea]^2$$
$$+ \frac{[(1-x_{rs})\sin\alpha_e - y_{rs}\cos\alpha_e]^2}{1-e^2} + \left(\frac{a}{c}\right)^2 z_{rs}^2 - a^2.$$

We choose the value for t for which the point of intersection of the line (46) with the disk is between the components of the system. In this case, $x_{rs} + t\rho_{xs} < 1$. For the positive hemisphere of the red component, the condition for heating of an area element on its surface is $z_t > z_{cr}$; for the negative hemisphere, it is $z_t < z_{cr}$. Due to heating by the white dwarf's radiation, the temperature of an area element on the secondary increases according to the relation

$$T = \sqrt{T_{\text{eff}}^4 + \frac{\kappa L_w \cos\gamma_{rs}}{4\pi\sigma\rho_{rs}^2}}, \qquad (50)$$

where $L_w = 4\pi\sigma T_w^4 R_w^2$ is the bolometric luminosity of the white dwarf, and κ is the coefficient for reprocessing of the hot white-dwarf radiation by the material of the secondary.

4. VERIFYING THE COMPONENT ECLIPSE CONDITION

After we have determined the disk shape and calculated all the parameters (coordinates, areas, normal vectors, and temperature) for area elements on the disk, we must check whether any components of the system (the red dwarf, white dwarf, paraboloidal, and the ellipsoidal parts of the elliptical disk) are eclipsed at the orbital phase of the light curve φ_0 under consideration. The general principle underlying the procedure for verifying the visibility of areas on the surfaces of the binary components is as follows. Knowing the coordinates (x_j, y_i, z_j) for the jth area element in the $OXYZ$ frame and the components of the unit vector $\mathbf{o}$ parallel to the line of sight

$$o_x = \cos\varphi_0 \sin i,$$

$$o_y = \sin\varphi_0 \sin i, \qquad (51)$$

$$o_z = \cos i,$$

where i is the inclination of the orbit, we can determine the angle γ between the normal vector to the area element $\mathbf{n}$ and the line of sight:

$$\cos\gamma = \mathbf{n} \cdot \mathbf{o}. \qquad (52)$$

The visibility condition for the area is

$$\cos\gamma > 0. \qquad (53)$$

If this condition is fulfilled, we check for eclipse of the area element by the other components of the system. To this end, we draw a straight line in parametric form through the center of the area element parallel to the line of sight:

$$x = x_j + to_x,$$

$$y = y_j + to_y, \qquad (54)$$

$$z = z_j + to_z,$$

and determine whether it crosses the surfaces of other components located between the observer and the area element. For this purpose, we must solve the system of equations (54) simultaneously with the equation describing the shape of the component under consideration in the $OXYZ$ frame for the parameter t, taking into account any supplementary conditions. The absence of a solution indicates that the line of sight does not cross the body of that particular component. The area element is also not shielded if there is an intersection beyond the region where the supplementary conditions are satisfied or beyond the region between the observer and the area element. In this case, its contribution to the total flux of

the system must be taken into account in accordance with the calculated temperature, size, and viewing angle γ for this element.

5. KU Cyg LIGHT CURVE ANALYSIS

To test our code for the synthesis of the light curve of a close binary system with an elliptical disk, we used the b light curve for the Algol-like binary KU Cyg (Fig. 3a) obtained by Olson [18] via the convolution of ~800 individual photometric observations made in the I(Kron)$ybvu$ system in 1982–1990. In 1997, Smak [19] reported the detection of an elliptical disk around the hot component of this long-period binary (BD + 46°2879), based on a study of the H_α line profile. The photometric and spectroscopic properties of KU Cyg are similar to those of SU UMa dwarf novae [8, 20]. In these systems, the disk occasionally becomes very large and elliptical, and begins to precess. Tidal effects removing angular momentum from the outer parts of the disk intensify the accretion on the hot star and manifest as a brightening of the object. The characteristic timescale for these processes in KU Cyg is several years.

In accordance with its orbital period ($P = 38^{\rm d}.4$), KU Cyg belongs to the class of long-period Algol-like stars. The system's primary—a comparatively massive hot star that is far from filling its Roche lobe and is surrounded by a large accretion disk—undergoes total eclipses. The most significant contributions to photometric and spectral studies of this system have been made by Popper [21, 22], Olson $et\ al.$ [18], Olson [23, 24], Zola [25], and Smak [19].

The spectral type (K5 III) of the secondary (a cool star that completely fills its Roche lobe) is consistent with the observed color indices of the star. The situation for the primary is not so clear. Its colors during the primary eclipse are completely nonstellar due to the substantial contribution of the unobscured part of the disk. According to its color indices, the spectral type of the primary ranges from M to G. Judging from its mass and radius, the primary is a main-sequence star with spectral type ~B7V and effective temperature $T_1 \sim 13\,300$ K. However, Popper [21, 22] determined the observed spectral type to be F4p, and, according to Olson [23], the spectrum resembles that of a supergiant and the colors correspond to a temperature of $T_1 \sim 7500$ K. Based on photometric data, Zola [25] estimated the temperature of the primary to be $T_1 \sim 10\,330$ K. This temperature discrepancy is thought to result from absorption of the primary's radiation in the disk atmosphere, whose thickness is comparable to the size of the disk itself. If the orbital inclination is high, such an extended atmosphere completely obscures the visible hemisphere of the primary. The uncertainty in T_1, however, affects only slightly the final geometrical parameters and the light radii of the stars. Uncertainties in the masses and radii of the components are determined primarily by
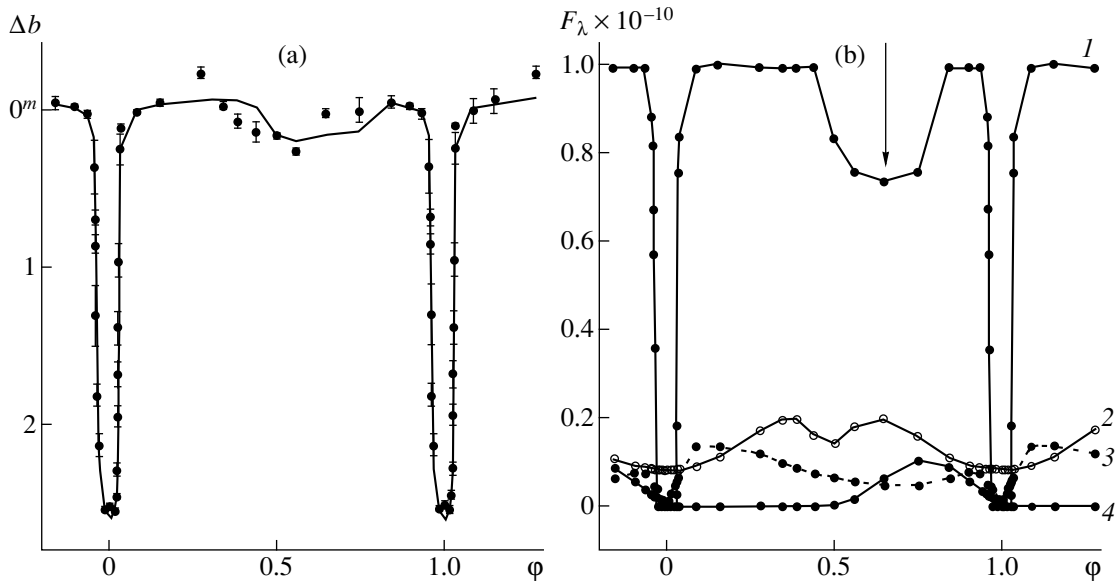
Fig. 3. (a) Observations of KU Cyg with their rms errors and the theoretical b light curve (solid) calculated using a model with an elliptical disk around the primary, with the parameters presented in the table; (b) contributions from various components to the total radiation of the system as a function of orbital phase calculated for a elliptical-disk model: (*1*) primary, (*2*) red dwarf, (*3*) accretion disk, (*4*) "typical" hot spot. The flux is given in arbitrary units F_λ (see the text). The vertical arrow indicates the orbital phase at which the disk periastron intersects the line of sight between the observer and primary.

uncertainties in the half-amplitude of the radial-velocity curve K_1 and the component mass ratio q.

The radial-velocity curve for the secondary is clearly sinusoidal [18, 19, 22]; its half-amplitude ($K_2 = 90.7 \pm 0.8$ km/s) is known with good accuracy. The radial velocities of the primary [18, 22] have a large scatter. The value of K_1 depends on the section of the curve used to determine the half-amplitude, and ranges from $K_1 \sim 7$ km/s (obtained by Olson [23, 24] using all points of the radial-velocity curve at all phases) to 17 km/s (obtained by Popper [21, 22] using observations at phases 0.15–0.85). This scatter corresponds to the uncertainty in $Q = 1/q = M_2/M_1$, from 0.08 to 0.19.

The light curve of KU Cyg has been analyzed by Olson [23, 26], Zola [25], and Olson *et al.* [18] using Wilson–Devinney algorithm. Their results are not very consistent; however, all these authors conclude that solutions with $Q < 0.10$ should be rejected. Solutions for $Q \sim 0.1$–0.3 are virtually indistinguishable. The inclination of the orbit of KU Cyg is rather high ($i \sim 86°$–$86°.5$); the radius of the primary is $r_1 \sim (0.043$–$0.047)a_0$, where a_0 is the distance between the components.

Smak [19] analyzed H_α line profiles obtained in March, 1989 at orbital phase $\varphi = -0.0447$, when the central part of the disk was partially obscured by the secondary. Investigations of the H_α line profile have demonstrated the existence of an elliptical disk with a rather high eccentricity ($e = 0.31 \pm 0.07$ for a semimajor axis $a = (0.48 \pm 0.01)a_0$) and a finite geometrical width for the disk. During the observations of Smak [19], KU

Cyg was $\sim 0^m.25$ brighter then in its quiescent state. In 1990, KU Cyg was still in the active state; however, the accretion disk eccentricity decreased to $e \sim 0.2$ and the semimajor axis of the disk decreased to $a \sim 0.41a_0$.

A similar brightening of the system by $\sim 0^m.2$ in the y filter was also observed in 1984. In 1949–1954, KU Cyg was not active. Radial-velocity data obtained at that time by Popper [22] indicated that the disk was circular: $a \approx 0.3a_0$, $e \approx 0$. Together, these facts provide evidence that the size and eccentricity of the disk in KU Cyg are variable. According to [27], the time scale for the perturbations responsible for the increase in disk eccentricity is $\tau_{pert} \approx 6$ yrs, while the disk precession period varies between $P_{prec} \approx 3$ yrs at $a \approx 0.50a_0$ and $P_{prec} \approx 9$ yrs at $a = 0.25a_0$ [6].

Using the b light curve for KU Cyg in the active state (Fig. 3a), we searched for optimal values of the system's parameters in order to compare our estimates with the previously obtained values. We used the Nelder–Mead method for the optimization of a function [28] to estimate N parameters that can be used to approximate the light curve of KU Cyg.

Figure 3a presents the observations and theoretical light curve of KU Cyg constructed for a model with an elliptical disk around the primary, with the model parameters calculated using the Nelder–Mead method. The points with error bars show the observed brightness of the system in magnitudes. The solid curve represents the theoretical light curve for the following parameters. For the red dwarf, $q = 5.43$ ($Q = 1/q = 0.184$), $i = 86°.5$, and $T_{eff} = 3904$ K, $\mu = 1.0$. For the disk, the eccentricity

(a)

(b)

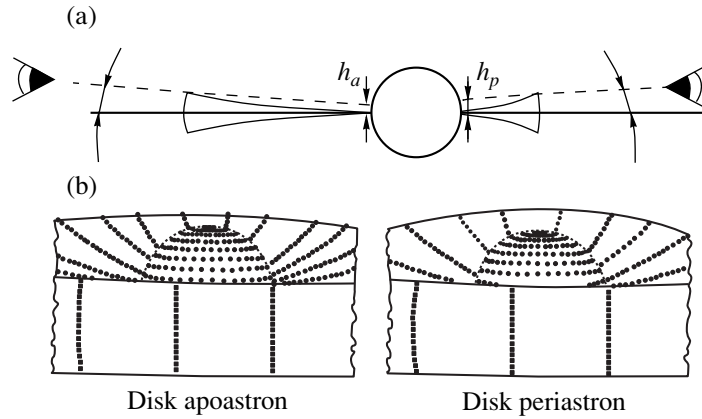Disk apoastron   Disk periastron

Fig. 4. (a) Diagram and (b) elements of the computer simulation illustrating the eclipse conditions for disk areas and the spherical star at the phases for disk apoastron and periastron for an orbital inclination of $i = 86°.5$; h_a and h_p are the heights of the corresponding regions obscured from the observer.

$e = 0.159$, and the apoastron radius $R_d(\text{ap}) = 0.647\xi = 0.431a_0$ (for $q = 5.43$, the distance between the inner Lagrange point and the center of the hot star was $\xi = 0.666a_0$). At periastron, $R_d(\text{per}) = 0.362a_0$, and the semimajor axis of the disk $a = 0.371a_0$. The constant for the paraboloidal fraction of the disk $A = 3.5$. In this case, the height of the outer edge of the disk is $h = 0.058a_0$ (the parameter z/r in units of the semi-major axis is often used instead of $z \equiv 0.5h$; r is the disk radius and, if r is assumed to be equal to the semimajor axis of the elliptical disk a, $z/r = 0.078$). The azimuth of the disk periastron relative to the line connecting the stellar components is $123°$. The temperature in the inner regions of the disk $T_{in} = 18\,440$ K was taken to be equal to the temperature at the surface of the primary

$(T_{in} = T_1)$, and its radius was $R_1 = 0.0637\xi = 0.0424a_0$. The temperature at the edge of the paraboloidal portion of the disk varies from 4500 K at disk periastron to 3600 K at apoastron. The average temperature on the lateral surface of the disk is 3600 K, and the temperature difference between periastron and apoastron does not exceed 20 K. When constructing the theoretical light curve, we included a hot spot near the lateral surface of the disk [12] using a standard hot-spot model. This yielded a hot-spot azimuth ~77°, radius $r_{sp} = 0.155a_0$, and temperature parameter $f_{sp} = 0.423$, which implies that the temperature inside the spot is ~42.3% higher than in the surrounding areas of disk; i.e., $T_{sp} \sim 5100$–5200 K. The table presents a comparison of the parameters we estimated for KU Cyg and those derived pre-

Parameters of KU Cyg

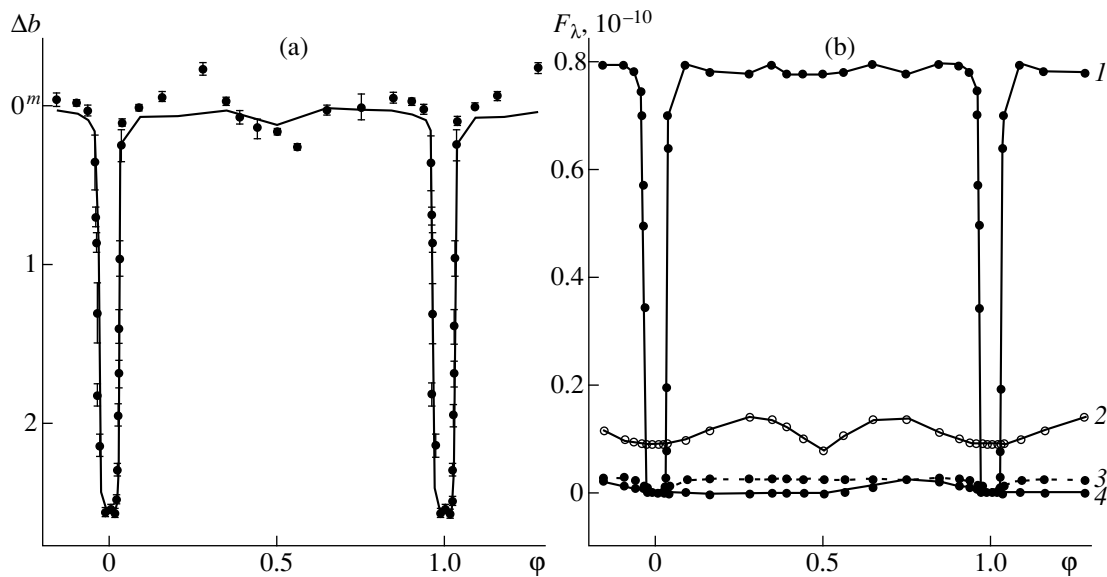| Parameter	Generally accepted values	Close binary system with circular disk	Close binary system with elliptical disk
$Q = M_2/M_1$	0.12–0.18	0.162	0.184
i, deg	82.5–88.0	86.4	86.5
R_1/a_0	0.043–0.047	0.0429	0.0424
R_2/a_0	0.2–0.3	0.245	0.254
T_1, K	7500–13300	12990	18440
T_2 (photometry), K	3651 ± 71 [19]	3966	3904
T_2 (Sp K5 III), K	4000 [29]		
a/a_0	~0.3–0.49	0.321	0.371
e	0–0.38	0	0.159
z/r	0.05–0.10	0.064	0.078
α_e, deg	157 ± 4	–	122.7
φ_{spot}, deg	–	81	77
R_{spot}/a_0	–	0.131	0.155
T_{spot}, K	–	4710	5150
χ^2	–	1328	934

Fig. 5. Same as Fig. 3 for a model with a circular disk around a spherical star. The parameters for the theoretical curve are given in the table.

viously in other studies. Figure 3b presents the contribution of each of the system's components (primary and secondary stars, disk, and hot spot) to the total flux from the system in arbitrary units (F_λ) as a function of orbital phase. The flux can be converted to physical units using the relation $f_\lambda = F_\lambda a_0^2 \times 10^{-12}$ erg s^{-1} cm^{-3}, where a_0 is the distance between the stars in centimeters and F_λ is the flux presented in Fig. 3b. Note the presence of a local minimum in curve *1* (the contribution of the primary) near orbital phases for which the disk periastron (whose position is marked by the vertical arrow) falls in the line of sight (we will call this orbital phase the "periastron phase" and the corresponding phase for the disk apoastron the "apoastron phase"). This minimum is due to the fact that, when we observe the disk from the periastron side, its outer edge obscures some fraction of the primary surface, whereas these areas remain unobscured for an observer viewing from the side of disk apoastron (see the diagram in Fig. 4).

Curve *2* in Fig. 3b presents the flux from the red star as a function of orbital phase. The shape of the curve is essentially due to the effect of reflection superimposed on the effect of partial eclipse of the star by the disk at orbital phases $\varphi \sim 0.4$–0.6. The elliptical shape of the disk results in asymmetry of the secondary minimum of the light curve.

Curve *3*, which represents the flux from the disk, is also asymmetrical: there is a flux maximum at phases $\varphi \sim 0.1$, and a minimum at phase $\varphi \sim 0.75$. The main reason for the decrease of the disk flux when the disk is observed from the side of periastron is that, at these orbital phases, areas of the disk near apoastron, which are more distant from the primary and cooler, are viewed at large angles ($\cos\gamma \sim 0$). In addition, in accor-

dance with the diagram in Fig. 4, at the periastron phase, the edge of the disk obscures a larger number of hot area elements near the primary than it does at the apoastron phase. Conversely, at these orbital phases, an observer viewing from the apoastron side views areas of the disk that are hotter and closer to the primary at small angles ($\cos\gamma \sim 1$). An additional contribution is made by the variation of the apparent size of the disk with orbital phase. The maximum projected area of the disk occurs at phases $\pm 90°$ from the periastron phase, while the minimum projected area occurs at the periastron and apoastron phases. The superposition of these two effects results in a small displacement of the maximum in the disk radiation from the apoastron phase.

The theoretical *b* light curve presented in Fig. 3a reproduces the secondary minimum ($\varphi \sim 0.4$–0.8) considerably better than the light curve based on the Wilson–Devinney model presented in [18], although, according to a χ^2 criterion (Table), our model likewise does not provide a completely adequate description of the observations. It is possible that we will obtain better agreement between the observations and theoretical model if we replace the "hot spot" on the lateral surface of the disk with an extended hot formation beyond the disk—a shock wave located along the edge of a stream of matter flowing into the accretion disk [9–11] (Matsuda *et al.* [30] call such structures "hot lines"). We will consider a "hot line" model in another study.

Figure 5a presents the theoretical *b* light curve for KU Cyg calculated for the standard model for cataclysmic variable with circular disks described in [13]. As for the elliptical-disk model, we used a Nelder–Mead method [28] to determine the best fit of the parameters to the observations. The resulting parameters for KU Cyg are presented in the table. We can see that both qualita-
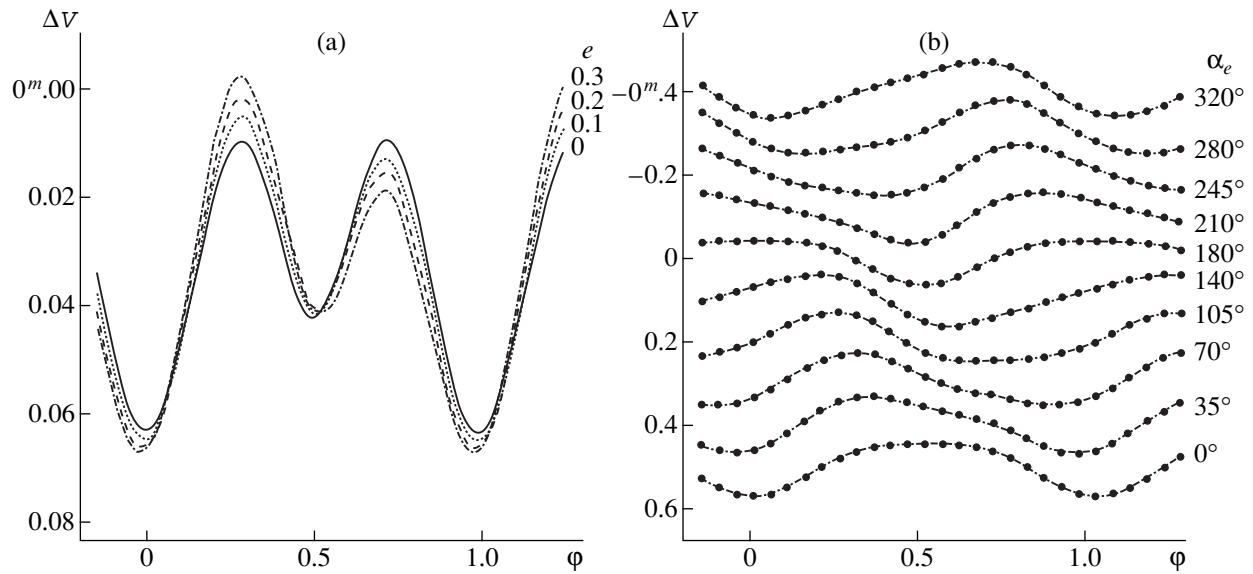
Fig. 6. (a) Theoretical V light curves calculated for an elliptical-disk model for disk eccentricities $e = 0.0$ (solid), 0.1 (dotted), 0.2 (dashed), and 0.3 (dot–dash). The azimuth for the disk periastron is 65°; the model parameters used to construct the curves are given in the text. (b) Light curves calculated for a range of disk periastron azimuths α_e (0°–325°). Model parameters used to construct the curves are given in the text. For convenience in comparison, the curves are shifted relative to each other by the constant value $\Delta m = 0.1$.

tively (Fig. 5a) and quantitatively (according to a χ^2 criterion), the shape of the curve near the secondary minimum is reproduced appreciably worse by the circular-disk model. On the whole, the theoretical curve is similar to those obtained in other studies [18, 19, 23, 25].

Figure 5b shows the contributions to the total flux of all the components of the system: the hot star (*1*), secondary (*2*), circular disk (*3*), and "typical" hot spot (*4*). The main difference from Fig. 3b is that there are no minima in curves *1* and *3*, which occur in the elliptical-disk model due to the different visibility conditions for an area element in the inner regions of the disk and on the hot star. As expected, the shape of the curve representing the flux from the secondary (*2*) is symmetrical, and the flux from the disk (*3*) is constant except at orbital phase $\varphi \sim 0.0$, where there is a partial eclipse of the disk by the red star.

6. MODEL CALCULATIONS

The code is rather sensitive to the value of the disk eccentricity, even for small inclinations of the binary orbit to the line of sight. We calculated model light curves for a system with parameters typical for cataclysmic variables: $q = 1.5$, orbital inclination $i = 30°$, red dwarf completely filling its Roche lobe; temperature averaged over the red-dwarf surface without taking into account heating by the white-dwarf radiation equal to 5000 K (intense heating from the hot component can increase the average temperature of the red dwarf); radius of the disk at periastron equal to $R_d(\text{per}) = 0.5\xi = 0.27a_0$ ($\xi = 0.542a_0$ for $q = 1.5$); and temperature and radius of the white dwarf $T_1 = 25\,000$ K, $R_1 = 0.20\xi =$

$0.0108a_0$. The thickness of the outer edge of the disk h is the same over the entire perimeter; it is determined by the paraboloid constant $A = 2.5$ and, for a fixed disk radius at periastron, depends on the disk eccentricity. For example, for $e = 0.1, 0.2, 0.3$, $h = 0.083a_0, 0.090a_0$, and $0.099a_0$, respectively. The thickness of the outer edge of the disk appreciably affects the shape and amplitude of the light curve only for orbital inclinations close to 90°.

Figure 6a shows model V light curves for disk eccentricities $e = 0.0$ (solid), 0.1 (dotted), 0.2 (dashed), and 0.3 (dot–dash). The azimuth of the disk periastron is 65°. We can see that the light curve for a circular-disk model ($e = 0.0$) is symmetrical; its shape is determined by the ellipsoidal shape of the red dwarf. During the orbital cycle, the contributions of the disk and white dwarf are constant for all the model curves. When the disk eccentricity e increases, the contribution of the disk increases near the apoastron phase due to the increase of the disk's radius at apoastron in accordance

with the relation $R_d(\text{ap}) = R_d(\text{per})\dfrac{1+e}{1-e} = 0.27a_0\dfrac{1+e}{1-e}$.

At sufficiently large disk eccentricities, the disk can be observed to precess. According to the calculations of Whitehurst [1] and Hirose and Osaki [7], precession of the apsidal line occurs in systems with component mass ratios $q > 4$. Figure 6b presents a set of model curves for a close binary system with mass ratio $q = 5.0$, orbital inclination $i = 30°$, disk eccentricity $e = 0.5$, and disk radius at apoastron $R_d(\text{ap}) = 0.5\xi = 0.329a_0$, calculated for several values for the azimuth of the disk periastron α_e (0°–325°). The semimajor axis of the disk for the

parameters used is $a = 0.22a_0$, and the half-thickness of its edge is $h/2 = 0.0323a_0$. The other parameters of the system coincide with those used to construct the model curves in Fig. 6a. For convenience in comparison, the curves are shifted relative to one another by the constant value $\Delta m = 0.1$.

For the system considered, the contribution of the red-dwarf radiation to the total flux for $q = 5$ is, on average, 25–30% lower than the average contribution of the disk. The amplitude of variations due to the ellipsoidal shape of the disk does not exceed $0.^{m}07$, since the main reason for the brightness variability is variations of the disk flux as a function of orbital phase. The light curve displays only one obvious maximum, sometimes of somewhat degraded shape. We can see that the shape of the curve varies with the orientation of the disk relative to the secondary, even when the disk is comparatively small and there is a total absence of eclipses of the components by each other. Even the entirely symmetric curves calculated for $\alpha_e = 0°$ and $180°$ differ. For $\alpha_e \sim 10°$–$170°$, the disk apoastron is visible in the first half of the orbital period ($\varphi \sim 0.25$); the light curve reaches its peak for $\alpha_e \sim 90°$. For $\alpha_e \sim 190°$–$320°$, the light-curve maximum moves into the second half of the orbital period ($\varphi \sim 0.75$). As noted earlier, the variation of the shape of the light curve for different disk orientations is due to the different visibility conditions for areas in its inner regions (Fig. 4). Near the apoastron phase, for small orbital inclinations, the disk flux increases due to the fact that the hottest areas of the disk, located at its periastron, are viewed at smaller angles. Conversely, near the periastron phase, the hot areas of the disk at periastron are viewed at large angles.

7. CONCLUSIONS

Dynamical calculations of matter flows in close binary systems provide conclusive evidence that the accretion disks that form around the compact stars in these systems are noncircular in shape. Observations of SU UMa variables lead to the same conclusion. In such systems, using a standard model with an axisymmetric disk around the white dwarf to synthesize the system's light curve results in poor agreement with the observations. The binary parameters for which photometric observations can be described reasonably well by the theoretical light curve differ from those implied by spectral observations of the system.

Using a model in which the compact star in a close binary system is surrounded by an elliptical disk makes it possible to obtain agreement between the parameters derived from spectral and photometric observations. Our photometric light curve analysis for the variable KU Cyg using a model with an elliptical accretion disk around a spherical star yields values for q, i, a, R_w that are in good agreement with those derived from spectral observations. In particular, we were able to obtain a good fit to the secondary minimum in the light curve of KU Cyg. Attempts to describe the shape and amplitude of this minimum using other models have failed.

REFERENCES

1. R. Whitehurst, Mon. Not. R. Astron. Soc. **232**, 35 (1988).

2. D. Syer and C. J. Clarke, Mon. Not. R. Astron. Soc. **255**, 92 (1992).

3. D. Syer and C. J. Clarke, Mon. Not. R. Astron. Soc. **260**, 463 (1993).

4. Yu. E. Lubarskij, K. A. Postnov, and M. E. Prokhorov, Mon. Not. R. Astron. Soc. **266**, 583 (1994).

5. N. Vogt, Astrophys. J. **252**, 653 (1982).

6. Y. Osaki, Astron. Astrophys. **144**, 369 (1985).

7. M. Hirose and Y. Osaki, Publ. Astron. Soc. Jpn. **42**, 135 (1990).

8. Y. Osaki, Publ. Astron. Soc. Jpn. **41**, 1005 (1989).

9. D. V. Bisikalo, A. A. Boyarchuk, O. A. Kuznetsov, and V. M. Chechetkin, Astron. Zh. **74**, 880 (1997) [Astron. Rep. **41**, 786 (1997)].

10. D. V. Bisikalo, A. A. Boyarchuk, O. A. Kuznetsov, and V. M. Chechetkin, Astron. Zh. **74**, 889 (1997) [Astron. Rep. **41**, 794 (1997)].

11. D. V. Bisikalo, A. A. Boyarchuk, V. M. Chechetkin, *et al.*, Mon. Not. R. Astron. Soc. **300**, 39 (1998).

12. T. S. Khruzina, Astron. Zh. **68**, 1211 (1991) [Sov. Astron. **35**, 607 (1991)].

13. T. S. Khruzina, Astron. Zh. **75**, 209 (1998) [Astron. Rep. **42**, 180 (1998)].

14. N. I. Shakura and R. A. Sunyaev, Astron. Astrophys. **24**, 337 (1973).

15. G. Djurasevic, Astrophys. Space Sci. **240**, 317 (1996).

16. I. B. Voloshina and T. S. Khruzina, Astron. Zh. **77**, 109 (2000) [Astron. Rep. **44**, 89 (2000)].

17. N. I. Balog, A. V. Goncharskiĭ, Z. Yu. Metlitskaya, and A. M. Cherepashchuk, Perem. Zvezdy **21**, 695 (1982).

18. E. C. Olson, P. B. Etzel, and M. R. Dewey, Astron. J. **110**, 2378 (1995).

19. J. I. Smak, Acta Astron. **47**, 345 (1997).

20. Y. Osaki, in *Cataclysmic Variables and Related Objects*, Ed. by A. Evans and J. H. Wood (Kluwer, Dordrecht, 1995), p. 127.

21. D. N. Popper, Publ. Astron. Soc. Pac. **60**, 248 (1948).

22. D. N. Popper, Astrophys. J. **139**, 143 (1964).

23. E. C. Olson, Astron. J. **96**, 1439 (1988).

24. E. C. Olson, Astron. J. **102**, 1423 (1991).

25. S. Zola, Acta Astron. **42**, 355 (1992).

26. E. C. Olson, in *Algols,* Ed. by A. H. Batten (Kluwer, Dordrecht, 1989), p. 23.

27. A. R. King, in *The Evolution of X-ray Binaries*, Ed. by S. S. Holt (AIP Conf. Series, 1994), Vol. 308, p. 515.

28. D. M. Himmelblau, *Applied Nonlinear Programming* (McGraw-Hill, New York, 1972; Mir, Moscow, 1975).

29. G. M. H. J. Habets and J. R. W. Heintze, Astron. Astrophys., Suppl. Ser. **46**, 193 (1981).

30. T. Matsuda, M. Makita, and H. M. J. Boffin, in *Disk Instabilities in Close Binary Systems*, Ed. by S. Mineshige and J.C. Wheeler (Universal Acad., Tokyo, 1999), p. 129.

Translated by K. Maslennikov

Multicolor Photometry of CH Cygni in 1978–1998

O. G. Taranova and V. I. Shenavrin

Sternberg Astronomical Institute, Universitetskiĭ pr. 13, Moscow, 119899 Russia

Received June 21, 1999

Abstract—We present the results of long-term (1978–1998) infrared and optical observations of the unique symbiotic system CH Cygni. The system's IR brightness and color variations are generally consistent with a model in which the source is surrounded by a dust envelope with variable optical depth. There was evidence for a hot source in the CH Cyg system during the entire period from 1978 to 1998, with the exception of several hundred days in 1987–1989. Over the observation period, there was tendency for the system to gradually redden at 0.36–5 μm, accompanied by a brightness decrease at 0.36–2.2 μm and a brightness increase at 3.5 and 5 μm. The "activation" of the cool sources in 1986–1989 nearly coincided with the disappearance of radiation from the hot source. The dust envelope of CH Cyg is not spherically symmetrical, and its optical depth along the line of sight is substantially lower than its emission coefficient, the mean values being $\tau_{ex}(L) \sim 0.06$ and $\tau_{em}(L) \sim 0.16$. We confirm the presence of a 1800- to 2000-day period in both the optical and IR, both accounting for, and not accounting for, a linear trend. The spectral type of the cool star varied between M5III and M7III. The spectral type was M5III during the phase of maximum activity of the system's hot source, while the spectral type was M7III when the star's optical radiation was almost completely absent. The luminosity of the cool giant varied from (6300–9100) $L_{\odot}$; its radius varied by approximately 30%. The ratio of the luminosities of the dust envelope and the cool giant varied from 0.08 to 0.5; i.e., up to 50% of the cool star's radiation could be absorbed in the envelope. The temperature of dust particles in the emitting envelope varied from 550 to 750 K; the radius of the envelope varied by more than a factor of 2. The expansion of the emitting dust envelope observed in 1979–1988 accelerated: its initial velocity (in 1979) was ~8 km/s, while the maximum velocity (in 1987–1989) was ~180 km/s. Beginning in 1988, the radiation radius of the dust envelope began to decrease, first at ~45 km/s and then (in 1996–1998) at ~3 km/s. From 1979 until 1996, the mass of the emitting dust envelope increased by approximately a factor of 27 (the masses in 1979 and 1988 were ~1.4×10^{-7} $M_{\odot}$ and ~3.8×10^{-6} $M_{\odot}$, respectively), after which (by 1999) it decreased by nearly a factor of 7. The mass-loss rate of the cool star increased in 1979–1989, reaching ~3.5×10^{-6} $M_{\odot}$/yr in 1988. Subsequently (up to the summer of 1999), the envelope itself began to lose mass at a rate exceeding that of the cool star. The largest input of matter to the envelope occurred after the phase of optical activity in 1978–1985. If the envelope's gas-to-dust ratio is ~100, the mass of matter ejected in 1988 was ~4×10^{-4} $M_{\odot}$. © 2000 MAIK "Nauka/Interperiodica".

1. INTRODUCTION

In early 1975, we included CH Cyg in our studies of circumstellar dust envelopes. Irregular infrared observations from 1969 to 1972 [1–4] had provided evidence for the presence of a dust envelope around CH Cyg, since they showed excess radiation at $\lambda > 3$ μm. Our spectroscopic (0.6–1.1 μm) observations and *UBVRJHKL* photometry of CH Cyg in the summer of 1975 confirmed the star's classification as a semiregular red giant with a spectral type close to M6 [5]. Comparison of our observations with those cited above did not indicate variations of the star's IR brightness within the photometric errors; for this reason, we stopped observing the star and resumed our observations only about three years later, when its *V* brightness had increased by 1–1.5^m and the beginning of the star's optical activity had become evident. Since the summer of 1978, we have been carrying out IR and optical photometry of CH Cyg as regularly as possible. Initial analyses of our observations have been published in [6–15].

Several hundred papers have been published on CH Cyg (see, for instance, the bibliography in [16]). The object's enigmatic nature has gradually become clearer after many years of diverse observations. The system is now known to be a symbiotic star, with the corresponding characteristic components (a late giant and white dwarf that accretes matter flowing from the cool star). Until recently, the orbital period of the symbiotic system was believed to be about 5300 days, based on estimates by Yamashita and Maehara [17]. In their recent paper, Hinkle *et al.* [18] conclude, based on their analysis of 13 years of high-resolution spectroscopic observations near 2 μm, that the system is triple: the symbiotic pair has a short orbital period (about 756 days) and the third component, a yellow dwarf, orbits the symbiotic pair with a period of about 14.5 years. Through their analysis of UV and optical spectroscopic and photometric observations, Skopal *et al.* [19] confirmed that the system is triple and found that the symbiotic pair eclipses.

Photometric data obtained over a wide spectral range indicate that CH Cyg contains at least three variable sources:

(a) A hot source, with its contribution to the radiation at $\lambda > 1$ µm not exceeding several percent (in flux), even during the period of optical activity in 1978–1985, when the star's U brightness increased by almost 6^m;

(b) A cool star (or stars);

(c) A circumstellar dust envelope.

The variability of the hot source, whose nature remains unclear, is mainly due to flare activity. Analysis of our spectroscopic and photometric observations of CH Cyg obtained in 1978–1989 [9, 10] suggested that the cool component of the symbiotic system was a late (M5–M7), semiregular-variable giant. However, based on the brightness variability amplitudes at different wavelengths after 1989, it is formally possible to classify red star of the system as a Mira-type star (for example, $\Delta V \geq 2^m$ when V–J exceeds 6^m; cf. the tables in [6–15]). We first detected the presence of a relatively hot circumstellar dust envelope in 1985 [8] at the end of an optical outburst, and our recent observations show that it had not dissipated by May 1999. The dust envelope's variability is primarily due to changes in its optical depth.

In the present study, we primarily analyze our IR photometric data for CH Cyg obtained in 1995–1998. In addition, we use our collected observations to revise and improve our earlier conclusions about the system and its individual components.

2. OBSERVATIONS

The IR and optical photometry of CH Cyg (along with other objects) was carried out with the 125-cm (IR) and 60-cm (optical) telescopes of the Sternberg Astronomical Institute's Crimean Station. We especially emphasize that our *JHKLM* photometry of CH Cyg in 1986–1997 forms a uniform series with constant instrumental errors. This uniformity is due to the fact that, since April 1986, our IR observations have been conducted using an InSb photometer [20], whereas three photometers with different detectors were used for our *JNK*, *L* and *M* photometric observations prior to 1986 [21]. Starting in 1986, the optical observations were obtained using V.M. Lyutyĭ's *UBV* photometer. The errors in our photometric observations of CH Cyg do not exceed 0.01–0.05^m in all filters. Note that a 0^m05 error in *J* translates into errors of less than 50 K when estimating the blackbody temperature of the source (for blackbody temperatures from 2200 to 3500 K) and into errors of less than 5% when estimating its radius. If we attribute the *J* brightness variations within 0^m05 solely to changes in the optical depth of the circumstellar dust envelope (whose constituents resemble interstellar dust particles), the corresponding uncertainty in $E(B - V)$ will not exceed 0^m07. Descriptions of our observing techniques

and the instrumental parameters, as well as the observational data for 1978–1995, are given in [6–15].

Table 1 presents the results of our *JHKLM* and *V* photometry of CH Cyg for 1995–1998.* Figures 1 and 2 show the results of our observations in the form of light and color curves for the entire period covered. The horizontal dashed lines in Fig. 2 correspond to the color indices of a normal M6 giant. The meaning of the other lines in Figs. 1 and 2 is explained below.

3. ANALYSIS OF OBSERVATIONAL DATA
3.1. CH Cyg after 1994

Our 1995 paper [14] presents an analysis of our *JHKLM* and *UBV* photometry carried out prior to 1995. After 1994, the system's radiation continued to exhibit nonstationary features associated with both the cool and hot sources. In the optical and IR photometric observations of CH Cyg, the appearance of radiation from the hot source adding to the radiation of the red giant will, first and foremost, influence U–B, which is 1–2^m for normal late-type stars. Lower U–B values, less than 1^m, can be considered evidence for the presence of radiation from the hot source in the overall radiation of CH Cyg. Using this criterion and examining Fig. 2, which shows variations in the star's U–B and U brightness in 1978–1998, we find that traces of the hot source were continuously observed in the system's radiation in 1995–1998. U–B varied from -0^m4 to $+0^m8$ (approximately at the same level as in 1986), while the U brightness reached almost a low record.

A second period of optical activity of the system began in mid-1990 [14], when the system's brightness was low (as opposed to the first active phase of 1978–1985). By 1995, this had become an "active–passive" phase. Figure 2 indicates that U–B increased (the star became redder) until mid-1995, when it began to decrease (the star became bluer), reaching a local minimum in August 1996. In 1997, the star became redder again, then bluer in late 1997–early 1998. Similar changes were observed in 1995–1997 for B–V and V–J, but their absolute values appreciably exceeded those for normal late-type stars. The variations in V–J in 1978–1998 are shown in Fig. 2.

The "active–passive" state of the system's hot sources was accompanied by extreme reddening of its cool sources; the observed IR color indices reached their maximum values in 1995–1996, as is obvious from Table 1 and Fig. 2. By the end of 1997 and in 1998, the cool sources also began to become bluer, accompanied by a brightening in the *JHK* filters and constant or slightly weakening *LM* brightness.

The data of Table 1 and Figs. 1 and 2 show that *an absolute minimum of the BV brightness* for the entire history of observations of CH Cyg occurred in 1995–

---

*IR photometric data obtained in 1999 during the preparation of this paper (JD 2451299 and later) have been added to Table 1.

Table 1. Results of *JHKLM* and *V* photometry of CH Cyg in 1995–1998

JD 2440000+	J	H	K	L	M	V	JD 2440000+	J	H	K	L	M	V
9858	1.72	0.47	−0.29	−1.53	−1.65	8.7	10704	1.11	−0.04	−0.62	−1.52	−1.64	8.3
9880	1.63	0.37	−0.34	−1.49	−1.67	8.6	10713	1.15	−0.01	−0.59	−1.45	−1.49	−
9885	1.6	0.36	−0.38	−1.53	−1.67	8.6	10714	1.11	−0.08	−0.62	−1.49	−1.53	8.6
9937	1.55	0.35	−0.39	−1.6	−1.84	8.69	10753	1.17	−0.02	−0.58	−1.46	−1.47	−
9939	1.52	0.33	−0.4	−1.57	−1.74	8.69	10764	1.13	−0.02	−0.6	−1.49	−1.72	−
9944	1.58	0.37	−0.35	−1.5	−1.77	8.67	10777	1.18	0.02	−0.55	−1.46	−1.66	−
9969	1.57	0.32	−0.4	−1.60	−1.82	−	10867	1.15	0	−0.57	−1.41	−1.5	−
9970	1.58	0.34	−0.36	−1.6	−1.72	8.88	10910	1.16	0.02	−0.55	−1.35	−1.4	−
9973	1.61	0.38	−0.31	−1.56	−1.73	8.88	10918	1.13	−0.03	−0.56	−1.42	−1.41	−
9975	1.56	0.34	−0.39	−1.56	−1.78	−	10942	1.07	−0.08	−0.53	−1.48	−1.5	8.69
9976	1.56	0.34	−0.39	−1.55	−1.81	8.87	10975	1.05	−0.08	−0.63	−1.46	−1.4	8.54
10061	1.52	0.32	−0.39	−1.53	−1.75	8.89	10980	1.08	−0.02	−0.54	−1.37	−1.52	−
10200	1.5	0.3	−0.32	−1.52	−1.72	9.43	11006	1.02	−0.05	−0.57	−1.43	−1.47	8.00
10233	1.56	0.37	−0.32	−1.49	−1.76	9.64	11033	0.98	−0.09	−0.65	−1.46	−1.57	7.71
10242	1.62	0.43	−0.3	−1.45	−1.65	9.77	11059	1.04	−0.04	−0.59	−1.4	−1.45	−
10258	1.66	0.46	−0.24	−1.49	−1.67	10	11068	1.05	−0.02	−0.56	−1.36	−1.5	7.70
10264	1.7	−	−0.27	−	−	10.05	11095	1.07	−0.04	−0.52	−1.42	−1.45	−
10272	1.75	0.5	−0.27	−1.5	−1.69	10.04	11124	1.07	−0.09	−0.62	−1.39	−1.55	−
10295	1.74	0.5	−	−	−	9.9	11164	0.85	−0.23	−0.72	−1.53	−1.55	−
10303	1.74	0.52	−0.26	−1.5	−1.69	9.9	11174	0.84	−0.24	−0.71	−1.46	−1.41	−
10357	1.73	0.53	−0.22	−1.42	−1.55	−	11180	0.8	−0.26	−0.73	−1.5	−1.44	−
10359	1.7	0.44	−0.24	−1.54	−1.69	9.91	11299	0.74	−0.22	−0.76	−1.38	−1.48	−
10360	1.7	0.36	−0.26	−1.6	−1.71	−	11336	0.76	−0.24	−0.75	−1.45	−1.32	−
10402	1.64	0.29	−0.35	−1.46	−1.65	−	11351	0.79	−0.29	−0.76	−1.51	−1.37	−
10404	1.56	0.29	−0.4	−1.52	−1.7	−	11358	0.78	−0.28	−0.79	−1.49	−1.40	−
10559	1.34	0.08	−0.51	−1.45	−1.54	−	11366	0.79	−0.25	−0.74	−1.52	−1.41	−
10565	1.26	0.09	−0.5	−1.46	−1.57	−	11383	0.82	−0.26	−0.72	−1.47	−1.38	−
10615	1.24	−0.03	−0.54	−1.46	−1.53	8.9	11387	0.82	−0.23	−0.67	−1.49	−1.44	−
10623	1.19	0	−0.57	−1.46	−1.52	8.8	11420	0.82	−0.24	−0.73	−1.48	−1.34	−
10648	1.16	−0.05	−0.59	−1.49	−1.54	8.6	11448	0.77	−0.28	−0.77	−1.51	−1.38	−
10675	1.14	−0.05	−0.61	−1.5	−	8.5	11452	0.73	−0.32	−0.79	−1.51	−1.45	−
10677	1.15	−0.06	−0.61	−1.46	−1.44	−	11456	0.72	−0.27	−0.76	−1.52	−1.48	−
10698	1.19	−0.05	−0.59	−1.46	−1.54	8.6							

1996. According to our observations, this dimming in *BV* took place from mid-June to mid-October 1996. Simultaneously, a record low of the *JHK* brightness and the reddest state of the cool sources were observed for the system. In 1995–1998, variations of the IR brightness were about $0\overset{m}{.}9$ in *J* and about $0\overset{m}{.}2$ in *L*. From mid-1996 until the end of 1998, there was a tendency for decreasing IR color indices and increasing IR brightness. The time scale for the *JHK* brightness vari-

ations in 1995–1998 was ~350–400 days, as for the optical brightness variations.

Thus, the variations of the optical and IR radiation of CH Cyg in 1995–1998 are generally consistent with a model in which the source is surrounded by a dust envelope with variable optical depth. Inside the envelope, there can exist more transparent regions or condensations with typical sizes of the order of the projected radius of the cool star on the dust envelope. We proposed a similar model [11, 14] in connection with
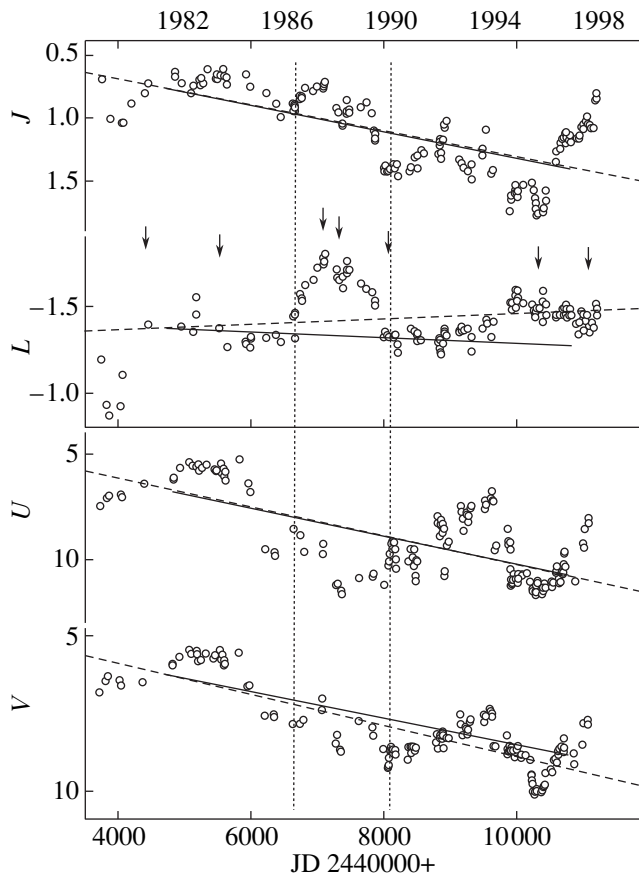
Fig. 1. *JL* and *UV* brightness variations for CH Cyg in 1975–1998. Open circles are our observations. The dashed vertical lines delineate the epoch of activity of the cool sources. The slanted dashed lines are regression fits to the data. The solid lines represent light variations for normal extinction in the dust envelope.
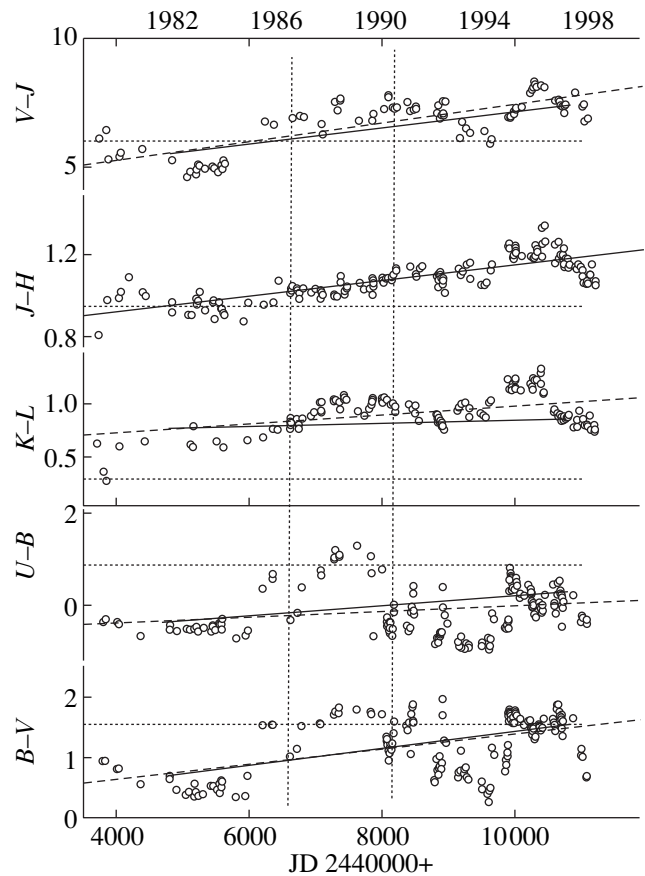
Fig. 2. Color index variations of CH Cyg in 1975–1998. The dashed horizontal lines correspond to the color indices of a normal M6 giant; the remaining lines are explained in the caption to Fig. 1.

estimations of the parameters of the cool radiation sources in the system.

3.2. Characteristic Brightness and Color Variations of CH Cyg in 1978–1998

Let us return to Figs. 1 and 2 and consider the most characteristic features in the brightness and color variations of CH Cyg over the more than two decades of our observations. As stated above, an absolute *BV* brightness minimum of the star was observed in 1996 (JD 2450233–2450403) but this dimming was not accompanied by comparable optical reddening. The *U–B* and *B–V* color indices show that the strongest optical reddening of the system was observed over a period of several hundred days in 1988–1989 (JD 2447250–2447900). The strongest reddening in *V–J* was in 1996 (JD 2450200–2450403). Applying our criterion for the presence of the hot source, the behavior of *U–B* in Fig. 2 indicates that radiation from the hot source was *continuously* present in the optical radiation of CH Cyg in 1978–1998. One exception is a period of several hundred days in 1987–

1989 when only the cool source was detected. The duration of the period in which only the cool source was visible increased with wavelength; for example, it was about 550 days for *U–B* and more than 3000 days for *V–J* (during this period, the color indices exceeded those for a normal M6 giant). This can be explained if the fraction of the hot source's light in the total radiation of the system decreases with increasing wavelength.

The hot source was bluest in 1992–1994 (JD 2448782–2449609) [14]. For equal values of *U–B*, the differences in *V* brightness reached 3^m (e.g., on JD 2445514 and JD 2449880). As a rule, *V–J* exceeded the values typical of normal cool stars (Fig. 2). Exceptions are the phase of optical activity in 1978–1985 and individual dates during the optical activity of 1992–1994.

The maximum *JHK* brightness (JD 2444412–2445949) coincided with the time of optical activity in 1978–1985. During the same period, *J–H* and *H–K* had minimum values (closest to those for normal cool stars). Before 1985, our *L* and *M* observations were not regular; nevertheless, estimates of the *L* and *M* bright-

nesses of CH Cyg for 1980–1984 show that there was also a local maximum in these filters. *K–L* and *L–M* were systematically higher than their values for normal stars, except on several dates in 1978 when the *K–L* values were close to those for a normal M6 giant.

Variations of the *JHK* brightness of up to several tenths of a magnitude occurred against the background of a monotonic decrease in the *JHK* brightness, with the amplitude of the variations decreasing with increasing wavelength (Figs. 1, 2). In other words, there was a systematic dimming and reddening of CH Cyg in the near IR from 1978 until 1999. The same is true of the optical brightness. There was no monotonic brightness decrease in the *L* and *M* filters (3.5 and 5 μm) in 1978–1998 (rather, the opposite). The maximum *L* and *M* brightnesses occurred in 1986–1989; another, less pronounced, maximum was observed in 1995–1996. The vertical dashed lines in Figs. 1 and 2 outline the interval when there was no radiation from the system's hot source and increased activity of the cool sources, reflected as a sudden increase in the IR brightness accompanied by reddening in both the IR and optical. The first attempt to interpret the behavior of the system in this interval was made in [11].

Summarizing the above information:

(1) During 1978–1998, features indicative of radiation from the hot source in CH Cyg were continuously observed, with the exception of several hundred days in 1987–1989.

(2) At 0.36–5 μm, systematic reddening was observed in 1978–1998, accompanied by a brightness decrease at 0.36–2.2 μm and a brightness increase at 3.5 and 5 μm.

(3) The increase in activity of the cool sources in 1986–1989 nearly coincided with the disappearance of the hot-source radiation.

3.3. Optical Properties of the Dust Particles

Analysis of the observations obtained after 1990 confirms our earlier conclusion [10] that the *J* and *H* emission is solely due to the cool component and the observed variations of the *JH* brightness and of *J–H* could be due to either changes in its parameters (temperature and radius) or variations of the optical depth of the dust envelope. Calculations show that, for reasonable dust-particle temperatures (<1200 K), the contribution of emission from the dust envelope to *J* and *H* (and, to some extent, *K*) does not exceed a fraction of a percent of the red star's radiation. Thus, in *J* and *H* (1.25–1.65 μm), the dust envelope will be manifest only as a decrease in the *JH* brightness and a reddening of the cool component.

In addition, assuming the dust particles have temperatures of ~600–700 K, we estimated the radius of the dust envelope heated by the cool component to be $(5–8) \times 10^{14}$ cm [8, 11]. For an orbital period of

~5290 days [17] and a combined mass of the components of $\leq 10\,M_\odot$, the distance between the components does not exceed 2×10^{14} cm if the orbit is circular. In other words, the system's stellar components are located inside the dust envelope, so that changes in its optical depth will lead to spectral brightness variations of the system as a whole, in accordance with the optical properties of the dust particles.

If we attribute the systematic decrease in the optical and *JHK* brightness of CH Cyg in 1978–1998 (Figs. 1 and 2) to a monotonic increase in the dust envelope's optical depth, we can use a linear approximation of our observations in the form

$$Y = a + bX \tag{1}$$

to estimate the parameter *b* for observations in various filters, where *Y* is the observed magnitude and *X* is the time scale for the observations. It is evident that the wavelength dependence of *b* should reflect the extinction law for the dust particles in the envelope. We analyzed this dependence by comparing the observed $\Delta Y/\Delta H = b(\lambda)/b(H)$ values with the normal interstellar extinction law.

Extinction in a dust envelope consisting of dust particles with optical properties close to those of interstellar dust particles will correspond to the normal law [22]:

$$\begin{aligned} &A(U)/A(B)/A(V)/A(J)/A(H)/A(K)/A(L)/A(M) \\ &= 4.78/4.05/3.05/0.75/0.46/0.27/0.14/0.08 \end{aligned} \tag{2}$$

and

$$A(\lambda)/A(H) = c(\lambda)/0.46, \tag{3}$$

where *A* (filter) is the normal extinction of the star's light by the dust envelope in the corresponding filter and $c(\lambda)$ are coefficients describing the normal interstellar extinction law [given on the right-hand side of (2)].

We calculated regression lines using (1) for our 1978–1997 observations, shown as dashed lines in Figs. 1 and 2. We present the relation between $\log[A(\lambda)/A(H)]$ and $\log[b(\lambda)/b(H)]$ in Fig. 3, which shows that these values are almost directly proportional to each other (see numerical data in Fig. 3). In other words, using the normal extinction law for the dust envelope in model calculations of the characteristics of the star + dust envelope system based on photometric observations of CH Cyg should not adversely affect our estimates of the parameters for the stellar and dust components.

Based on this conclusion and assuming that variations of *J–H* are primarily due to changes in the dust envelope's optical depth along the line of sight, we can

use Eq. (2) to estimate the expected linear trend for any of the observed magnitudes, namely,

$$\Delta U = 16.48\Delta(J-H), \quad \Delta V = 10.52\Delta(J-H),$$
$$\Delta J = 2.59\Delta(J-H), \quad \Delta L = 0.48\Delta(J-H),$$
$$\Delta(U-B) = 2.52\Delta(J-H),$$
$$\Delta(B-V) = 3.44\Delta(J-H),$$
$$\Delta(V-J) = 7.93\Delta(J-H),$$
$$\Delta(K-L) = 0.45\Delta(J-H).$$

(4)

In Figs. 1 and 2, the solid slanted lines show the expected trends for the corresponding magnitudes in 1978–1997; these lines are close to the regression lines at 0.36–2.2 μm. At 3.5 and 5 μm, in addition to extinction in the dust envelope, which is small at these wavelengths, emission from the dust envelope itself is appreciable.

The similarity of the dust particles in the envelope of CH Cyg to interstellar dust particles is confirmed by the dependences of the system's brightness variations in various filters on variations of $J–H$. Figure 4 displays the observed variations of the JKL brightness as functions of the $J–H$ variations. The regression fits are plotted as dashed lines, and relations based on Eqs. (2) and (3) are plotted as solid lines. We can see that, here also, the data for the J and K brightnesses nearly coincide with the plotted lines, whereas the emission of the envelope itself leads to appreciable discrepancies in the L filter. The crosses in Fig. 4 mark observations taken during the enhanced activity of the cool sources (dashed vertical lines in Figs. 1 and 2).

3.4. Spectral Energy Distribution of CH Cyg

Several distinctive intervals stand out in the light and color curves of CH Cyg (Figs. 1, 2), associated with the radiation of the system's various components, which radiate most efficiently in different parts of the spectrum. We can see from Figs. 1 and 2 that a maximum in $UBVJH$ was observed during the phase of optical activity in 1978–1985 (near JD 2445520) and a minimum in July 1996. An optical minimum was observed in May 1988, a maximum in LM in September 1987, and a minimum in 1978. Note that our 1978 data were taken at the beginning of our observing program and could be slightly inaccurate. Table 2 contains our optical and IR photometric data for CH Cyg averaged over six time intervals, where se(mag) are the standard errors in magnitudes and N is the number of nights included in the average. The open circles in Fig. 5 show the mean observed energy distributions for the intervals we consider most characteristic of CH Cyg in 1978–1998 (curves 2–6, with their numbers corresponding to the interval numbers from Table 2). The upper energy distribution (Fig. 5, curve 1) corresponds to the beginning of our observations. The middle points of these time series are marked with arrows in Fig. 1. The verti-
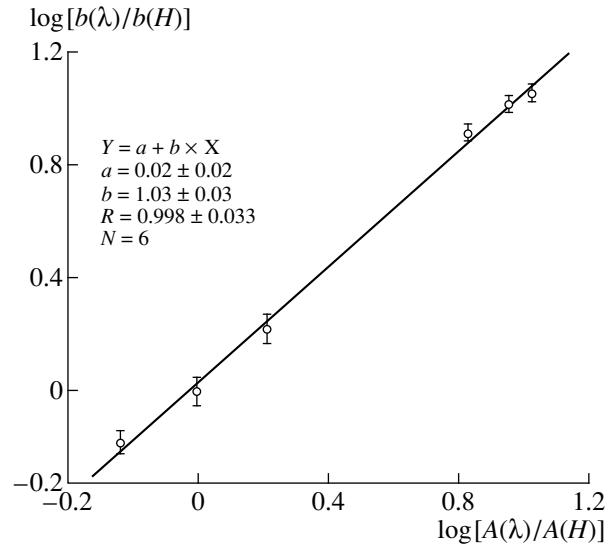

Fig. 3. Comparison between the observed $\log[\,b(\lambda)/b(H)\,]$ values and the law for normal interstellar extinction (see text).
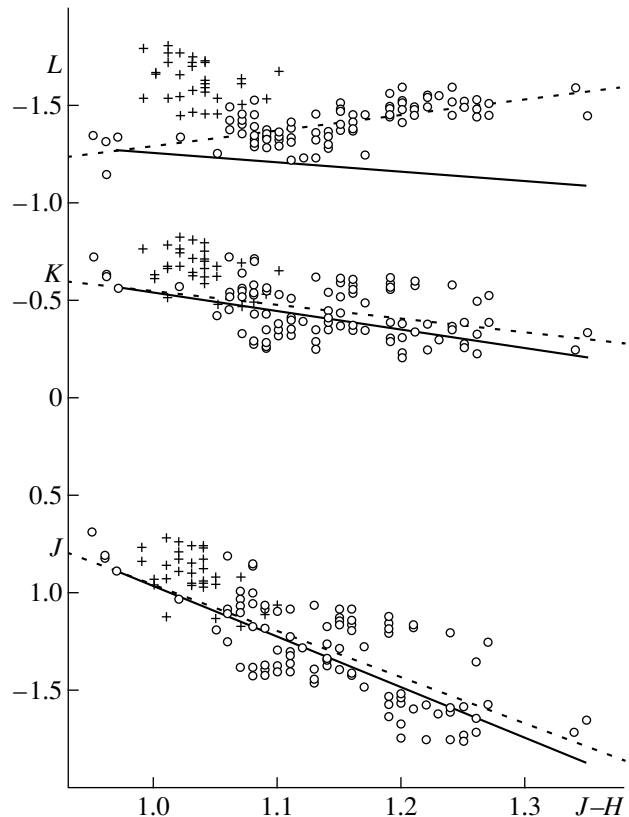

Fig. 4. Brightness–color diagram from the 1978–1998 observations of CH Cyg. Variations of the JKL brightness are plotted against variations in $J–H$. The dashed lines are regression fits; the solid lines show the normal extinction law; the crosses correspond to observations during activity of the cool source.

Table 2. Averaged optical and IR photometric data for CH Cyg for six observation intervals

JD 2445460–JD 2445580 (interval 2)				JD 2447048–JD 2447065 (interval 3)			
λ, μm	mag	se(mag)	N	mag	se(mag)	N
0.36	5.82	0.08	9	9.46	0.17	2
0.45	6.25	0.07	9	8.75	0.13	2
0.55	5.72	0.05	9	7.19	0.13	2
1.25	0.67	0.01	8	0.74	0.01	4
1.65	−0.27	0.02	8	−0.27	0.02	4
2.2	−0.72	0.01	10	−0.80	0.01	4
3.5	−1.32	0.04	2	−1.78	0.01	4
5	−1.45	0.01	2	−1.92	0.02	4

JD 2447265–JD 2447343 (interval 4)				JD 2448010–JD 2448150 (interval 5)			
λ, μm	mag	se(mag)	N	mag	se(mag)	N
0.36	11.31	0.09	5	9.76	0.15	14
0.45	10.23	0.10	5	10.07	0.08	14
0.55	8.49	0.09	5	8.80	0.05	14
1.25	0.99	0.03	4	1.39	0.00	12
1.65	−0.05	0.01	4	0.29	0.01	10
2.2	−0.64	0.01	4	−0.30	0.00	12
3.5	−1.65	0.02	4	−1.32	0.01	9
5	−1.96	0.03	4	−1.54	0.01	11

JD 2450240–JD 2450380 (interval 6)				JD 2451010–JD 2451070 (interval 7)			
λ, μm	mag	se(mag)	N	mag	se(mag)	N
0.36	11.32	0.04	21	8.23	0.16	3
0.45	11.29	0.04	21	8.55	0.12	3
0.55	9.82	0.04	21	7.76	0.04	3
1.25	1.67	0.02	12	1.02	0.01	4
1.65	0.46	0.03	11	−0.05	0.01	4
2.2	−0.28	0.02	11	−0.59	0.02	4
3.5	−1.50	0.02	10	−1.41	0.02	4
5	−1.68	0.02	10	−1.49	0.02	4

cal sizes of the circles correspond roughly to the standard errors in the observed fluxes. The observed fluxes were corrected for interstellar reddening using $E(B - V) = 0\overset{m}{.}07$. Two of the intervals (*2* and *3*) correspond to the state when optical and IR maxima were observed; in interval *4*, hot-source radiation was minimal or absent altogether.

We analyzed the observed energy distributions using a simple model, assuming that the stellar components were embedded in the dust envelope, so that the changes in the envelope's optical depth along the line of sight decreased the observed brightness and redistributed the energy in the spectrum of the system. At 1–2 μm, some 95–99% of the radiation is due to the cool M(5–7) giant [9]. Thus, the first step of our analysis was to fit the near-IR radiation with the radiation from a normal giant attenuated by the dust envelope. As a result, we were able to obtain a fit for the energy distributions at 1–2 μm for the selected intervals with the radiation from a cool star whose spectral type varies from M5 to M7; the changes in the dust envelope's optical depth along the line of sight correspond to variations of $E'(B - V)$ from 0^m in the optically active phase of 1983 to ~$0\overset{m}{.}9$ in 1996. The solid curves in Fig. 5 show the spectral energy distributions of normal M5–M7 giants after their passage through a dust envelope with variable optical depth. These curves are labeled with the corresponding interval numbers; the mean time for the observations, $E'(B - V)$, and the spectral type of the cool star are indicated below each curve. The next step was to estimate and analyze

the excess radiation at $\lambda < 1$ μm and $\lambda > 1.65$ μm (with respect to the cool star's radiation). These excesses are clearly visible in Fig. 5.

At short wavelengths, the maximum radiation from the hot source naturally corresponds to the phase of maximum optical activity (intervals *1*, *2*; Fig. 5). At the maximum LM brightness (interval *3*), the hot source is manifest via a slight excess in the *U* filter. In the optical minimum of 1988 (interval *4*), the cool star is classified as an M7 giant, the color excess of the dust envelope is $\sim0\overset{m}{.}14$, and there is no indication of radiation from the hot source. In the absolute minimum of the *UBVJH* brightness in 1996 (interval *6*), the radiation of the hot source is clearly visible at 0.36–0.55 μm (*UBV*). Based on the expected *K* (2.2 μm) flux from an M5–M7 giant corrected for extinction in the dust envelope, we can estimate the integrated flux from the cool star F_c [27], its luminosity L_c (assuming the distance to CH Cyg is $r \approx 300$ pc), and the radius R_c. These values are presented in Table 3 for seven intervals. The first and second columns contain estimates of the spectral type for the cool star and values of $E'(B-V)$. Note that the energy distributions (or color indices) for stellar spectra of types later than M6 are poorly known, making our classification of M7 for the red giant during interval 4 somewhat arbitrary.

It is apparent from Fig. 5 that there was excess radiation in the *V* filter (0.55 μm) only during interval 1 (1979); the observed and expected radiation agreed within the standard error in all other intervals. In the first interval, the energy distribution of the excess radiation at 0.36–0.55 μm (outside the dust envelope) can be described as the sum of radiation from a hot source mimicking an A3.5V star and ionized gas. In other intervals, the *V* brightness of the hot source is such that its color index is $(B-V)_{hot} \ll -1^m$ and the hot star's radiation is masked by radiation from the cool component and ionized gas. The "hot component" line of Table 3 presents the spectral type of the hot source implied by $(U-B)_{hot}$. Below this line, we give values for the dust-particle temperatures in the envelope T_d. These were derived from $(K-L)_d$ for the excess radiation at 2.2–5 μm, taking into account the optical properties of the dust particles. If we use $(L-M)_d$, we obtain temperatures that are systematically higher by 150–200 K; this could result from a depression at 5 μm due to extinction by silicates.

Our estimates of the dust-particle temperatures in the envelope and its optical depth $\tau_{ex}(\lambda)$ enable us to draw several conclusions concerning the dust envelope in the CH Cyg system. The observed flux from the cool star is

$$F_c(\lambda) \approx (R_c/r)^2 B(T_c, \lambda) e^{-\tau_{ex}(\lambda)}, \qquad (5)$$

where R_c is the cool star's radius, $B(T_c, \lambda)$ is radiation from a blackbody with temperature T_c, and $\tau_{ex}(\lambda)$ is the optical depth of the dust envelope along the line of sight.

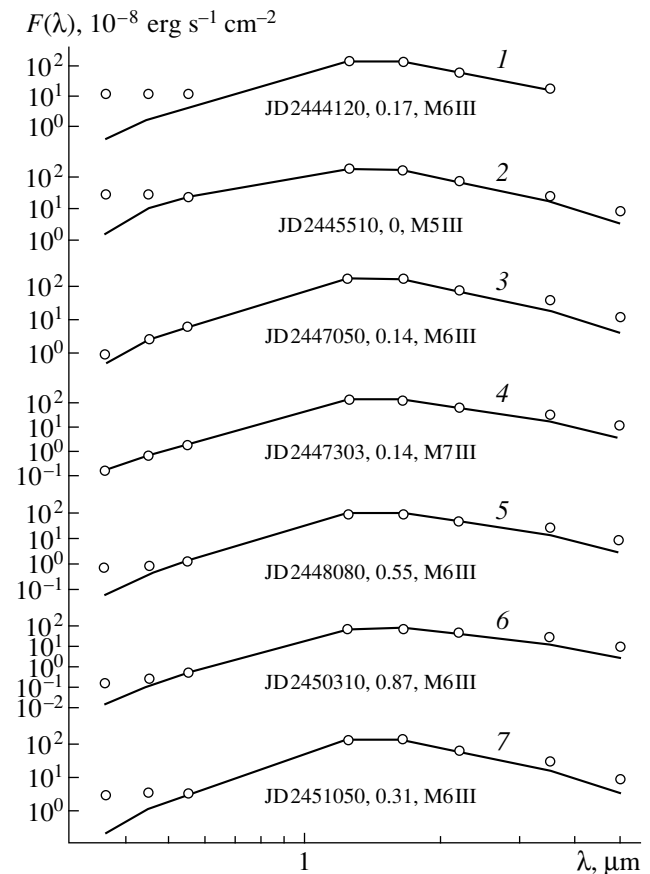$F(\lambda)$, 10^{-8} erg s^{-1} cm^{-2}

Fig. 5. Observed spectral energy distributions of CH Cyg for the most typical intervals in our 1978–1998 observations. The open circles are our data; the solid lines show the spectral energy distributions of the cool star (not corrected for extinction in the dust envelope).

The observed flux from the dust envelope—for instance, in the *L* (3.5 μm) filter—can be estimated from the expression

$$F_d(L) \approx F_{obs}(L) - F_c(L). \qquad (6)$$

In the case of an optically and physically thin dust envelope, we have

$$F_d(L) \approx (R_d/r)^2 B(T_d, L)\tau_{em}(L), \qquad (7)$$

where R_d is the radius of the dust envelope and $\tau_{em}(L)$ is the emission coefficient of the dust envelope.

If the dust envelope is heated only by the cool star's radiation and is spherically symmetrical, the optical depths along the line of sight derived from the extinction of the source radiation and from the emission of the envelope itself should coincide. Using the simple model of Robinson and Hyland [26] for the radiation of a star (in our case, a cool giant) surrounded by a dust

Table 3. Parameters of the CH Cyg system for the seven most typical intervals of 1978–1998 JD 2400000+

Parameter	44120	45510	47050	47303	48080	50310	51050
Sp (cool comp.)	M6III	M5III	M6III	M7III	M6III	M6III	M6III
$E'(B-V)$	0.17	0	0.14	0.14	0.55	0.87	0.31
F_c, 10^{-6} erg s^{-1} cm^{-2}	2.76	3.12	3.24	2.72	2.34	2.26	2.77
L_c, $L_\odot$	7700	8700	9100	7600	6500	6300	7800
R_c, 10^{13} cm	2.4	2.4	2.6	2.8	2.3	2.2	2.4
Hot comp.	A3.5 V + gas	gas (B2V ?)	gas (B7V ?)	–	gas (O5V ?)	gas (O9.5V ?)	gas (B1V ?)
T_d, K	750	750	650	550	600	670	700
τ_{em} (L)	0.04	0.06	0.17	0.23	0.16	0.19	0.11
τ_{ex} (L)	0.02	0	0.02	0.02	0.07	0.10	0.04
R_d, 10^{14} cm	6.3	7.3	10	14	11	7.8	7.6
F_d, 10^{-7} erg s^{-1} cm^{-2}	2.2	4.9	11	11	8.4	1.1	6.8
L_d, $L_\odot$	610	1400	3100	3100	2400	3100	2000
M_d, 10^{-7} $M_\odot$	1.4	2.7	14	38	16	10	5.5
$\dot{M}_d$, $M_\odot$/yr		$+3.4 \times 10^{-8}$	$+1.7 \times 10^{-7}$	$+3.5 \times 10^{-6}$	-1×10^{-6}	-9.8×10^{-8}	-2.2×10^{-7}

envelope with particles resembling interstellar dust particles, we can use Eqs. (5) and (7) to estimate

$$
\begin{aligned}
\tau_{em}(L) &\approx [F_d(L)/F_c(L)](R_c/R_d)^2 \\
&\times [B(T_c, L)/B(T_d, L)]e^{-\tau_{ex}(L)} \\
&\approx 4[F_d(L)/F_c(L)](T_d, T_c)^{5.68} \\
&\times [B(T_c, L)/B(T_d, L)]e^{-\tau_{ex}(L)}.
\end{aligned}
\tag{8}
$$

The $\tau_{em}(L)$ values obtained from Eq. (7) using the data from Tables 2 and 3 are presented in Table 3 below the T_d values. To facilitate comparison, the next line contains the optical depths along the line of sight for the dust envelope at 3.5 μm (L) calculated using the relation $\tau_{ex}(L) = 0.92A'(L) = 0.92 \times 0.13E'(B-V)$.

Comparing $\tau_{em}(L)$ and $\tau_{ex}(L)$, we conclude that the dust envelope of CH Cyg is not spherically symmetrical and that a transparent region, whose size exceeds the projected radius of the cool component on the dust envelope, is continuously present along the line of sight. During the phase of optical activity of 1983, we can detect emission from the dust envelope (the system's IR radiation exceeds that from an M5 giant) but not extinction (the unreddened M5 giant is apparent in the radiation at λ 1.25 and 1.65 μm). On average, the optical depth of the dust envelope along the line of sight increased from 1983 until 1996 ($E'(B-V) \sim 0^m - 0^{m}.9$), after which it decreased nearly to the 1989 level. The emission coefficient reached its maximum in 1988 after increasing more than sixfold compared to its 1979 value, then decreased by nearly a factor of 2 by 1999. The dust envelope of CH Cyg along the line of sight was densest in 1996, when the star's *BVJH* brightness reached a low record (Table 1; Figs. 1, 2).

Note that the linear trend in the *J–H* variations in Fig. 2 (solid line) primarily reflects changes in the optical depth of the dust envelope along the line of sight in 1978–1998. The scatter of the data points around the regression line is partly due to the different states of the cool component (M5–M7). The variations of the *L* brightness and of *K–L* reflect both extinction in the dust envelope (solid lines) and emission (dashed regression lines).

Using the simple model we adopted, we estimated the dust envelope's radius, integrated flux (luminosity), and mass for the seven time intervals. We described the radius using the expression

$$
R_d \approx 0.5R_c(T_c T_d^{-1})^{2.84},
\tag{9}
$$

where R_c and T_c are the radius and temperature of the M5–M7 giant and R_d and T_d are the radius and temperature of the dust envelope. The integrated flux from the emitting dust envelope was estimated from the observed *L* flux (3.5 μm):

$$
F_d \approx F_d(L)[\sigma T_d^4 \langle \tau_d \rangle / B(T_d, L)\tau_{em}(L)],
\tag{10}
$$

where $\langle \tau_d \rangle$ is the optical depth averaged over the spectrum of the dust envelope. The mass of the emitting dust envelope is given by the expression

$$
M_d \approx 4\pi R_d^2(\rho V)(n\Delta R),
\tag{11}
$$

where $\rho \sim 3$ g/cm^3 is the density of the dust envelope material; $V = 4\pi a^3/3$ is the volume of a dust particle; $(n\Delta R)_{em} \approx \tau_{em}(L)/Q(L)\pi a^2$ is the number of emitting dust particles in a column with a 1-cm^2 cross section, where $a \sim 0.1$ μm is the radius of a dust particle; and $Q(L) \sim 0.03$ is the extinction efficiency for the dust particles.

The resulting values are collected in the bottom lines of Table 3. The data in Table 3 lead us to the following conclusions about the CH Cyg system in 1978–1998.

(1) The spectral classification of the cool star based on near-IR observations shows that, during the time interval considered, the spectral type of the cool star varied in the range M5III–M7III. The spectral features of an M5 giant were observed during the phase of maximum activity of the hot source, and those of an M7 giant when optical signatures of the hot source were nearly completely absent.

(2) The cool giant's luminosity varied in the range (6300–9100) $L_\odot$, with its maximum and minimum values achieved when it had the same spectral type (M6). In other words, the changes in the cool giant's luminosity were primarily due to changes in its radius (up to 30%).

(3) The observed energy distribution for the optical radiation that is in excess of the red giant's light does not enable us to determine the fraction of this radiation due to the hot star, except possibly at the beginning of the 1978–1985 activity phase.

(4) Fivefold luminosity changes in the dust envelope were observed, with the ratio of the luminosities of the dust envelope and cool giant varying from 0.08 to 0.5. In other words, assuming radiation balance, up to 50% of the radiation of the cool star could be absorbed in the emitting part of the envelope.

(5) The dust-particle temperature in the emitting envelope varied in the range 550–750 K; the minimum occurred when the cool giant's spectral type was M7. The envelope's radius changed by more than a factor of 2.

(6) The expansion of the emitting dust envelope from 1979 until 1988 accelerated: the expansion velocity was initially ~8 km/s, whereas it reached a maximum of ~180 km/s in 1987–1989. The opposite process began in 1988: the emitting radius of the dust envelope began to decrease at a rate of ~45 km/s and later decreased at ~3 km/s from 1996 until 1998. By the summer of 1999, the size of the emitting dust envelope had nearly returned to its size in 1979.

(7) The mass of the emitting dust envelope increased from 1979 until 1996 by approximately a factor of 27 then decreased almost sevenfold by 1999. In 1979, the mass of the emitting dust envelope was ~$1.4 \times 10^{-7} M_\odot$; and in 1988, it had grown to ~$3.8 \times 10^{-6} M_\odot$. The emitting dust envelope began to dissipate in 1989. The rate of mass loss by the cool star increased from 1979 until 1987, although it remained typical of single cool giants. From 1987 until 1988, the mass-loss rate abruptly increased to ~$3.5 \times 10^{-6} M_\odot$/yr; and in the following years (up to the summer of 1999), the envelope itself began to lose mass at a rate exceeding that of the cool star.

(8) If the thickness of the layer where the dust particles are formed or disrupted is small compared to the radius of the dust envelope and the mass-loss and
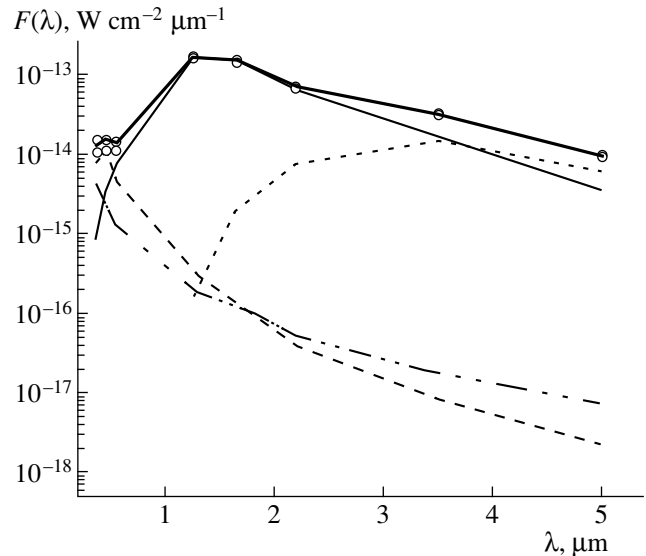

Fig. 6. Mean (1978–1998) spectral energy distributions for CH Cyg corrected for extinction in the dust envelope. The open circles are fluxes averaged over the time interval; the thin solid curve is the spectral energy distribution of a normal M6 giant; the dashed curve is the spectral energy distribution of a normal B8V star; the dash-dot curve is the spectral energy distribution of ionized gas with $T_e \sim 10^4$ K and $N^2V \sim 4 \times 10^{59}$ cm^{-3}; the dotted curve is the spectral energy distribution of a dust envelope with particle temperature ~650 K and $\tau_{em}(L) \sim 0.16$; the thick solid curve is the sum of the radiation from the above components.

expansion rates for the dust envelope are constant, the dust-particle density will decrease with distance from the star as $n_d(R_d) \propto R_d^{-\alpha}$, where $\alpha \sim 1$–2. When $\alpha \sim 2$, $\tau_{em} R_d$ should remain nearly constant. In our case, this quantity changes by more than an order of magnitude, increasing from 1979 until 1988 and then decreasing until 1999. Our estimates of α from the relation $\tau_{em} R_d \propto n_d(R_d) R_d^2 \propto R_d^{(2-\alpha)}$ indicate that $\alpha_\uparrow \sim -1.2$ in 1979–1988 (matter arrives at the envelope at a higher rate than it leaves), while $\alpha_\downarrow \sim +0.7$ from 1990 until 1998 (matter leaves the envelope at a higher rate than it arrives). Note that the largest input of matter into the envelope occurred after the record phase of optical activity in 1978–1985. If the gas-to-dust ratio in the envelope is ~100, the mass ejected in 1988 was ~$4 \times 10^{-4} M_\odot$.

We can estimate the mean parameters of the CH Cyg system by analyzing the data averaged over the entire period covered by our observations. For this purpose, from our observations of CH Cyg, we selected only nights with simultaneous optical and IR photometry. There were about a hundred such nights in 1978–1998. These data were averaged, and are given in the second column of Table 4. The third and fourth columns of Table 4 contain standard errors se(mag) and the number of nights averaged N. Using the adopted approach and the above relations, we obtained mean
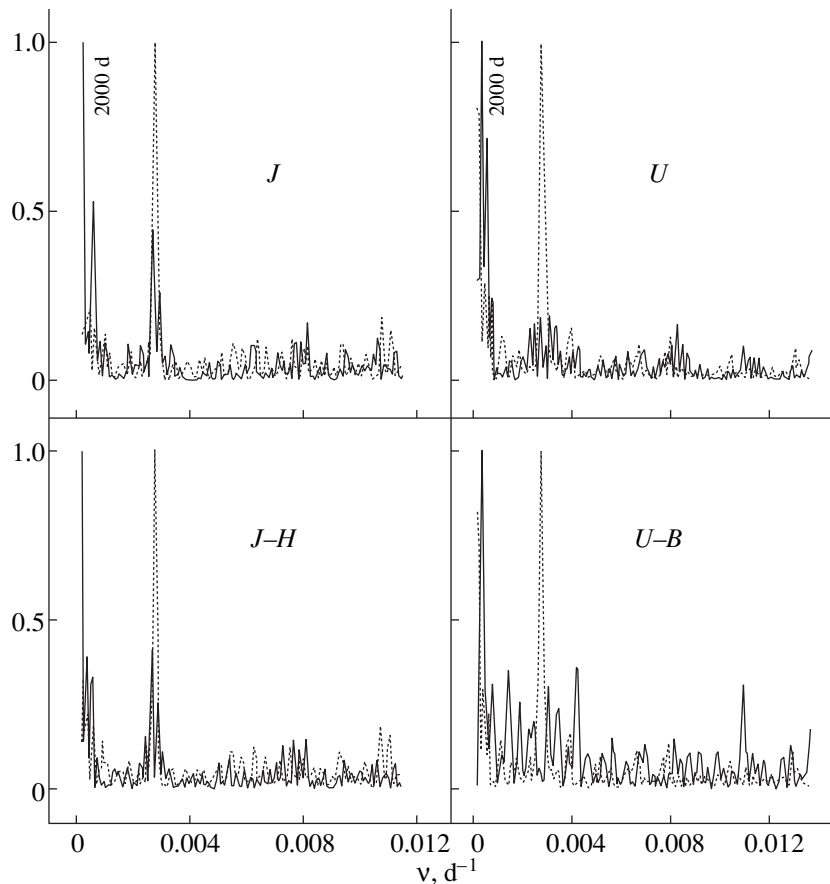
Fig. 7. Power spectra (solid curves) and spectral windows (dashed lines) derived from our 1978–1998 *JH* and *UB* photometry of CH Cyg.

parameters for the CH Cyg system, which are collected in Table 5. Analysis of the mean spectral energy distribution of CH Cyg at 0.36–5 μm shows that, after taking into account extinction in the dust envelope along the line of sight ($E' \sim 0.^{m}5$), the observed distribution is the sum of radiation from three (possibly four) sources. In the IR (1.25–5 μm), the radiation corresponds to a cool

M6 giant and a dust envelope with extinction optical depth along the line of sight $\tau_{ex}(L) \sim 0.06$ and emission coefficient $\tau_{em}(L) \sim 0.16$. At optical wavelengths, a hot source, possibly a main-sequence B8V star, is apparent. The remaining light in the *U* filter may be associated with ionized gas. Figure 6 shows the mean spectral energy distribution and the spectral energy distributions of the individual components.

3.5. Period Search

Several periodic components in the light of CH Cyg due to possible orbital motion, as well as intrinsic variability of the various components of the system, have been clearly detected at optical wavelengths (see references in the Introduction). During the first years of our observations of CH Cyg, we attempted to detect a periodic component in the near IR. Our initial analysis [24] using software developed by Yu.K. Kolpakov suggested the presence of components with periods ~2025 and ~28 days. The 1500- to 2000-day time scale for variations is clearly visible in the IR light and color curves in Figs. 1 and 2. We have undertaken a detailed analysis of the photometric observations of CH Cyg for 1975–1998 in order to search for periodic components
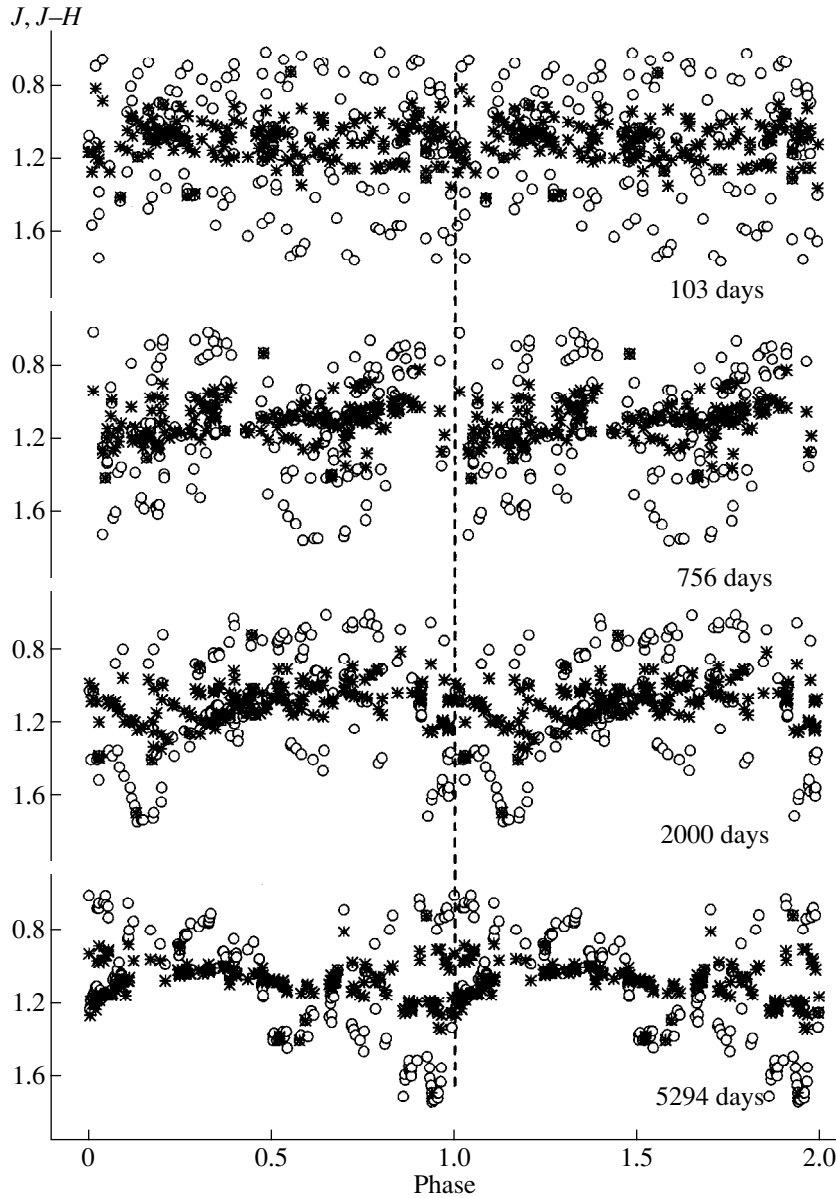
Table 4. Optical and IR photometry of CH Cyg averaged over the entire observation period, 1978–1998

Filter	JD 2443800–JD 24551100		
	mag	se(mag)	N
U	8.96	0.20	109
B	9.07	0.16	109
V	7.90	0.13	109
J	1.17	0.03	105
H	0.06	0.02	98
K	−0.51	0.02	104
L	−1.43	0.02	83
M	−1.60	0.02	74

Fig. 8. Phased J light curves (open circles) and (J–H) color curves (asterisks) folded with periods of 103, 756, 2000, and 5294 days.

in the IR of CH Cyg. We used software designed to search for periods in the light curves of nonstationary stars developed at the Sternberg Astronomical Institute by Antokhin, Kolpakov, and Lyutyĭ. Our analysis of our data in filters from U to M confirms the presence of a 1800- to 2000-day period. This period is detected in both the optical and IR, both accounting for, and not accounting for, the linear trend. As an example, Figure 7 shows the power spectra (together with the spectral windows) derived from our JH and UB observations of CH Cyg for 1975–1998, which clearly display the possible periodic components and the level of their reliability. When computing the power spectra, we did not take the linear trend into account. Figure 8 shows phased curves for the J brightness (open circles) and for

J–H for several of the most often discussed periods. These phased curves were made using all the data. In our opinion, there are appreciable periodic components in each graph of Fig. 8.

Table 5. Mean parameters of the components in the CH Cyg system

Component	F, erg s^{-1} cm^{-2}	T, K	R, $R_\odot$	L, erg/s
Cool (M6III)	2.6×10^{-6}	3000	320	2.85×10^{37}
Hot (B8V)	7×10^{-8}	11 000	3.9	7.8×10^{35}
Dust	1.1×10^{-7}	650	12 300	1.2×10^{36}
$\tau_{ex}(L) \sim 0.06$				
$\tau_{em}(L) \sim 0.16$				
$M_d \sim 10^{-6}\,M_\odot$				

4. CONCLUSIONS

In conclusion, we note the following principal photometric and physical features of CH Cyg in 1978–1998.

(1) The greatest reddening in the optical took place at JD 2446894–2447825. The minimum optical brightness was observed at JD 2450233–2450429. The greatest reddening at 0.55–2.2 μm (V, J, H, and K) was observed in late 1996, simultaneous with a brightness minimum from U to K. We observed an optical brightness maximum at JD 2444798–2445588, simultaneous with a JHK brightness maximum. IR activity (maximum LM brightness) was observed at JD 2446894–2447773, when the system was reddest at optical wavelengths.

(2) The mean 0.36- to 5-μm spectral energy distribution of CH Cyg, derived by averaging data from nearly a hundred observing nights and accurate to better than 10% in the IR fluxes, can be represented as the sum of light from four sources: a normal M6 giant, a hot source whose B–V resembles that of a B8V star, a dust envelope with particle temperature ~650 K, and possibly a gas envelope.

(3) Our analysis of our entire data set in filters from U to M confirms the presence of a 1800- to 2000-day period. This period is detected in both the optical and IR, both taking into account, and not taking into account, the linear trend in the data.

(4) The dust envelope of CH Cyg is not spherically symmetrical. There probably exists a permanent clearing along the line of sight, whose size exceeds the projected radius of the cool component onto the dust envelope. The mean (1978–1998) optical depth of the dust envelope along the line of sight is $\tau_{ex}(L) \sim 0.06$; the emission coefficient is $\tau_{em}(L) \sim 0.16$.

(5) The cool star's spectral type varied in the range from M5III to M7III. The spectral type was M5 during the phase of maximum activity of the hot source, whereas it was M7 when there was almost no evidence for the hot source in the optical.

(6) The cool giant's luminosity varied in the range (6300–9100) $L_\odot$, primarily due to changes in its radius.

(7) The ratio of the luminosities of the dust envelope and the cool giant varied from 0.08 to 0.5; i.e., assuming radiation balance, the emitting part of the envelope could absorb up to 50% of the cool star's radiation.

(8) The dust-particle temperature in the emitting envelope varied from 550 to 750 K, and its radius varied by more than a factor of 2.

(9) The expansion of the dust envelope from 1979 to 1988 showed acceleration (from ~8 to ~180 km/s). The opposite process began in 1988: the dust envelope's emitting radius decreased at ~45 km/s, slowing to ~3 km/s in 1996–1998. By the summer of 1999, the size of the emitting dust envelope had nearly returned to its size in 1979.

(10) In 1979, the mass of the emitting dust envelope was ~$1.4 \times 10^{-7} M_\odot$ and reached ~$3.8 \times 10^{-6} M_\odot$ in 1988. Beginning in 1989, the emitting dust envelope began to dissipate. The mass-loss rate from the cool star increased from 1979 to 1987; in 1987–1988, there was an abrupt increase in the mass-loss rate to ~$3.5 \times 10^{-6} M_\odot$/yr. In subsequent years (up to the summer of 1999), the envelope itself began to lose mass at a rate exceeding that of the cool star. Assuming the gas-to-dust ratio in the envelope is ~100, the mass of matter ejected in 1988 was ~$4 \times 10^{-4} M_\odot$.

REFERENCES

1. F. C. Gillet, K. M. Merril, and W. A. Stein, Astrophys. J. **164**, 83 (1971).
2. J. P. Swings and D. A. Allen, Publ. Astron. Soc. Pac. **84**, 523 (1972).
3. D. F. Dickinson, K. P. Bechis, P. Kenneth, and A. H. Barrett, Astrophys. J. **180**, 831 (1973).
4. D. Morrison and Th. Simon, Astrophys. J. **186**, 193 (1973).
5. P. N. Kholopov, N. N. Samus', V. P. Goranskiĭ et al., General Catalog of Variable Stars [in Russian] (Nauka, Moscow, 1985), Vol. 1.
6. O. G. Taranova and B. F. Yudin, Astron. Astrophys. **117**, 209 (1983).
7. A. P. Ipatov, O. G. Taranova, and B. F. Yudin, Astron. Astrophys. **135**, 325 (1984).
8. O. G. Taranova and B. F. Yudin, Astrophys. Space Sci. **146**, 33 (1988).
9. O. G. Taranova and V. I. Shenavrin, Pis'ma Astron. Zh. **15**, 1020 (1989) [Sov. Astron. Lett. **15**, 444 (1989)].
10. O. G. Taranova, Pis'ma Astron. Zh. **16**, 1011 (1990) [Sov. Astron. Lett. **16**, 434 (1990)].
11. O. G. Taranova, Pis'ma Astron. Zh. **17**, 253 (1991) [Sov. Astron. Lett. **17**, 107 (1991)].
12. O. G. Taranova and B. F. Yudin, Astron. Astrophys. **257**, 615 (1992).
13. O. G. Taranova and B. F. Yudin, Astron. Zh. **69**, 262 (1992).
14. O. G. Taranova, B. F. Yudin, and E. A. Kolotilov, Pis'ma Astron. Zh. **21**, 529 (1995).
15. U. Munari, B. F. Yudin, E. A. Kolotilov, and T. V. Tomov, Astron. Astrophys. **311**, 484 (1996).

16. *Physical Processes in Symbiotic Binaries and Related Systems*, Ed. by J. Mikolajewska (Copernicus Foundation for Polish Astronomy, Koniki, 1997).

17. Y. Yamashita and H. Maehara, Publ. Astron. Soc. Jpn. **31**, 307 (1979).

18. K. H. Hinkle, F. C. Fekel, D. S. Johnson, and W. W. G. Schrlach, Astron. J. **105**, 1074 (1993).

19. A. Skopal, M. F. Bode, H. M. Lloyd, and S. Tamura, Astron. Astrophys. **308**, L9 (1996).

20. A. É. Nadzhip, V. I. Shenavrin, and V. G. Tikhonov, Tr. Gos. Astron. Inst., Mosk. Gos. Univ. **58**, 119 (1986).

21. V. I. Moroz, O. G. Taranova, V. I. Shenavrin, and B. F. Yudin, Astron. Tsirk., No. 1056 (1979).

22. H. L. Johnson, Annu. Rev. Astron. Astrophys. **4**, 193 (1966).

23. J. Koorneef, Astron. Astrophys., Suppl. Ser. **51**, 489 (1983).

24. O. G. Taranova, Astron. Tsirk., No. 1473, 7 (1986).

25. O. G. Taranova, Pis'ma Astron. Zh. (1999) (in press).

26. G. Robinson and A. R. Hyland, Mon. Not. R. Astron. Soc. **180**, 499 (1977).

27. D. E. Blackwell, A. D. Petford, and M. J. Shallis, Astron. Astrophys. **82**, 249 (1980).

Translated by N. Samus'

Precision Astrometry with Schmidt Telescopes

K. V. Kuimov[1], F. D. Sorokin[2], A. V. Kuz'min[1], and N. T. Barusheva[1]

[1]Sternberg Astronomical Institute, Universitetskiĭ pr. 13, Moscow, 119899 Russia
[2]Bauman State Technical University, Vtoraya Baumanskaya ul. 5, Moscow, 107005 Russia
Received May 17, 1999

Abstract—Schmidt telescopes currently provide nearly the only means to obtain positions of faint objects with respect to the standard ICRS reference system. However, the lack of adequate astrometric calibration methods to account for the specific properties of Schmidt telescopes leads to residual systematic errors of up to 1″. The main source of systematic errors is plate bending during exposure. A high-precision reduction technique to account for this effect is proposed. Application of this technique to observations acquired with the Schmidt telescopes of the Palomar and Anglo-Australian Observatories reduced the systematic errors by a factor of 2.5 and gave them a simpler structure, while simultaneously decreasing the number of unknowns in the reduction model threefold. Application of the new method, with appropriate account for the design of the particular plateholder used, will make it possible to use Schmidt telescopes to determine high-precision positions for virtually all objects detected in photographic surveys. © 2000 MAIK "Nauka/Interperiodica".

1. INTRODUCTION

Over the last two decades, Schmidt telescopes have been used more and more frequently as astrometric instruments. The reason is obvious: the limiting magnitude of classical astrographs became unsatisfactory long ago. In addition, photographic surveys carried out with Schmidt telescopes operating in various wavelength intervals have already covered the entire sky several times. Such surveys often serve as the only source of information about faint objects, in particular, about their positions.

However, a specific difficulty is encountered when a Schmidt telescope is used to determine the positions of celestial bodies: the telescope's focal surface is spherical. Because of this, prior to exposure, a photographic plate must be put in a special plateholder, where it is deformed in order to bring the emulsion surface as close to the focal surface as possible. Such plates are measured after the deformation is removed.

It is well known that positional measurements obtained using Schmidt telescopes often contain systematic errors, sometimes exceeding 1″ [1]. In the present paper, we show that such errors are dominated by the effect of plate deformation and suggest a new method to account for the influence of deformation on the measured positions of stars.

2. THE STANDARD METHOD FOR ACCOUNTING FOR DEFORMATION

Apparently, the first attempt to calculate corrections to account for plate deformations based on elasticity theory was undertaken by Shepherd [2], who computed the deformation of the plate's upper surface assuming that

1) the plate is round;

2) the plate is subject to elastic deformation and remains isotropic;

3) the plate is in contact with a spherical support over its entire surface;

4) there is no friction between the plate and support;

5) at the position where the plate touches the ring holding it to the spherical surface, there is no tension along the tangent to this surface.

Under these assumptions, the correction u to the distance of a point from the plate center measured with a measuring machine is given by the formula

$$u = \frac{1}{16}(1-\mu)R\gamma^2\lambda - \frac{1}{48}(1-3\mu)R\lambda^3. \qquad (1)$$

Here, u is the correction in length units, μ is the Poisson ratio, R is the radius of curvature of the focal surface, γ is the angular radius of the field of view (from the plate center to the restraining ring) in radians, and λ is the angular distance of the point on the plate from its center in radians. The Poisson ratio describes the elasticity of the plate material (in our case, glass) [3].

As might be expected (given the first assumption), the correction implies a scale change and cubic distortion. A similar result was obtained in [4] for the deformation of a film. Such systematic errors should be completely accounted for in a reduction model relating the celestial and measured coordinates of a source via complete third-order polynomials in the coordinates. However, this is not the case, as we will show in Section 3. Thus, the use of corrections calculated from Eq. (1) does not completely exclude systematic errors due to plate deformation.

3. THE ENERGY METHOD
FOR CALCULATING DEFORMATIONS

We propose a means to calculate the deformations for the realistic case of a square plate. This makes the use of a nonlinear plate deformation theory unavoidable [5].

Let us introduce a system of coordinates x, y, z, as shown in Fig. 1, rigidly connected with the telescope and the celestial sphere. Its origin is at the point where the deformed plate's axis of symmetry crosses its median surface. When the plate is deformed, points on the median surface are displaced. We designate the displacements along the x, y, z coordinate axes $u(x, y)$, $v(x, y)$, and $w(x, y)$, respectively.

To derive the desired displacements of the photographic emulsion particles (u_e, v_e) from the displacements of points on the median surface, we must assume that the Kirchhoff–Love ("rigid normal") hypothesis is valid: points on the normal to the surface of the undeformed plate remain on the normal to the surface of the deformed plate. In other words, the thickness of the plate remains the same. In this case, we may use the relations

$$u_e = u - \frac{h}{2}\frac{\partial w}{\partial x}, \quad v_e = v - \frac{h}{2}\frac{\partial w}{\partial y}. \quad (2)$$

The solution can be simplified by assuming that the plate lies on a sphere. In this case, one of the displacements is known *a priori*; the vertical displacement w is determined by the sphere's radius of curvature:

$$w = -\frac{x^2 + y^2}{2R}. \quad (3)$$

Equation (3) is an approximate equation for a sphere, which differs from the exact equation only slightly, since the size of the plate is much smaller than the radius of curvature R.

It is probably impossible to find exact analytical solutions for the horizontal displacements u and v (analytical solutions in the nonlinear theory of plate bending are known only for the simplest cases). A universal technique for finding approximate solutions is the principle of virtual displacements (Lagrange's principle), according to which the total potential energy of an elastic system is minimum when it is in equilibrium [3].

In our case, the total potential energy is just the deformation energy. External forces (the pressure of the spherical support on the plate) are directed along the normal to the sphere, and virtual displacements are limited to the tangential plane. Thus, we need not take the work of external forces into account. The deformation energy is subdivided into the bending energy U_b and the expansion and contraction energy (membrane deformation energy) U_s:
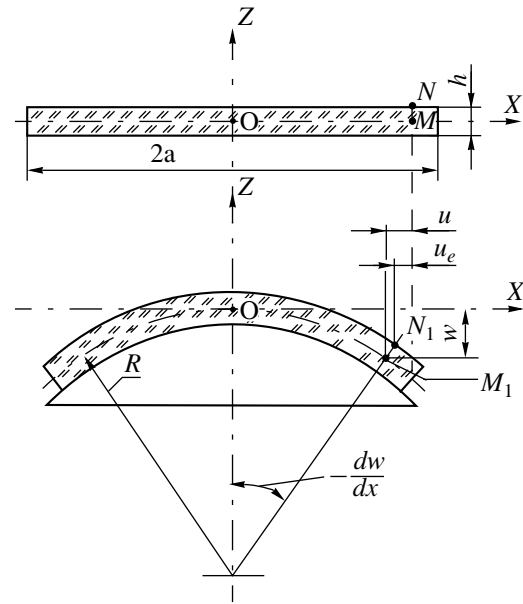
$$U = U_b + U_s. \quad (4)$$

Fig. 1. Accounting for plate deformations due to bending in a Schmidt telescope plateholder.

The plate's bending energy U_b can be expressed solely in terms of the normal displacement w, which is known [5]. When the displacements u and v are varied, this part of the energy will not change. Thus, the problem reduces to finding the minimum membrane deformation energy for a plate lying without friction on a spherical surface:

$$U[u(x, y), v(x, y)] \longrightarrow \min, \quad (5)$$

where

$$U = \frac{Eh}{2(1-\mu^2)} \times \int_{-a}^{a}\int_{-a}^{a}\left(\varepsilon_x^2 + \varepsilon_y^2 + 2\mu\varepsilon_x\varepsilon_y + \frac{1-\mu}{2}\gamma_{xy}^2\right)dxdy. \quad (6)$$

Here, h is the plate's thickness, a is half the plate's size, E is the elasticity modulus (Young's modulus), μ is the Poisson ratio, ε_x and ε_y are the deformations along the x and y axes, and γ_{xy} is the shear.

In nonlinear plate theory, the deformations of the median surface are [5, 6]

$$\varepsilon_x = \frac{\partial u}{\partial x} + \frac{1}{2}\left(\frac{\partial w}{\partial x}\right)^2,$$

$$\varepsilon_y = \frac{\partial v}{\partial y} + \frac{1}{2}\left(\frac{\partial w}{\partial y}\right)^2, \quad (7)$$

$$\varepsilon_{xy} = \frac{\partial u}{\partial y} + \frac{\partial v}{\partial x} + \frac{\partial w}{\partial x}\frac{\partial w}{\partial y}.$$

The last terms in (7) distinguish the nonlinear from the linear plate-bending theory. It is these terms that introduce heterogeneity into the system of equations (7). If we drop these terms, the determination of the energy minimum becomes trivial: $u = v = 0$. In our problem, in view of (3), Eqs. (7) take the particular form

$$\varepsilon_x = \frac{\partial u}{\partial x} + \frac{1}{2}\left(\frac{x}{R}\right)^2,$$

$$\varepsilon_y = \frac{\partial v}{\partial y} + \frac{1}{2}\left(\frac{y}{R}\right)^2, \tag{8}$$

$$\gamma_{xy} = \frac{\partial u}{\partial y} + \frac{\partial v}{\partial x} + \frac{xy}{R^2}.$$

Substituting (8) into (6) and then into (5), we obtain a system of two partial differential equations satisfied by the desired functions, $u(x, y)$ and $v(x, y)$:

$$2\frac{\partial^2 u}{\partial x^2} + (1-\mu)\frac{\partial^2 u}{\partial y^2} + (1+\mu)\frac{\partial^2 v}{\partial x \partial y} = -(3-\mu)\frac{x}{R^2},$$

$$2\frac{\partial^2 v}{\partial y^2} + (1-\mu)\frac{\partial^2 v}{\partial x^2} + (1+\mu)\frac{\partial^2 u}{\partial x \partial y} = -(3-\mu)\frac{y}{R^2}. \tag{9}$$

The system (9) must be supplemented by boundary conditions; we do not write these here because we do not seek an exact analytical solution. Instead, we find approximate solutions using two different methods: Ritz's method and a finite-element method.

3.1. Polynomial Solution (Ritz's Method)

We can find the displacements u and v, for example, in the form of seventh-order polynomials:

$$u = c_1 x + c_2 xy^2 + c_3 x^3 + c_4 xy^4 + c_5 x^3 y^2 + c_6 x^5$$
$$+ c_7 xy^6 + c_8 x^3 y^4 + c_9 x^5 y^2 + c_{10} x^7,$$

$$v = c_1 y + c_2 yx^2 + c_3 y^3 + c_4 yx^4 + c_5 y^3 x^2 + c_6 y^5$$
$$+ c_7 yx^6 + c_8 y^3 x^4 + c_9 y^5 x^2 + c_{10} y^7. \tag{10}$$

The polynomials (10) are derived from the full seventh-order polynomials by rejecting terms that do not satisfy the conditions for the problem's symmetry with respect to the x and y axes and the plate's diagonal: $u(-x, y) = -u(x, y)$, $u(x, -y) = u(x, y)$, $v(-x, y) = v(x, y)$, $v(x, -y) = v(x, y)$, $u(x, y) = v(y, x)$.

In this way, the symmetry conditions simplify the solution: instead of 56 coefficients, we need find only 10. We determined these coefficients from the condition that the deformation energy be minimum. After substituting (10) into (8) and into (6), the energy U becomes a function of ten variables, $u = U(c_1, c_2, \ldots, c_{10})$, and the condition of minimum energy becomes

$$\frac{\partial U}{\partial c_i} = 0, \quad i = 1, \ldots, 10. \tag{11}$$

The calculations required to construct and solve the system (11) are very cumbersome, but quite straightforward. We found the analytical solution to Eqs. (11) using the Maple5 computer algebra package. The following expressions were obtained for the polynomial coefficients (10):

$$c_1 = -\frac{1}{32}\frac{a^2(5576184 - 2838722\mu - 2670505\mu^2 - 68182\mu^3 + 1225\mu^4)}{zR^2},$$

$$c_2 = +\frac{7}{16}\frac{(650100 - 444408\mu - 367537\mu^2 - 9018\mu^3 - 175\mu^4)}{zR^2},$$

$$c_3 = +\frac{1}{96}\frac{(50360576 + 15569894\mu - 4074959\mu^2 - 199490\mu^3 + 3675\mu^4)}{zR^2},$$

$$c_4 = +\frac{35}{32}\frac{(353964 + 309372\mu + 70451\mu^2 + 1752\mu^3 - 35\mu^4)}{za^2R^2},$$

$$c_5 = -\frac{35}{16}\frac{(110484 - 55420\mu - 53981\mu^2 - 1208\mu^3 + 35\mu^4)}{za^2R^2},$$

$$c_6 = -\frac{77}{16}\frac{(7026 + 19511\mu + 7116\mu^2 - 221\mu^3)}{za^2R^2},$$

$$\tag{12}$$

$$c_7 = +\frac{1001}{16}\frac{(226 + 357\mu + 131\mu^2)}{za^4R^2},$$

$$c_8 = -\frac{35}{32}\frac{(149672 + 225090\mu + 77205\mu^2 + 1752\mu^3 - 35\mu^4)}{za^4R^2},$$

$$c_9 = +\frac{231}{16}\frac{(7026 + 10225\mu + 3285\mu^2 + 86\mu^3)}{za^4R^2},$$

$$c_{10} = -\frac{143}{16}\frac{(226 + 357\mu + 131\mu^2)}{za^4R^2}.$$

Here, $z = -2467724 - 1208496\mu - 28609\mu^2 + 450\mu^3$, a is half the plate length, and R is the radius of curvature of the plate's median surface (Fig. 1).

It is apparent from (12) that neither the elasticity modulus E nor the plate thickness h enter the expressions for $u(x, y)$ and $v(x, y)$, since the factor Eh cancelled out in all equations (11). We can find the displacements of the photographic plate's points from Eq. (2), taking into account Eq. (3):

$$u_e = u + \frac{h}{2}\frac{x}{R},$$
$$\quad\quad\quad (13)$$
$$v_e = v + \frac{h}{2}\frac{y}{R}.$$

3.2. Solution Using the Finite-Element Method

Our calculation of distortions using a finite-element method (FEM) was aimed at estimating the errors in the approximate solution (12). The finite-element solution is much more accurate than the polynomial solution: the order of the polynomials cannot be very high due to numerical limitations, whereas the finite-element grid can be made quite dense. The disadvantage of the method is that it does not yield a solution in analytical form. Having changed any parameter (for example, the Poisson ratio μ), we must repeat the FEM calculation, whereas there is no need to recalculate the polynomial coefficients (12) when a parameter changes.

We constructed the solution using the traditional FEM method [7]. We split a quadrant of the photographic plate into $n \times n$ square finite elements (we used n values from 10 to 40). We searched for the displacement field in each element j in the form of the bilinear functions

$$u_j(x, y) = A_{1j} + A_{2j}x + A_{3j}y + A_{4j}xy,$$
$$v_j(x, y) = B_{1j} + B_{2j}x + B_{3j}y + B_{4j}xy.$$
$$\quad\quad\quad (14)$$

The eight unknown coefficients can easily be expressed in terms of the displacements of the eight nodes (two displacements for each of the four corners of a square). Substituting the relations (14) for all elements into (8) and (6), we transform the energy U into

a quadratic function of the node displacements. In order for the nodes of the element grid to be in equilibrium, the derivatives of the energy with respect to the node displacements must vanish. This leads to a poorly filled high-order system of linear algebraic equations that must be solved numerically. In this way, we found the displacements for all nodes of the finite-element grid.

Note that, in the problem under consideration, it is difficult (though not impossible) to apply universal software packages, such as NASTRAN or ANSYS, since their standard finite-element programs do not allow for heterogeneities such as (8). For this reason, we found the solution using a FEM software package developed at the Applied Mathematics Department of Bauman State Technical University in Moscow, especially for the treatment of nonstandard problems.

3.3. Comparison of the Polynomial and FEM Solutions

We compared the displacement fields computed using the FEM with the polynomial solution (12). We calculated the magnitude of the maximum difference between the displacement vectors derived using the two methods. The values of these differences as a function of the number of elements in the plate quadrant are presented in the table. We can see that the accuracy of the analytical polynomial solution is no worse than 1 μm.

4. APPLICATION OF THE METHOD

To demonstrate the effectiveness of the proposed method for computing plate-deformation corrections, we present the results of our reduction of the PAL–QV survey plates to the Tycho reference catalog [8, 9]. Observations for this survey were acquired using the Schmidt telescope of the Mt. Palomar Observatory in 1982–1984 [10] in order to compile a guide-star catalog for the Hubble Space Telescope [11]. The telescope's aperture is $D = 1.2$ m, its focal length is $F = 3.07$ m, and the angular size of its field of view on a 355×355-mm plate is $6.5 \times 6.5°$. The published catalog contains data that can be used to reconstruct the original measured coordinates for the stellar images, so that we were able to perform the new reduction.

Comparison between solutions based on the FEM and Ritz's method

Number of elements	100	225	400	625	900	1600
Maximum displacement, mm	0.198	0.197	0.197	0.197	0.197	0.197
Maximum displacement difference, μm	3.06	1.85	1.39	1.16	1.04	0.909

We call a "reduction model" a representation of the relationship between the celestial coordinates of stars and the measured coordinates of their images on plates [12]. We used two reduction models: a complete third-power polynomial in the coordinates (20 plate constants) and a linear Turner model (6 constants). In the former case, we introduced no deformation corrections, whereas, in the latter case, we introduced deformation corrections in accordance with (10) and (13). The systematic errors remaining after the reduction are presented in the diagrams as fields of vectors, each of which is an average of the residual deviations in a 5 × 5-mm square.

The left panel of Fig. 2 shows the errors after reduction using the first model. This is the same model used in creating the guide star catalog for the Hubble Space Telescope [11]. The right panel of Fig. 2 shows the vector field of displacements of the plate points due to deformation after subtraction of the component that could be reproduced by the complete third-power polynomials in each of the coordinates. It is clear that the agreement of the vector fields is fairly good, although not perfect. Note that no information about the plates, apart from the telescope's and plate's geometrical sizes, was used when plotting the right panel of Fig. 2 (the diagram of displacements due to plate deformation).

Figure 3 (left panel) presents the errors after reduction using the second model on the same scale as in Fig. 2. It is evident that the systematic errors have become much smaller and their structure has became appreciably simpler, in spite of the fact that the number of plate constants was reduced from 20 to 6. This indicates that the bulk of the systematic errors are due to plate deformations. The right panel of Fig. 3 shows the same residual deviation field on a larger scale.

Harrington [10] published a photograph of the Mt. Palomar Observatory telescope's plateholder, reproduced here in Fig. 4. It shows details of the design that ensure that the plate is pressed tightly to the supporting sphere (the plate is positioned with emulsion downwards and is not seen in the photograph). Comparison of the error field in Fig. 3 (right panel) with the positions of features on the plateholder shows a clear correlation between the distribution of the error vectors and the positions of features. This provides hope that, knowing details of a plateholder design, we will be able to calculate the remainder of the systematic errors due to plate deformation on the basis of elasticity theory. Such calculations will require solution of Eq. (9) with particular boundary conditions describing the plateholder design and the method used for the plate bending.
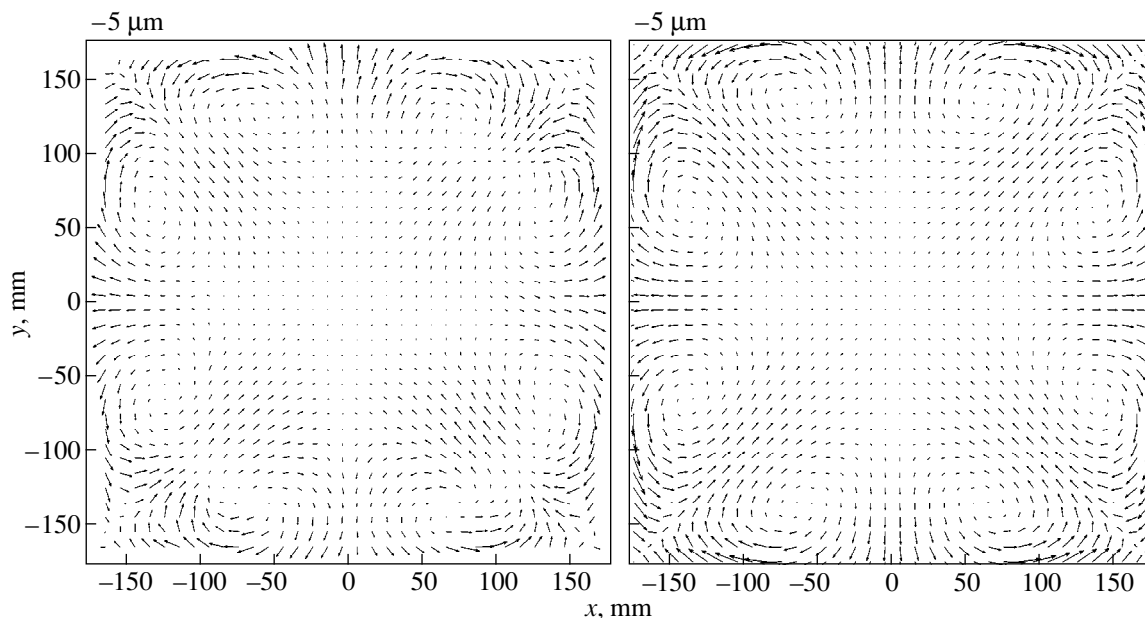

Fig. 2. Residual deviations of measurements on Palomar PAL–QV survey plates from the positions of reference stars from the TRC1 catalog: reduction with the third-order model (left panel) and a polynomial model for the plate deformations with third-order terms subtracted (right panel).
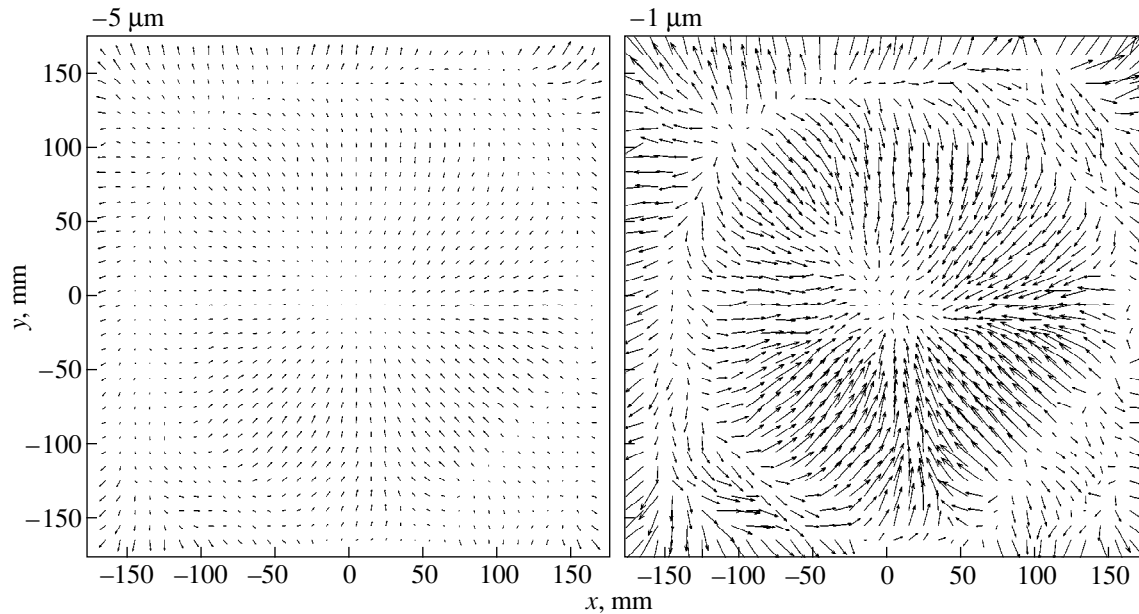
Fig. 3. Same as Fig. 2 for reductions with a linear Turner model, with preliminary account of the effects of plate bending using the polynomial model (10). The right panel shows the same on a larger scale.

We carried out a similar study for plates taken with the Schmidt telescope of the Anglo-Australian Observatory. The results are very similar to those presented above, though they do not coincide completely, probably due to differences in the plateholder design. When calculating the deformation corrections, we used the following numerical parameters: plate thickness $h = 1$ mm, Poisson ratio $\mu = 0.2$, plate length $2a = 355$ mm, radius of curvature of the plate's median surface $R = 3070$ mm.

5. CONCLUSION

We have suggested a new method for calculating plate deformations for a Schmidt telescope using a nonlinear theory for plate bending. The method can be applied in two forms: an analytical form represented by a seventh-order polynomial and a numerical form represented by the solution of a system of differential equations using a finite-element method. The former method can correct for systematic errors in measured stellar positions due to plate deformations with an accuracy of about 1 μm; the second method can be considered exact.

After applying the first method to the reduction of plates taken with the Schmidt telescope of Mt. Palomar Observatory, we arrive at the following conclusions.

(1) The bulk of systematic errors inherent in stellar positions derived from Schmidt-telescope observations are due to plate deformations.

(2) Even a simple deformation model incorporating no information about the plateholder design can reduce these systematic errors by a factor of 2 to 3 and simplify their structure, while simultaneously reducing the number of plate constants from 20 to 6. This model is much more efficient than the widespread model (1) describing cubic distortions.

(3) It is possible to eliminate residual systematic errors almost completely given details of the plateholder design, so that the system of equations (9) can be supplemented with appropriate boundary conditions.
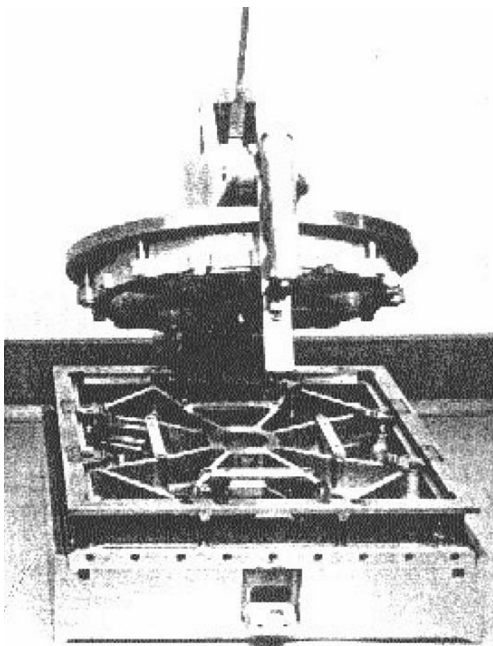

Fig. 4. Photograph of the plateholder of the Mt. Palomar Observatory Schmidt telescope, taken from [10].

Thus, we expect that further development of the proposed method for correcting for deformations will make it possible to turn Schmidt telescopes into valuable astrometric instruments, at least as good as classical astrographs but with much better limiting magnitudes. The very good image quality over a wide field of view provided by Schmidt telescopes should ultimately make it possible to obtain even better results.

REFERENCES

1. B. M. Lasker, B. J. McLean, H. Jenkner, *et al.*, in *Future Possibilities for Astrometry in Space* (RGO-ESA, Cambridge, 1995), p. 137.
2. W. M. Shepherd, Mon. Not. R. Astron. Soc. **4**, 450 (1953).
3. L. D. Landau and E. M. Lifshitz, *Theory of Elasticity* (Nauka, Moscow, 1965; Pergamon, Oxford, 1986).
4. M. K. Abele and G. É. Abele, Nauchn. Inf. Astron. Sov. **22**, 12 (1972).
5. V. L. Biderman, *Mechanics of Thin-Walled Constructions* [in Russian] (Mashinostroenie, Moscow, 1977).
6. N. A. Alfutov, *Fundamentals of Stability Calculations for Elastic Systems* [in Russian] (Mashinostroenie, Moscow, 1978).
7. L. J. Segerlind, *Applied Finite-Element Analysis* (Wiley, New York, 1976; Mir, Moscow, 1979).
8. E. Høg, A. Kuzmin, U. Bastian, *et al.*, Astron. Astrophys. **335**, 65 (1998).
9. A. Kuzmin, E. Høg, U. Bastian, *et al.*, Astron. Astrophys. **136**, 491 (1999).
10. R. G. Harringron, Publ. Astron. Soc. Pac. **64** (381), 275 (1952).
11. B. M. Lasker, C. R. Sturch, B. J. McLean, *et al.*, Astron. J. **99**, 2019 (1990).
12. A. A. Kiselev, *Theoretical Principles of Photographic Astrometry* [in Russian] (Nauka, Moscow, 1989).

Translated by N. Samus'

Investigation of Magnetic Fields in Solar Active Regions

S. I. Gopasyuk, O. S. Gopasyuk, I. P. Zalesov, D. V. Karkach, and V. V. Svistel'nikov

Crimean Astrophysical Observatory, National Academy of Sciences of Ukraine, Nauchnyĭ, Crimea, 334413 Ukraine
Received June 25, 1999

Abstract—The magnetic-field structure in solar active regions outside spots is studied. The line-of-sight fields were measured using the new Crimean digital magnetograph in three spectral lines—Fe I 5253 Å, Fe II 5234 Å, and Ti I 5193 Å. Observations in the Fe II 5234 Å line indicate systematically higher field strengths than those in the Fe I 5253 Å line. The magnetic fluxes in 2″ elements are $\sim 4.3 \times 10^{18}$ Mx, $\sim 4.6 \times 10^{18}$ Mx, and $\sim 6.2 \times 10^{18}$ Mx according to the Fe I 5253 Å, Ti I 5193 Å, and FeII 5234 Å observations, respectively. Elements 2″–8″ in size make the largest contribution to the magnetic fluxes of active regions outside spots. © *2000 MAIK "Nauka/Interperiodica"*.

1. INTRODUCTION

Observations with relatively low spatial resolution [1–5] have shown that solar magnetic fields vary very rapidly with time. Their changes are compatible with neither the transverse sizes of the observed features nor the classical value of the photospheric electrical conductivity.

Magnetograph observations of a quiet region conducted simultaneously in two spectral lines—Fe I 5233 Å and Fe I 5250 Å, whose equivalent widths differ by a factor of about 5.6 [6]—have revealed twofold-to-threefold differences in the measured field strengths [7]. These results are confirmed by more extensive observational material [8–10], making it promising to use magnetographic (the most sensitive) techniques for simultaneous magnetic-field observations in two lines to investigate fine magnetic-field structures that are not resolved in ground-based observations, even with large telescopes. Using such data, models for small-scale elements were constructed assuming that differences in the measured field strengths are purely the result of saturation of the magnetograph signal. According to these models, the field strength in small-scale elements should be ~2000 G and elements should be ~100–300 km across [9]. A review of such models is presented in [11]. Determining the differences between strengths measured simultaneously in several lines turned out to be much more difficult [12–14]. It was established that the field strength measured outside spots depends on the line equivalent width: the larger the equivalent width of a spectral line formed in the photosphere, the higher the measured field strength [12–14]. The largest field strengths are obtained from observations of lines with equivalent widths of 330–480 mÅ [14].

A high-speed digital magnetograph [15] has been operating in the Crimean Astrophysical Observatory since 1996. In particular, it is intended for observations of fine magnetic-field structures. Here, we investigate the field structure in active regions (ARs) outside spots based on 11 days of observations with a high-speed digital magnetograph.

2. OBSERVATIONS

The observational data were obtained using the high-speed digital magnetograph [15] of the Solar Tower Telescope. The basic unit for the digital magnetograph is a two-slit photometer with separate photomultipliers placed behind each slit. Information is read from each photomultiplier during 100-μs intervals separated by a half period at a frequency of 1 kHz. The brightness signals from each photomultiplier are recorded simultaneously with the field signals. The beginning of any record is preceded by the system zeros of both multipliers, as well as calibration signals. The calibration signals are written at the place on the solar surface where the record for the chosen region begins; this procedure is executed via the rotation of a calibrated plane-parallel plate. At the end of an AR recording, the dark current and noise of each multiplier are written. Our experience in using the magnetograph indicated that the system is highly stable: the system zeros drift by no more than 0.10–0.15% during a season.

The entrance slit of the spectrograph is $1'' \times 2''$. The solar image was scanned relative to the slit using a photoguide along the daily parallel, at a speed of 10″/s. The angle between the daily parallel and the direction of the spectrograph slit (the slit's height was 2″) was always no less than 75°. The distance between the centers of neighboring scans was 3.3″. An AR was sequentially observed in three spectral lines—Fe I 5253 Å, Fe II 5234 Å, and Ti I 5193 Å.

The Fe I 5253 Å line exhibits a simple magnetic splitting with Landé factor $g = 1.5$. Its equivalent width at the center of the solar disk is 75 mÅ. The excitation potential for its lower level is $E = 3.28$ eV. It is weakly

Observational data

Date	λ, Å	*t*, UT	*L*	φ
Oct. 31, 1997	Fe II 5234	8^{h}38^m	−22°	−20°
	Ti I 5193	9 50		
	Fe I 5253	12 50		
Nov. 2, 1997	Fe I 5253	8 26	4	−20
	Fe II 5234	9 26		
	Ti I 5193	10 24		
Nov. 6, 1997	Ti I 5193	8 10	9	21
	Fe II 5234	9 06		
	Fe I 5253	9 56		
Nov. 8, 1997	Fe I 5253	7 27	35	21
	Fe II 5234	8 24		
	Ti I 5193	9 07		
Nov. 9, 1997	Fe I 5253	7 30	48	21
	Fe II 5234	8 13		
	Ti I 5193	9 20		
Aug. 8, 1998	Fe II 5234	6 07	−4	−22
	Ti I 5193	7 23		
	Fe I 5253	8 41		
Aug. 9, 1998	Fe I 5253	6 49	9	−22
	Fe II 5234	7 56		
	Ti I 5193	9 06		
Aug. 13, 1998	Fe I 5253	5 47	−7	16
	Fe II 5234	6 58		
	Ti I 5193	8 24		
Aug. 16, 1998	Fe I 5253	5 48	32	16
	Fe II 5234	6 31		
	Ti I 5193	8 10		
Aug. 22, 1998	Fe I 5253	5 41	−44	31
	Fe II 5234	6 24		
	Ti I 5193	8 00		
Aug. 23, 1998	Fe I 5253	5 29	−32	31
	Fe II 5234	6 11		
	Ti I 5193	6 52		

sensitive to temperature and is somewhat enhanced in spots [6].

The splitting of the Fe II 5234 Å line is complex. The σ-component intensity-weighted mean Landé factor is $\langle g \rangle = 0.929$. Its excitation potential is $E = 3.22$ eV, and its equivalent width at the center of the sun's disk is 81 mÅ. This line becomes weaker in spots [6].

The Ti I 5193 Å line demonstrates a simple magnetic splitting with Landé factor $g = 1.083$. Its equivalent width is 80 mÅ, and excitation potential is $E = 0.02$ eV. This line is substantially stronger in spots than in the quiet photosphere [6].

During the observations in these lines, the photometer entrance slits transmitted light from 35 to 90 mÅ from the line center. The magnetic-field strength for which the centers of the σ components of the Fe I 5253 Å line were displaced toward the centers of the photometer slits was 3238 G. For the other lines, the corresponding field strength varied as $g\lambda^2$.

To recalculate the signals into field strengths, we constructed calibration curves using photoelectric records of the line profiles obtained with a double magnetograph [16]. The technique for calculating the calibration curves is briefly described in [17]. The field signals were computed for a period, corrected for brightness variations during the observation interval, and finally recalculated into field strengths.

Here, we present our measurements of the line-of-sight magnetic fields in active regions over 11 days. The positions of the AR centers (longitude *L* and latitude φ) during the observations, as well as the observing times, are presented in the table.

3. MAGNETIC-FIELD STRENGTHS IN ELEMENTS

To study the magnetic-field structures, we averaged the observational data over 50 periods. The maximum noise amplitude was ~50 G (with a standard deviation of ~18.7 G for individual measurements). Figure 1 shows maps of the line-of-sight magnetic field obtained in the three lines plotted on a 3.3″ × 3.3″ grid. These show the overall structure of the AR magnetic field and demonstrate agreement between the patterns observed in different lines. Along with sharp jumps in the field strength in the image plane, we can see numerous small elements. Maps with low spatial resolution are not sufficient to distinguish small-scale elements.

As an example, we present in Fig. 2 a scan across an AR outside spots, in which individual small-scale elements can be seen. The scans of each record were used separately to identify all elements outside spots, in which the field signals exceeded 50 G, and to determine their sizes *d* and the peak values H_m of their magnetic fields. We took the size of an isolated element at the half-maximum field strength as its size *d*. In complex structures, we took the distance between two neighboring elements to be *d*.

Figure 3 shows the dependences of the maximum strength within an element on its size *d* averaged over all observation days for each spectral line. They indicate that, according to the observations in any given line, the field strength increases with the size of the element. For 2″ elements, the mean strength was 206 G in Fe I 5253 Å, 220 G in Ti I 5193 Å, and 293 G in Fe II 5234 Å. It is striking that the observations in the Fe I 5253 Å and Ti I 5193 Å lines, which have very different thermal sensitivities but similar equivalent widths, yielded nearly equal field strengths. At the same time, the strength in the Fe II 5234 Å line is substantially
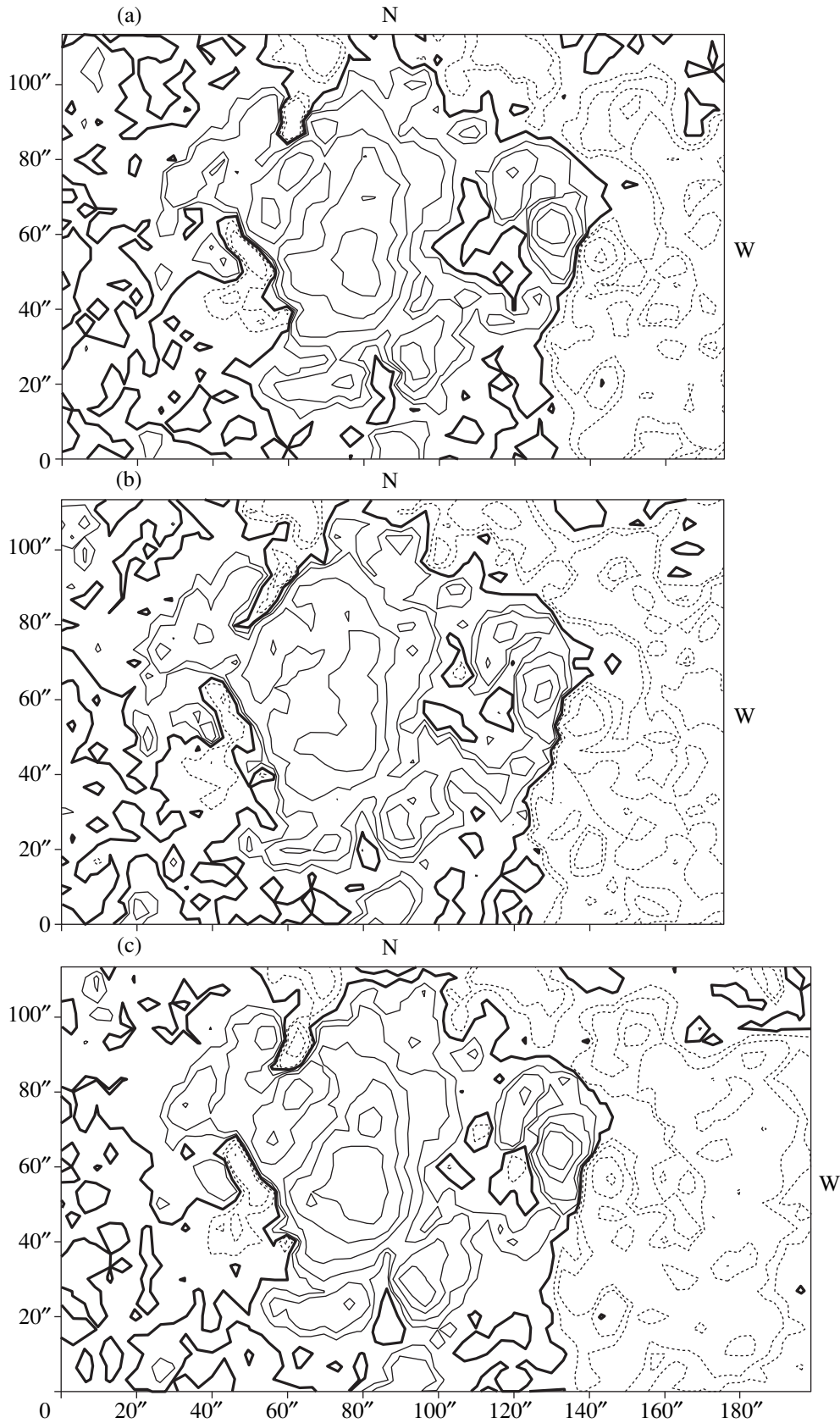
Fig. 1. Magnetic-field maps of the active region of August 23, 1998 ($L \simeq -32°$; $\varphi \simeq 31°$): (a) Fe I 5253 Å, (b) Fe II 5234 Å, (c) Ti I 5193 Å. The heavy line separates regions of opposite polarity. The thin solid lines show S polarity, and the thin dotted lines N polarity. Contour levels are 100, 200, 500, 1000, 1500, and 2000 G.
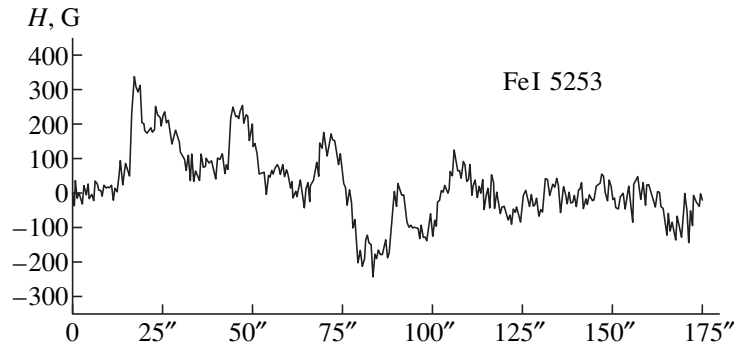
Fig. 2. Distribution of the magnetic-field strength along a scan in the active region of August 23, 1998, outside spots (Fe I 5253 Å measurements).

higher: it exceeds the intensities obtained in the two other lines by a factor of 1.33–1.52 throughout the entire range of d.

These strength differences are confirmed by extensive independent measurements [14] with a double magnetograph [16]. Figure 4 shows precisely this relationship between the intensities inferred from observations of undisturbed regions in the same spectral lines: the lowest strength was obtained from measurements in Fe I 5253 Å, almost the same strength in Ti I 5193 Å, and the highest strength in Fe II 5234 Å. However, this fact was ignored in [14]. Observations in another ionized-element line (Cr II 5237 Å), also used in [14], are consistent with this general behavior.

Thus, observations in the ionized-iron Fe II 5234 Å line show the highest field strengths in elements and the Ti I 5193 Å and Fe I 5253 Å lines show strengths a factor of 1.33–1.52 lower.

Two main factors could be responsible for weakening of the field signal from the magnetograph:

Fig. 3. Maximum magnetic-field strength in elements as a function of their size. Probable errors are indicated.

(a) Saturation, i.e., the decrease in the field signal with increase in the field strength after reaching a certain strength;

(b) Changes in the line-profile steepness when going from field-free areas, where the calibration is normally performed, to areas with magnetic fields.

In our case, the photometer slits were such that the threshold of signal saturation corresponded to ~3240 G for Fe I 5253 Å, ~4590 G for Ti I 5193 Å, and ~5270 G for Fe II 5234 Å. These values are very high, so that saturation can probably be ignored for observations in these lines.

To investigate the second effect, we photoelectrically recorded the line profiles in the central zone of the solar disk separately for left-circular and right-circular polarizations with the $1'' \times 2''$ spectrograph slit. Our analysis of these measurements showed that the line intensity changes in areas with magnetic fields. A ~ 300-G field measured in the Fe I 5253 Å line weakens this line to the point where the magnetograph field signal is reduced by a factor of 1.25; the corresponding factor for the Ti I 5193 Å line is 1.6. Applying a correction factor of 1.33–1.52 brings the observational data for Ti I 5193 Å and Fe II 5234 Å into agreement virtually throughout the entire range of sizes d. The fields measured in Fe I 5253 Å are weaker than those measured in Fe II 5234 Å, even after introducing a correction factor of 1.25.

4. MAGNETIC FLUXES

Figure 4 represents the distributions of magnetic fluxes according to element size averaged over all observation days for each of the three lines. To obtain these distributions, we calculated from each record the magnetic fluxes of individual elements and the magnetic flux of the entire active region exclusive of spots, without separating polarities. We used d as the transverse size of an element and H_m as its field strength. The magnetic fluxes in the elements were grouped according to size d and reduced to the magnetic flux of the entire AR. Essentially, the relative fluxes depend solely
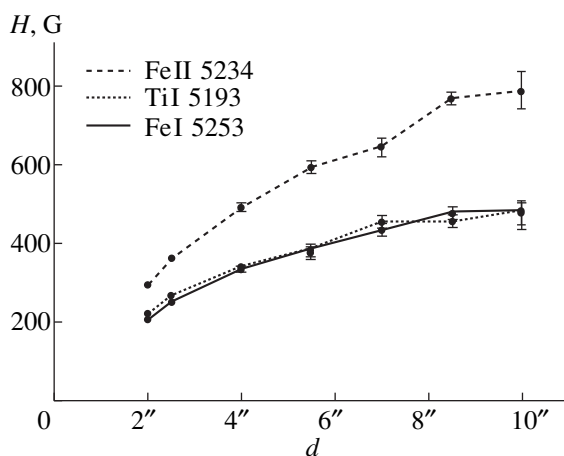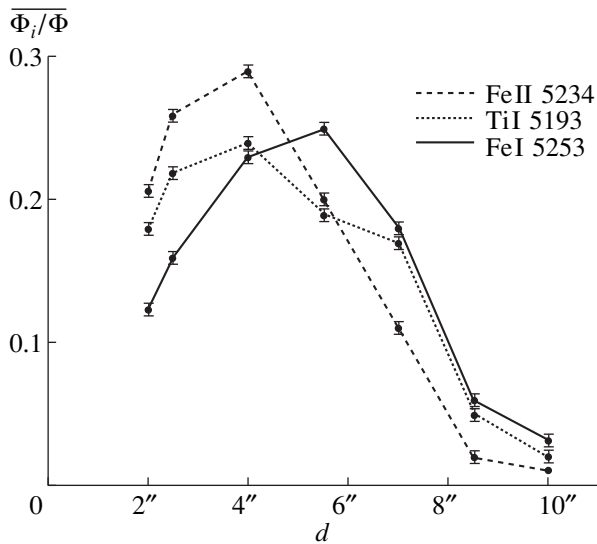
$\overline{\Phi_i/\Phi}$

Fig. 4. Relative magnetic flux $\overline{\Phi_i/\Phi}$ in elements of the active region averaged over 11 records as a function of element size. In each case, the magnetic flux of the active region outside spots is used as the flux unit. Probable errors are indicated.

on the measured field strength. The data shown in Fig. 4 are averaged over 11 records. The highest peak, obtained from the Fe II 5234 Å observations, corresponds to $d \simeq 2.5''$–$4''$. The distribution based on the Fe I 5253 Å measurements is shifted toward larger sizes with respect to the Fe II 5234 Å distribution and peaks at $d \simeq 4''$–$5.5''$. The peak of the Ti I 5193 Å distribution is at $d \simeq 2.5''$–$4''$. The relative positions of these distributions reflect differences between the field patterns observed in different lines. According to Fig. 4, structures with sizes of $2''$–$8''$ make the largest contribution to the total magnetic flux of the AR, based on the observations in all three lines. The mean magnetic fluxes in $2''$ elements indicated by our observations are 4.3×10^{18} Mx in Fe I 5253 Å, 4.6×10^{18} Mx in Ti I 5193 Å, and 6.2×10^{18} Mx in Fe II 5234 Å.

5. CONCLUSION

Our study has shown that the measured strength of the photospheric magnetic field in an AR outside spots depends on the spectral line considered. The field strength is the highest in the lines of ionized elements, which are weakened in spots (Fe II 5234 Å). The field strength based on measurements in the line Fe I 5253 Å, which is only slightly enhanced in spots, is a factor of 1.42–1.52 lower. The Ti I 5193 Å line, which is strongly enhanced in spots, probably yields an intermediate field strength.

In $2''$ magnetic elements, the field strengths are, on average, ~206 G, ~220 G, and ~293 G according to the Fe I 5253 Å, Ti I 5193 Å, and Fe II 5234 Å measurements (Fig. 3). These values are a factor of 2.4–3.4 higher than

those inferred from observations with a videomagnetograph in the photospheric network outside ARs [18]. In large-scale structural features ($d = 10''$), the field strength in Fe II 5234 Å was, on average, ~720 G, reaching 850–900 G in individual elements. Infrared observations yielded field values of 800–1700 G in ARs outside spots; at the same time, the strengths measured with a customary magnetograph did not exceed 500 G [19].

A comparison of the data in Fig. 3 to the observational data reported in [18, 19] suggests that the field strengths obtained with the Crimean digital magnetograph are more realistic. This is natural, since even averaging over 50 periods corresponds to field signals measured with an accumulation time of 0.05 s. The integration time of all other instruments, videomagnetographs among them, ranges from 1 to 100 s. For this reason, in observations with such accumulation times, the features studied are strongly blurred, even if the image quality is high; the problem is that, as our studies show, under such conditions, the contrast of a feature can change two- or threefold within several seconds.

The magnetic fluxes in $2''$ elements are ~4.3×10^{18} Mx for Fe I 5253 Å and ~6.2×10^{18} Mx for Fe II 5234 Å. The main contribution to the magnetic flux of an AR outside spots is made by elements $2''$–$8''$ in size, in spite of the fact that the field strength increases with the size of the element. This is because the number of elements declines sharply as their size increases. Note that we have isolated a large number of elements with sizes $d \simeq 1''$; this corresponds to the size of the spectrograph slit in the transverse direction, along which the Sun's image was scanned. The maximum field strengths in these elements were 2.7, or even more than 3, standard deviations. There is no doubt that elements with such sizes actually exist. However, this is a subject for a separate investigation.

The established differences between the field strengths measured in lines with different thermal sensitivities could be due to differences in the field strengths of areas of elevated and reduced brightness.

(1) If the measured field strengths correspond to the true ones, the field strengths are maximum in bright, and therefore hot, features (Fe II 5234 Å). Conversely, the strengths are lower in the darkest (coldest) areas, where the Ti I 5193 Å line preferentially forms. However, in such places, the field strength is higher than the strength averaged over an intermediate-brightness area, where the line Fe I 5253 Å forms.

(2) We cannot rule out the possibility that the magnetic fields are appreciably stronger but are concentrated in fine-structure features. In this case, to satisfy the observational conditions, we must assume that, given some field strength in fine-structure elements, the density of elements (filling factor) is maximum where hot features are situated, lower in colder areas, and minimum in areas where Fe I 5253 Å forms.

GOPASYUK *et al.*

(3) It is possible that the field strength in fine-structure elements is nonuniform, as well as the filling of magnetic structures with such elements.

The presence of small-scale elements could be directly related to their formation, as well as to the disintegration of larger-scale structures. As observations show [1, 3, 20, 21], the breakdown of large-scale structures into smaller features is characteristic of the evolution of solar magnetic fields. Magnetic structures can disintegrate into small-scale features due to the action of various magnetohydrodynamic instabilities, in particular, current instabilities—convective or overheating instability or, as suggested in [22, 23], the flute instability. However, it is far from clear to what sizes the process of magnetic-structure disintegration goes. In particular, based on indirect observations, Lozitskiĭ and Tsap [10, 24] argue that magnetic-element sizes of 10–100 km are possible. The disintegration of magnetic structures into small-scale features via magnetohydrodynamic instabilities is relatively rapid. The spreading of small-scale features over large areas may be impeded by the magnetic field of the global electric current [25], which flows in one direction in the leading part of the AR magnetic field and in the opposite direction in its trailing part. The smallest size of elements is determined by the field-diffusion process. It is reasonable to think that the lifetime of small-scale elements is determined by the field-diffusion time, i.e., by the time of electric-current damping. The damping time for the magnetic or electric field of an individual element of size d is

$$t \simeq \frac{4\pi d^2}{c^2}\sigma,$$

where σ is the electric conductivity of the plasma.

If we use the classic value of the photospheric electric conductivity $\sigma \simeq 10^{11}$ CGSE [26] and assume $d \simeq 200$ km and $t \simeq 1.6$ days, the lifetime of an element of size $d \simeq 20$ km turns out to be as short as ~ 0.4 h. In an inhomogeneous plasma, especially one such as the photospheric plasma, diverse plasma oscillations are possible in the presence of electric currents. In this case, turbulence lowers the plasma conductivity by 1 or 2 orders of magnitude [27]. As a result, the lifetime for elements ~ 200 km in size is reduced to 0.4 h and for 20-km elements, to 15 s. In connection with this, the problem of magnetic-field generation becomes very urgent.

ACKNOWLEDGMENT

REFERENCES

1. S. I. Gopasyuk, Izv. Krym. Astrofiz. Obs. **36**, 56 (1967).
2. S. I. Gopasyuk and L. G. Kartashova, Izv. Krym. Astrofiz. Obs. **63**, 25 (1981).
3. L. V. Ermakova, Issled. Geomagn. Aéron. Fiz. Solntsa, No. 62, 257 (1982).
4. G. W. Simon and P. R. Wilson, Astrophys. J. **295** (1), 241 (1985).
5. W. Unno, K. Tanaka, and M. Semel, Publ. Astron. Soc. Jpn. **33** (3), 495 (1981).
6. Ch. E. Moore, M. G. J. Minnaert, and J. Houtgast, *The Solar Spectrum 2935 Å to 8770 Å* (Washington, 1966).
7. J. W. Harvey and W. Livingston, Sol. Phys. **10** (2), 283 (1969).
8. S. I. Gopasyuk, V. A. Kotov, A. B. Severny, and T. T. Tsap, Sol. Phys. **31** (2), 307 (1973).
9. J. O. Stenflo, Sol. Phys. **32** (1), 41 (1973).
10. V. G. Lozitskiĭ, Phys. Solariterr., No. 14, 88 (1980).
11. S. K. Solanki, in *Proceedings of 10th European Regional Astronomy Meeting of the IAU, 1987*, Ed. by L. Hejna and M. Sobotka, Vol. 1, p. 95.
12. S. I. Gopasyuk and A. B. Severnyĭ, Pis'ma Astron. Zh. **9** (2), 120 (1983) [Sov. Astron. Lett. **9**, 65 (1983)].
13. M. Semel, Astron. Astrophys. **97** (1), 75 (1981).
14. S. I. Gopasyuk, Izv. Krym. Astrofiz. Obs. **72**, 159 (1985).
15. S. I. Gopasyuk and I. P. Zalesov, Kinematika Fiz. Nebesnykh Tel **12** (5), 48 (1996).
16. V. A. Kotov, A. B. Severnyĭ, and T. T. Tsap, Izv. Krym. Astrofiz. Obs. **65**, 3 (1982).
17. S. I. Gandzha, S. I. Gopasyuk, and T. N. Tarasova, Kinematika Fiz. Nebesnykh Tel **10** (4), 36 (1994).
18. J. Wang, H. Wang, F. Tang, *et al.*, Sol. Phys. **160** (2), 277 (1995).
19. D. Rabin, Astrophys. J. Lett. **390** (2), L103 (1992).
20. J. O. Stenflo, in *Basic Mechanisms of Solar Activity*, Ed. by V. Bumba and I. Kleczek (Reidel, Dordrecht, 1976; Mir, Moscow, 1979).
21. M. H. Gokhale and C. Zwaan, Sol. Phys. **26** (1), 52 (1972).
22. J. H. Piddington, Astrophys. Space Sci. **34** (2), 347 (1975).
23. J. H. Piddington, Astrophys. Space Sci. **35** (2), 269 (1975).
24. V. G. Lozitskiĭ and T. T. Tsap, Kinematika Fiz. Nebesnykh Tel. **5** (1), 50 (1989).
25. S. I. Gopasyuk, Itogi Nauki Tekh., Ser. Astron. **34**, 6 (1987).
26. M. T. Kopecký, Bull. Astron. Inst. Czech. **22** (6), 343 (1971).
27. B. B. Kadomtsev, *Collective Phenomena in Plasma* [in Russian] (Nauka, Moscow, 1976).

Translated by A. Getling

Longitude and Latitude Structure of the Polar Activity of the Sun in the 21st Cycle

V. P. Mikhaĭlutsa and V. V. Makarova

Mountain Astronomical Station, Pulkovo Observatory, Russian Academy of Sciences,
P.O. Box 145, Kislovodsk, 357700 Russia

Received July 20, 1999

Abstract—A catalog of observations of polar faculae by the Mountain Astronomical Station of the Pulkovo Observatory (Kislovodsk) for the 21st polar-activity cycle of the Sun (1972–1976) has been compiled. The mean annual and semiannual longitude distributions of the facular surface density have been constructed for latitude bands from 35 to 85° with steps of 10° in latitude and 30° in longitude in polar (the "wind roses") and cylindrical projections, using a Bartels coordinate-grid rotation system. Coherent spatial structures in these distributions, which are characteristically elongated in two mutually perpendicular directions (i.e., they have an "X"-like appearance), can be identified. The high-latitude activity in the northern and southern hemispheres tends to be in spatial antiphase. This behavior corresponds to a four-sector global polar-activity structure. This indicates the presence of a magnetic-field source that is not associated with the differential rotation of the sun and modulates the evolution of local magnetic fields. © 2000 MAIK "Nauka/Interperiodica".

1. INTRODUCTION

Bright compact objects in polar regions of the sun observed in white light and, with especially high contrast, in the ultraviolet, are called "polar faculae" [1]. The largest number of polar faculae are observed in periods of minimum sunspot activity, and the cycle of their appearance is in temporal antiphase with the sunspot cycle. Polar faculae can be separated into three types: (1) single pointlike objects (with angular sizes 1–2″), (2) groups of pointlike objects (with the total size of each group up to 10″), and (3) extended diffuse objects (with angular sizes up to 20″). Polar faculae in the form of diffuse objects occur less frequently than the other two types.

A fragment of a photoheliogram obtained by the Mountain Astronomical Station of the Pulkovo Observatory in Kislovodsk is presented in Fig. 1, which shows a solar polar region with polar faculae. The visibility of polar faculae depends on both objective factors (for example, image jitter, the type of photographic plate used, and the quality of the photographic development) and subjective factors (i.e., related to the partic-

ular observer). Therefore, the most reliable results on polar faculae have been obtained using statistical methods. Polar faculae seem to be associated with magnetic fields. It was shown in [2] that the number of polar faculae and the flux of the solar magnetic field in polar regions are well correlated. However, the basic mechanism for their generation remains unclear. The proper rotation of polar faculae is probably differential [3]. The relatively short lifetimes of these objects (from 10–15 min to one day, according to various estimates) hinder studies of their rotation [4]. The concentration of polar faculae in latitude and time shifts toward higher latitudes during the development of their cycle [5].

The characteristic features in the distributions in latitude and longitude depend primarily on the choice of rotation period for the coordinate grid. For example, it was found for the first time using a grid rotation period of $T = 27.23$ synodic days that there are certain regularities in the longitude distribution of the number of polar faculae [6]: there are two main maxima in the distributions, the maxima are usually localized at opposite sides of a diameter, and the positions of extrema in the polar-faculae distributions in different solar hemi-
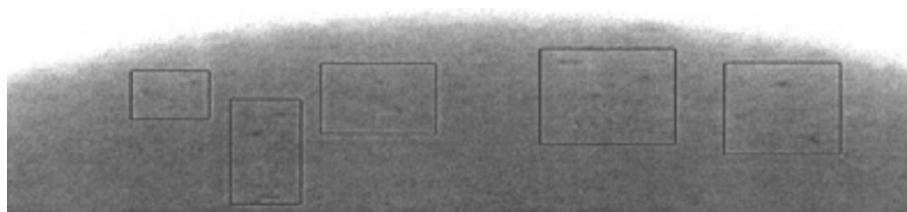

Fig. 1. Faculae in the polar region of the solar surface. The photoheliogram was obtained by the Mountain Astronomical Station of the Pulkovo Observatory in Kislovodsk.
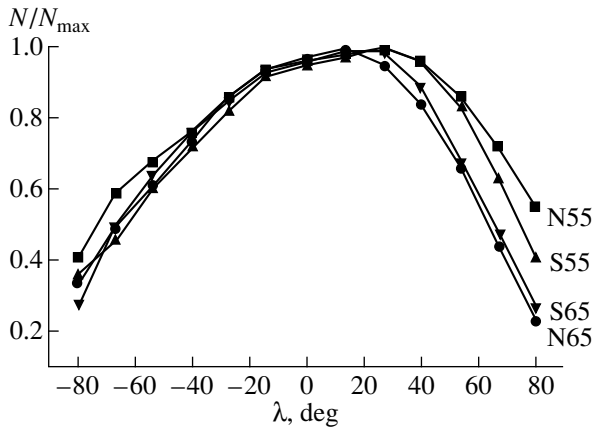
Fig. 2. Number of polar faculae over a $1° \times 30°$ region. Longitude is measured from the central meridian.

spheres are in spatial antiphase with respect to each other. These regularities were obtained from statistical analyses as a result of multiple averaging of the corresponding distributions. As shown in subsequent investigations, these features could reflect the presence of some source inside the Sun (a wave of nonradial pulsations) that rotates with the Bartels period $(27^{\mathrm{d}}.0)$ and modulates the surface density of polar faculae [7, 8].

Thus, studies of the longitude distributions of polar faculae led to the discovery of a new phenomenon—sectoral–hemispheric asymmetry in the concentration of polar faculae and similar objects over the entire solar surface. The aim of the present paper is to study finer features of the sectoral–hemispheric asymmetry over considerably shorter averaging time scales using new data and new analysis methods.

The observational material was obtained at the Mountain Astronomical Station of the Pulkovo Observatory in 1972–1976 (photoheliograms of the "Solar Service"). One of us (V.V.M) has recently completed the compilation of a first catalog of detailed observations of polar faculae for this time interval. This catalog contains the coordinates of the polar faculae in the Carrington system, the types of faculae, and their number at each point. Using computer processing, the catalog data were transformed into a surface-density distribution of polar faculae over regions covering $10°$ in latitude and $30°$ in longitude in a Bartels rotation system. This transformation inevitably requires taking into account the visibility function of the faculae.

2. THE VISIBILITY FUNCTION OF POLAR FACULAE

The number of polar faculae in a region with a specified size has a statistical dependence on the position of this region with respect to the central meridian, its latitude at the solar surface, and the heliographic latitude of the earth. The last two factors are important, first and

foremost for studying the latitude distributions of the faculae. They affect the number of polar faculae in a specified latitude band in studies of the longitude distributions in the same way. Therefore, we paid the most attention to the visibility function of polar faculae for various positions of a region with respect to the central meridian. By considering many passages of various regions covering 10 heliographical degrees in latitude and 30 degrees in longitude, we constructed dependences for the number of polar faculae (normalized to their maximum values) as functions of the heliographic longitude of the corresponding regions. We studied the latitude ranges $50°–60°$ and $60°–70°$ in both solar hemispheres.

Figure 2 presents the resulting visibility functions. These all correspond well to each other, and their eastern branches nearly coincide. The western branches are split, and regions centered on $55°$ have larger visibility functions in both hemispheres compared those centered on $65°$. In addition, there is some asymmetry of the branches relative to the central meridian: the maximum values of these functions are shifted toward the west by 10–20 heliographic degrees. Such east–west asymmetry is also present in the visibility function of sunspots [9] and is usually attributed to their magnetic nature. The observational points in Fig. 2 can be smoothly fitted by a parabolic function. These smoothed values are shown in the table in boldface; extrapolated values for higher and lower latitudes are printed in normal font. We used these tabular values of the visibility function to transform the data from the catalog of polar faculae to distributions of their surface density.

3. THE POLAR-FACULAE DENSITY DISTRIBUTIONS IN POLAR COORDINATES

We averaged the polar-faculae density distributions over annual (from 1972 to 1974) and semiannual (from 1975 to 1976) intervals. Figure 3 shows several examples of the longitude density distributions of the polar faculae in the "wind rose" polar projection, which clearly demonstrate the presence of X-like features. Although the latitudes with maximum polar-faculae densities usually varied in an unpredictable fashion, some general tendencies can be discerned. In all the distributions, we can identify four longitude directions in which regions of enhanced density are concentrated. These directions form the regular X-shaped features shaded in Fig. 3. The orientation of the X's at the solar surface did not change with time and was the same in both hemispheres. Note that most of the X-shaped features were not as clearly delineated as those in Fig. 3. The maximum polar-faculae densities usually did not exactly correspond to the directions of the axes of the X's, and not all axes were clearly distinguished in specific distributions. However, it is clear that there is a general overall agreement between parts of the X-shaped features over the time interval studied.
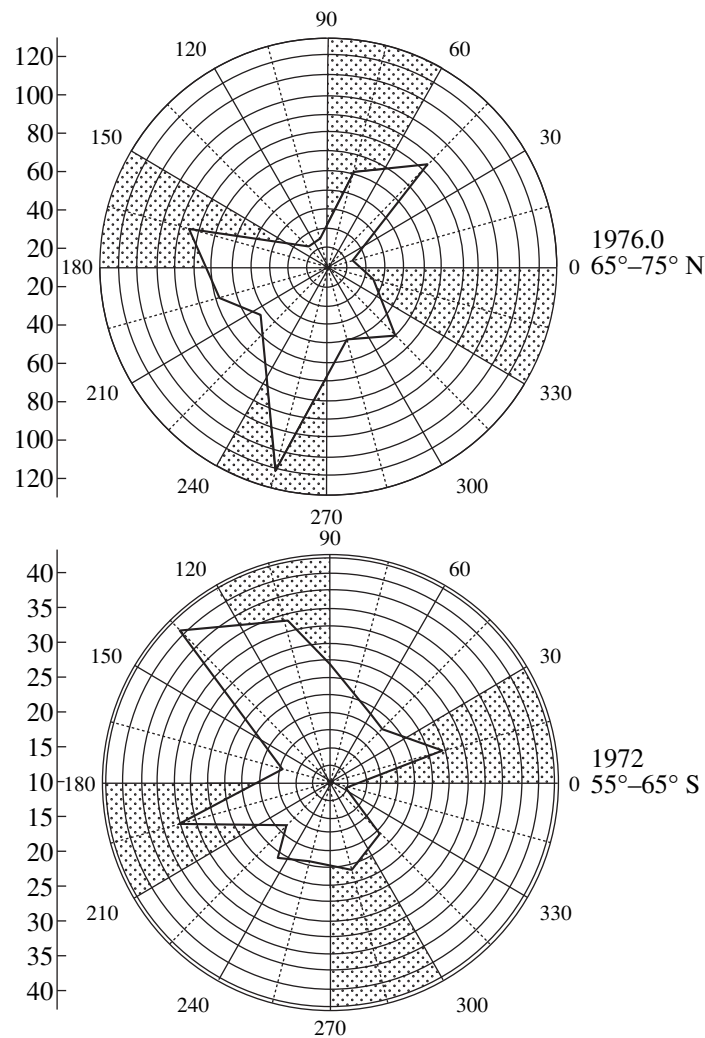
Fig. 3. Examples of X-shaped distributions of the polar-faculae density in a polar projection for latitudes 65°–75° in the northern hemisphere in the first half of 1976 (top panel) and for latitudes 55°–65° in the southern hemisphere in 1972 (bottom panel). The scale for the surface density is given on the left-hand side.

One "X" with a time-independent orientation cannot describe all longitudes with maximum polar-faculae densities. This orientation sometimes changed with time or latitude within ±30° of its average position. This is true for the distributions in both solar hemispheres. There was no agreement between the directions of X's in different hemispheres, and they showed a tendency to be spatially in antiphase.

To find the latitude bands where the orientations of the X-shaped features were most stable, we normalized all the distributions to their maximum value and then summed them separately in each latitude band over the entire polar-activity cycle. The result is presented in Fig. 4, which shows that the distributions for the lowest (35°–45°) and highest (75°–85°) latitudes in both solar hemispheres have the most stable orientations. The distributions for different hemispheres in these latitude bands are in spatial antiphase. The orientations of the distributions for other latitudes are less stable in time. As a result, the shapes of these distributions are slightly spread in longitude. If the distributions in Fig. 4 are analyzed as a sequence, we note a rotation of their peaks in the direction of increasing longitude in the transition from low to high latitudes. As a result, the distributions for low latitudes (35°–45°) in each hemisphere are in spatial antiphase with respect to the corresponding distributions for high latitudes (75°–85°).

Thus, we can draw the following conclusions.

(1) The distributions of the extrema of the polar-faculae density in polar coordinates in a Bartels rotation system tend to be oriented along mutually perpendicular directions (i.e., they form X-shaped features).

(2) These directions are most stable at the lowest and highest polar-faculae latitudes, where the distribu-

Visibility function of polar faculae $N/N_{\max}$

λ, deg	40°–50°	50°–60°	60°–70°	70°–80°	40°–50°	50°–60°	60°–70°	70°–80°
	Northern hemisphere				Southern hemisphere			
−90	0.50	**0.27**	**0.08**	0.04	0.20	**0.10**	**0.06**	0.04
−80	0.58	**0.39**	**0.26**	0.17	0.31	**0.28**	**0.25**	0.17
−70	0.64	**0.52**	**0.42**	0.34	0.49	**0.45**	**0.41**	0.34
−60	0.68	**0.63**	**0.58**	0.53	0.58	**0.56**	**0.56**	0.53
−50	0.74	**0.72**	**0.70**	0.68	0.70	**0.68**	**0.68**	0.65
−40	0.82	**0.81**	**0.80**	0.79	0.79	**0.77**	**0.79**	0.75
−30	0.88	**0.88**	**0.88**	0.88	0.88	**0.86**	**0.87**	0.85
−20	0.92	**0.92**	**0.93**	0.92	0.92	**0.91**	**0.93**	0.92
−10	0.96	**0.96**	**0.96**	0.96	0.97	**0.95**	**0.97**	0.96
0	0.98	**0.98**	**0.98**	0.98	0.98	**0.97**	**0.98**	0.98
+10	0.98	**0.98**	**0.96**	0.96	0.99	**0.98**	**0.97**	0.96
+20	0.98	**0.98**	**0.93**	0.90	0.97	**0.96**	**0.94**	0.92
+30	0.96	**0.95**	**0.87**	0.80	0.95	**0.93**	**0.90**	0.86
+40	0.93	**0.91**	**0.79**	0.70	0.91	**0.87**	**0.83**	0.75
+50	0.88	**0.86**	**0.69**	0.60	0.86	**0.80**	**0.73**	0.63
+60	0.81	**0.78**	**0.55**	0.40	0.76	**0.72**	**0.60**	0.45
+70	0.72	**0.69**	**0.43**	0.30	0.64	**0.61**	**0.46**	0.31
+80	0.63	**0.60**	**0.24**	0.17	0.55	**0.48**	**0.28**	0.19
+90	0.50	**0.47**	**0.07**	0.04	0.40	**0.34**	**0.13**	0.08

tions have opposite spatial phases both in different hemispheres in the same latitude bands and in low and high latitudes within a single hemisphere.

4. DISTRIBUTIONS OF THE DENSITY OF POLAR FACULAE IN CYLINDRICAL COORDINATES

Another representation of the same data reveals other characteristic features of polar activity not identified previously. In particular, the latitude–longitude distributions of the polar-faculae density in a cylindrical coordinate system show stable regions of concentration of the polar faculae. Figure 5 shows contours of equal polar-faculae density for the northern (left) and southern (right) hemispheres. If the rotation of the extrema of the polar-faculae density is differential, then (1) the yearly averages of these distributions should be spread out in longitude due to the Bartels rotation of the coordinate system, and (2) the structures in these distributions in different years should not be similar. However, Figure 5 shows no longitudinal smearing of the structures. On the contrary, the limited regions with increased densities of polar faculae (whose sizes range from 10°–30° to 20°–60°) form stable structures existing for many years (especially in the northern hemisphere).

Therefore, if the proper rotation of the polar faculae is differential, the presence of stable regions of polar-

faculae density rotating at the Bartels rate indicate that their source must be located beyond the zone of differential rotation of the Sun.

5. DISCUSSION

All the characteristic properties of the distributions of polar-faculae density revealed in our study are relatively subtle features. They can be discerned only if several conditions are satisfied. First, the data must be averaged over a sufficiently long time interval. (This requirement results from the small amplitude of the signal that must be distinguished from the noise.) The next factor is the choice of the rotation period for the longitudinal coordinates. Finally, we must present the results in an appropriate way. In particular, only by using polar coordinates was it possible to identify the X-shaped features of the longitude distributions of the polar-faculae density.

Our results are insufficient for us to draw unambiguous conclusions. A similar analysis should be conducted for the 22nd and 23rd cycles of polar activity, which will be a subject of our future research. However, we can draw several conclusions based on the current results.

(1) The loss in stability of the X-like orientation at latitudes ±(55°–75°)° could have two origins: either the rotation of these structures varies with time and differs
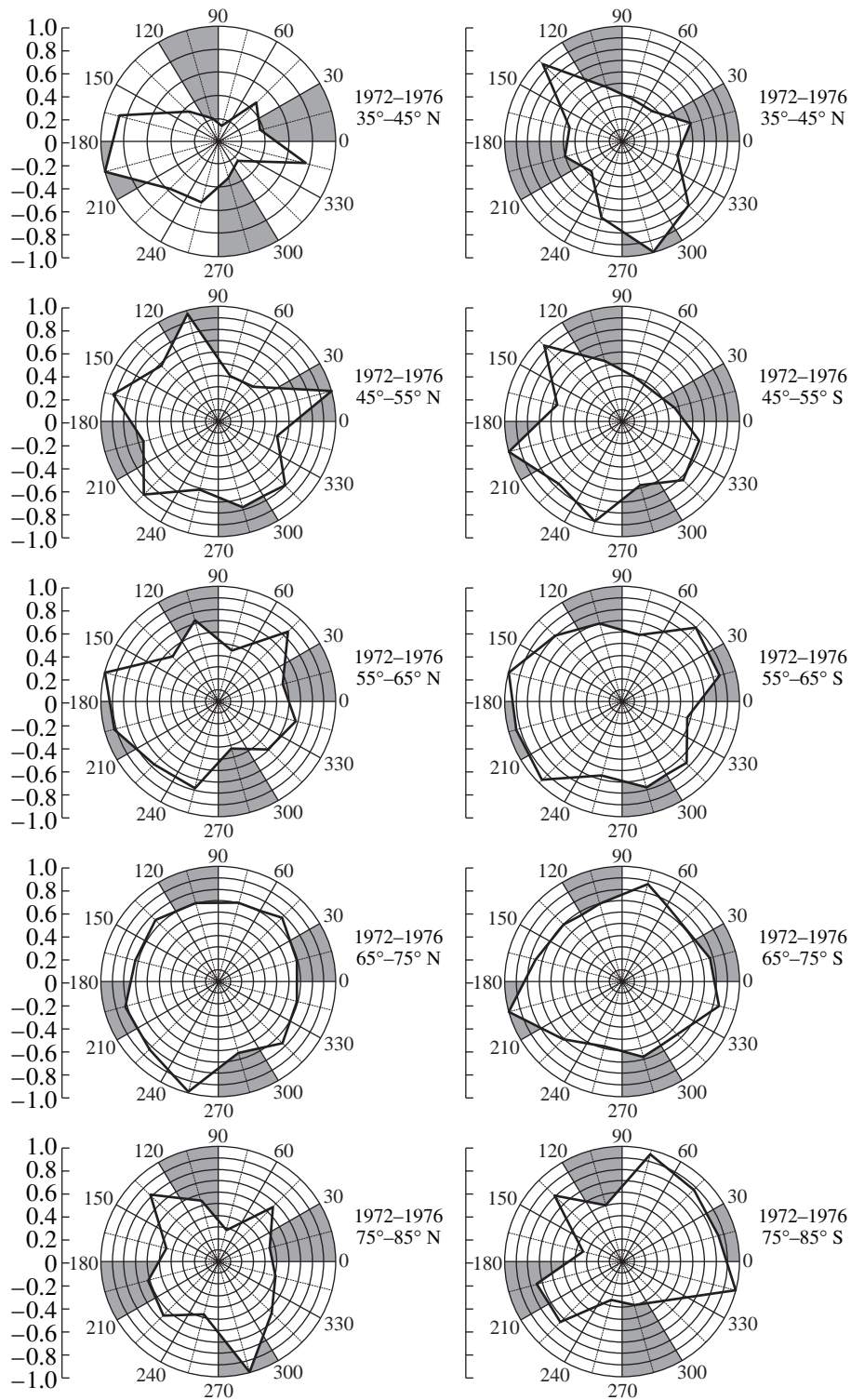
Fig. 4. Normalized longitude distributions of the polar-faculae density in various latitude bands averaged over the entire period 1972–1976.

slightly from a Bartels law or the distribution of polar faculae in this band is nonuniform and unstable, hindering identification of a weak stationary signal in the density distributions.

(2) According to helioseismological data, the Bartels period (27.0 synodic days) is not detected at high heliolatitudes and in layers below the bottom of the convection zone. The rotation of the medium in these
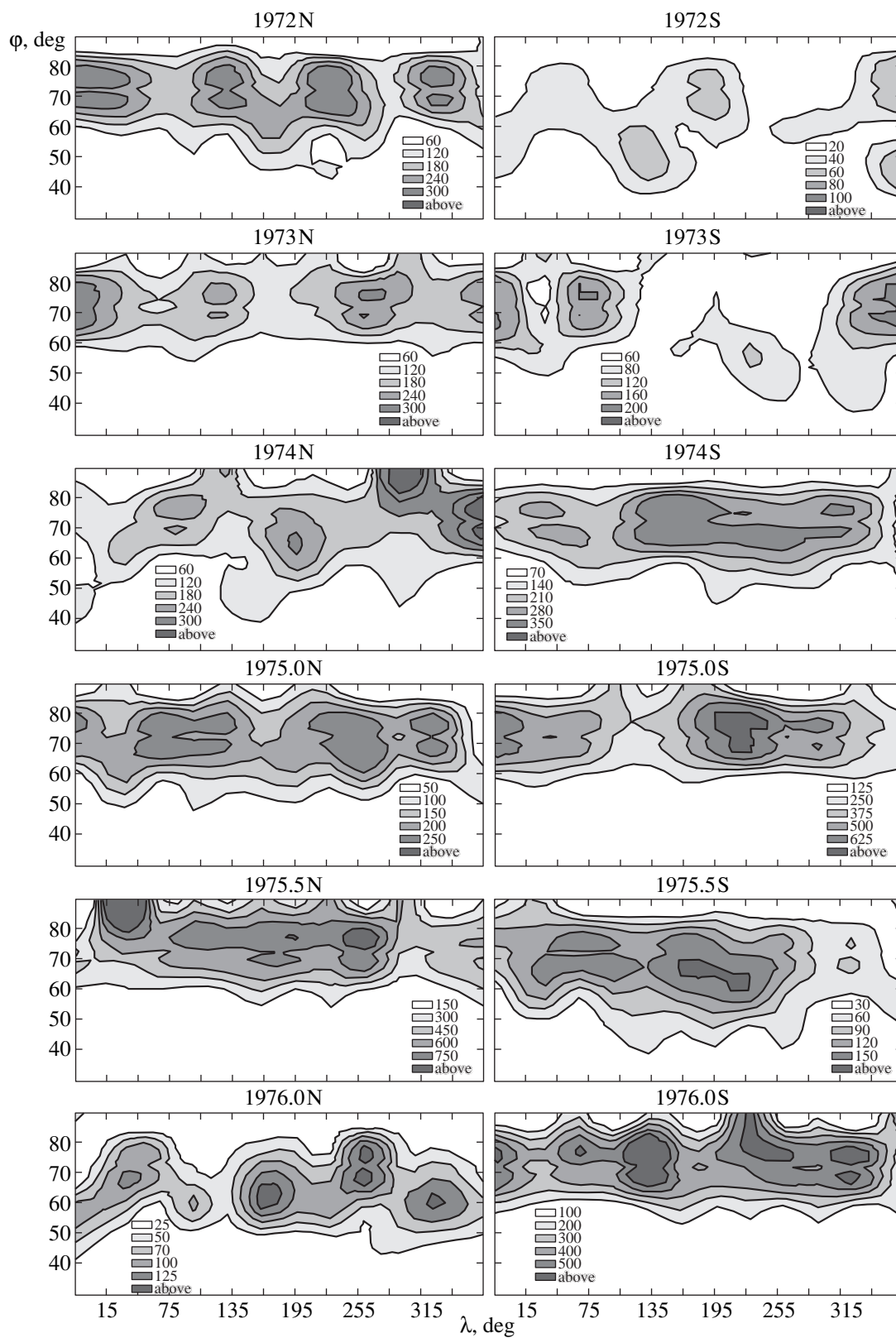
φ, deg

Fig. 5. Contours of polar-faculae density in cylindrical coordinates.

regions is slower (T = 28–29 synodic days) [10]. This seems to contradict our results. This discrepancy can be explained as follows. The rotation of the medium is measured in helioseismology via the Doppler effect and represents the group velocity for propagation of pressure perturbations in the medium. On the other hand, the Bartels rotation period could correspond to the phase velocity of another global wave process, so that it is not detected by Doppler observations. Such a global wave process should have sector number $m = 2$ (i.e., it should be quadrupolar).

Thus, along with the usual source of small-scale solar activity (localized near the bottom of the convection zone), there is some evidence suggesting the existence of another source that modulates the activity of the first source in the sector (quadrupole-like) segments of the solar surface and is located beyond the zone of differential rotation.

REFERENCES

1. F. Weber, Wochenschr. Astron. Met. Geogr. **11**, 161 (1868).

2. V. I. Makarov and V. V. Makarova, in *Current Problems in Solar Activity* [in Russian] (Peterburg. Inst. Yad. Fiz., St. Petersburg, 1997), p. 149.

3. V. A. Solonsky and V. V. Makarova, Sol. Phys. **131**, 372 (1992).

4. V. I. Makarov and V. V. Makarova, Soln. Dannye, No. 12, 88 (1984).

5. V. I. Makarov and V. V. Makarova, Soln. Dannye, No. 9, 99 (1985).

6. V. P. Mikhailutsa and V. V. Makarova, Sol. Phys. **155**, 391 (1994).

7. V. P. Mikhaĭlutsa and V. V. Makarova, in *Current Problems in Solar Activity* [in Russian] (Peterburg. Inst. Yad. Fiz., St. Petersburg, 1997), p. 372.

8. V. P. Mikhailutsa and V. V. Makarova, Astron. Astrophys. Trans. **17** (5), 393 (1999).

9. M. Kopecky, Bull. Astron. Inst. Czech. **36**, 359 (1985).

10. A. G. Kosovichev *et al.*, Sol. Phys. **170**, 43 (1997).

Translated by Yu. Dumin